Nuno Filipe Viseu Duarte

HIGH SPEED DATA ACQUISITION IN SWEPT SOURCE OPTICAL COHERENCE TOMOGRAPHY

Master's degree in Physics Engineering

September 2016

· U C ·

UNIVERSIDADE DE COIMBRA

High Speed Data Acquisition in Swept Source Optical Coherence Tomography

Master Dissertation submitted for the Master's degree in Physics Engineering with specialization in Instrumentation of the Faculty of Sciences and Technology of the University of Coimbra. Supervised by PhD. Professor José Paulo Pires Domingues.

Nuno Viseu Duarte

September 2016

Acknowledgments

Many people deserve acknowledge for having directly or indirectly contributed to the realization of this work.

Firstly, my parents, sister, grandparents and the remaining part of my family to whom I thank for guiding me throughout my academic path.

To Afonso and Zélia, for opening the door of their house and family, where I dedicated many hours of work with pleasant company.

To professors José Paulo, Miguel Morgado and Rui Bernardes who led me, broaden my knowledge in many topics and kept me motivated throughout this project.

To professor Joaquim Santos for his contribution in the text revision and receptivity for assisting me in every matter.

To my friends, whose presence lightened the mental stress claimed by this project.

To Sara, for making my life complete.

Abstract

Optical Coherence Tomography (OCT) is an imaging technique especially popular in the medical field, developed to obtain information about the morphology of living biological tissue through cross-sectional images with micrometer resolution. One of the most common applications is the visualization of the eye.

In the last decade considerable breakthroughs in this technique have happened, mostly due to the improvement of resolution, sensitivity, dynamic range and acquisition speed. An OCT system is being developed from scratch at IBILI to be used for small animal imaging, namely of the eye. Animals with anatomical resemblance to humans are often used in biomedical research to test new techniques and therapies. Therefore, applying this particular imaging technique in such animals can provide a major contribution to retinal physiology research and consequently an important contribution to medicine, from which all humans can benefit.

The development of this project involves didactic aspects in several instrumentation areas, for instance data acquisition and signal processing. It also bears a strong component of physics and engineering fields such as wave optics and optoelectronics.

This work will focus on the improvement of the data acquisition system of this OCT, mostly by means of software developing. Emphases will be given to the acquisition speed, one of the crucial parameters of an OCT, but many other aspects were improved such as the image quality and the simplification of the user's interaction with the software interface.

Resumo

A Tomografia de Coerência Óptica (OCT) é uma técnica de imagiologia especialmente popular na área da medicina, desenvolvida para obter informação sobre a morfologia de tecidos biológicos vivos através de imagens transversais com resolução micrométrica. Uma das aplicações mais populares é a visualização do olho.

Na última década ocorreram consideráveis avanços nesta técnica, principalmente devido à melhoria da resolução, sensibilidade, gama dinâmica e velocidade de aquisição. Um sistema OCT está a ser desenvolvido de raíz no IBILI para ser utilizado em imagiologia de animais de pequeno porte, nomeadamente do olho. O uso de animais com semelhanças anatómicas ao ser humano é frequentemente em investigação biomédica para testar novas técnicas e terapias. Assim, aplicar esta técnica de imagiologia nestes animas pode constituir uma importante contribuição para a medicina, da qual todos os humanos podem tirar benefício.

O desenvolvimento deste projecto envolve aspectos didáticos em várias áreas de instrumentação, tais como aquisição de dados e processamento de sinais. Também acarreta uma componente forte das áreas de física e engenharia como óptica de ondas e optoelectrónica.

Este trabalho vai visar a melhoria do sistema de aquisição de dados deste OCT, principalmente através do desenvolvimento de software. Será dado ênfase à velocidade de aquisição, um dos parâmetros cruciais de um OCT, mas muitos outros aspectos foram alvo de melhoria, tais como a qualidade de imagem e a simplificação da interação entre utilizador e software.

Contents

List of Figures

List of Tables

List Of Abbreviations

- ADC - Analog-to-Digital Converter

- CCD - Charge-Coupled Device

- CMOS - Complementary Metal-Oxide-Semiconductor

- CMRR - Common Mode Rejection Ratio

- DAC - Digital to Analog Converter

- DAQ - Data Acquisition

- DDR - Double Data Rate

- DFT - Discrete Fourier Transform

- DRAM - Dynamic Random Access Memory

- FD-OCT - Fourier Domain OCT

- FFP-TF - Fiber Fabry-Perot Tunable Filter

- FFT - Fast Fourier Transform

- FPGA - Field Programmable Gate Array

- GPU - Graphics Processing Units

- IDFT - Inverse Discrete Fourier Transform

- IFFT - Inverse Fast Fourier Transform

- I/O - Input/Output

- LED - Light-Emitting Diode

- LSB - Least Significant Bit

- MSB - Most Significant Bit

- MSPS - Mega Samples Per Second

- NIR - Near-Infrared

- OCT - Optical Coherence Tomography

- OLCR - Optical Low-Coherence Reflectometry

- PCI - Peripheral Component Interconnect

- PDA - Photodiode Array

- PLL - Phase-Locked Loop

- QDR - Quad Data Rate

- RGB - Red, Green and Blue (color model)

- SNR - Signal-to-Noise Ratio

- SOA - Semiconductor Optical Amplifier

- SRAM - Static Random Access Memory

- SD-OCT - Spectral Domain OCT

- SS-OCT - Swept Source OCT

- TD-OCT - Time Domain OCT

- TTL - Transistor-Transistor Logic

Introduction

Optical coherence tomography (OCT) is an optical imaging technique capable of producing a high resolution cross-sectional image of the internal structures of a sample by measuring the behavior of light after being backreflected by them. We can make an analogy between this technique and ultrasound imaging, except that OCT measures backreflections of light instead of sound.

Certain characteristics such as being noninvasive and using nonionizing radiation makes this technique very attractive in medical applications and research, particularly in ophthalmology. The rise of a frequency domain approach on OCT exponentially increased the acquisition speed and made *in vivo* imaging possible with very satisfying results, which contributed to the popularity of this imaging technique over the last decade.

This led the Institute for Biomedical Imaging and Life Sciences (IBILI) to develop an OCT system from scratch, assembling the required optical components and developing an acquisition system along with an application software for the user to interact with to control the system and visualize the acquired data. This OCT will be used for retinal imaging in small animals, namely mice and rats.

This project began about 4 years ago, and one of the most critical aspect lacking before this work was the fact that the acquisition speed was still very far from the required to perform real time imaging. There was also no means of saving a complete volume acquisition for posterior analyses, since the system only operated in live mode, i.e. acquired data was displayed as an image and irreversibly lost whenever the new data necessary to produce a new image was acquired. These were only some of the many issues that needed to be solved.

The ultimate goal of my contribution in this project is to make the acquisition system of the OCT capable of performing real time *in vivo* imaging. The optical apparatus of the OCT must be correctly adjusted and optimized to obtain acceptable results, however this task was left for a distinct work. Hence, this work will mostly aim attention at the data acquisition hardware and software, which will be explained in detail. The modifications on the software version previous to this work will be individualized, to clearly distinguish the features that were added or improved from the already existing and satisfactorily working ones.

For a clear exposition of the developed OCT, this work is organized in distinct chapters, each one related to a specific subject. Initially, an overview of the basic physical and engineering principles that support the OCT technique is presented, along with some technical nomenclature necessary to understand the follwing chapters and a general state of the art that will report the evolution and the current state of OCT.

After this, the OCT system being developed at IBILI will be specified in terms of its components and their most relevant characteristics will be presented. The methods used to synchronize different components that must work in harmony will

also be addressed. The path of the optical and electrical signals that steer the acquisition will also be traced on their travel along different optical and acquisition hardware components.

Subsequently, the work developed on the acquisition software will be detailed, explaining how data is handled from the moment it is acquired to the moment it is displayed to the user, while specifying the distinctions on the previous software version. This chapter will also clarify how the user should interact with the software to accomplish the desired objectives.

Finally, some obtained results will be presented and discussed on a qualitative and quantitative analysis.

1 | *OCT Overview and Basic Principles*

In order of the fully understand the core of this thesis, i.e. how data is acquired in OCT, it is crucial to perceive the signals' origins. That involves getting familiarized with the physics behind and OCT system, in order to know exactly what and how signals are being generated. Therefore, this initial chapter will be dedicated to the explanation of the most important concepts related to the operation of an OCT system.

Initially, a brief historical context of the origins of this technique will be exposed, to present a notion of its arising.

The basic setup and a brief description of its components will also be addressed, as well as different possible approaches regarding data acquisition. As we will see, different approaches implicate the use of different setups.

It will also be made reference to some of the most relevant optical parameters that allow a quantitative evaluation of the performance of an OCT system, as well as common imaging artifacts that corrupt the desired information. It is important to understand the origins of these artifacts to know how to overcome, attenuate or deal with them.

To end this chapter, it will be explained how data acquisition relates to the scanning of the samples, which allows different types of acquisition and the visualization of different dimensions of the sample.

1.1   Historical Context and the Arising of OCT

OCT is presently one of the most popular imaging technique, especially in ophthalmology. However, it was only in recent years that OCT established itself as a recurring clinical practice in this area. In fact, a lot of evolutionary steps were involved in the creation of this technology, and more steps are certainly yet to be taken.

The first measurements of the length of the eyeball *in vivo* was performed by R. H. Rushton in 1938[1]. In his experiment, a narrow beam of X-rays entered the eye perpendicularly to its optical axis and intersected the retina in a circle (AB in Figure 1.1). As a result of this stimulus, a visible ring emerged in the retina. By moving the X-rays source to the right, the ring shrinks, becoming a bright spot when the X-rays reach the posterior pole (P). The position of the corneal vertex (C) is located optically by an apparatus carried in the same slide that moves the X-ray source. The antero-posterior diameter ($\overline{CP}$) is then obtained by simply measuring the distance between the referred apparatus and the source.
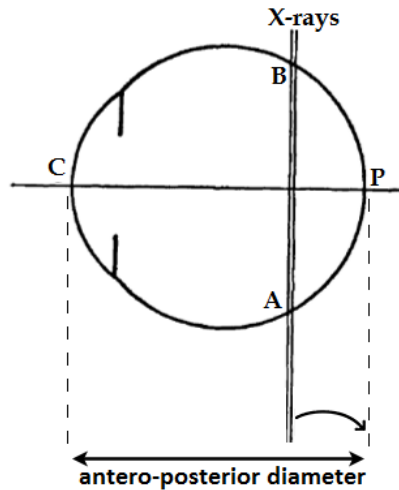
Figure 1.1: Rushton's X-ray method for determining the axial length of the eye[1].

The disadvantages of this method were obvious: besides the lack of precision and the reliance on the subject's description, X-rays' potential hazard was known since the beginning of the century.

A new approach was developed by G. J. Schoute in 1940, this time by means of chromatic aberration. In his work, he found that there was a directly proportional relation between the length of the optical axis and the apparent distance between two differently colored objects in alignment with a prolongation of the axis. Although this method was noninvasive and did not expose the eye to any radiation, it did not prove to be entirely reliable nor accurate.

Significant progress only emerged in 1961 by S. Franken[2], with an innovative method based on ultrasonic echo-impulses. In this technique, the time that an ultrasonic pulse takes to travel to an interface and be reflected back was measured, from which the path traveled was deduced. To do so, it was used a crystal that converted electric vibrations of suitable frequency into mechanical vibrations, and another crystal that did the reverse, transposing sonic or ultrasonic vibrations into electrical frequencies. Both the emitted and the echoed pulse were made visible on a cathode-ray oscillograph. By knowing the time delay between these signals and the

characteristics of the transversed medium, it is possible to deduce the path length which corresponds to the length of the optical axis of the eye. However, there were some drawbacks, such as the limited transversal resolution of the ultrasound beam and the need for mechanical contact between the transducer and the eye to allow the propagation of the sonic wave. Despite being used for decades as a standard clinical technique to determine the adequacy of implant lenses, due to its inadequacy for human eyes, different approaches were explored.

The measurement of ultrasonic echo-impulses inspired researchers to come up with a similar approach, but using light waves instead of sound waves. The use of shorter wavelengths would permit imaging at a higher resolution and light requires no contact medium to propagate. This new approach emerged firstly in 1971 by M. Duguay, who developed a technique for the display of picosecond light pulses[3]. Ultrashort (6 ps) green light pulses passing through a light-scattering medium were photographed from the side by a camera positioned behind a shutter of 10 ps framing time (Figure 1.2). The shutter was an ultrafast Kerr cell driven by $8ps$ infrared pulses. This experiment allowed the visualization of light pulses by simply observing their flight through a scattering medium from behind the shutter having a framing time equal to the time resolution desired (Figure 1.3).
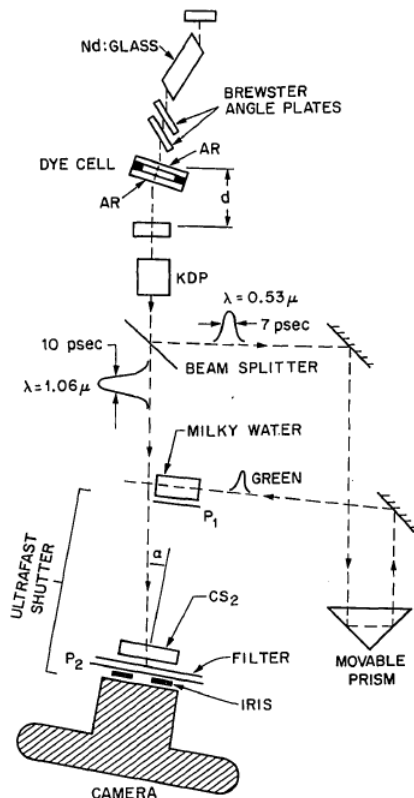
Figure 1.2: Experimental setup for photographing light pulses in flight. Movable prism provides for an adjustable delay line, so that as the nth pulse in the train traverses the water cell the shutter is being opened by the (n + 1)th infrared pulse[3].
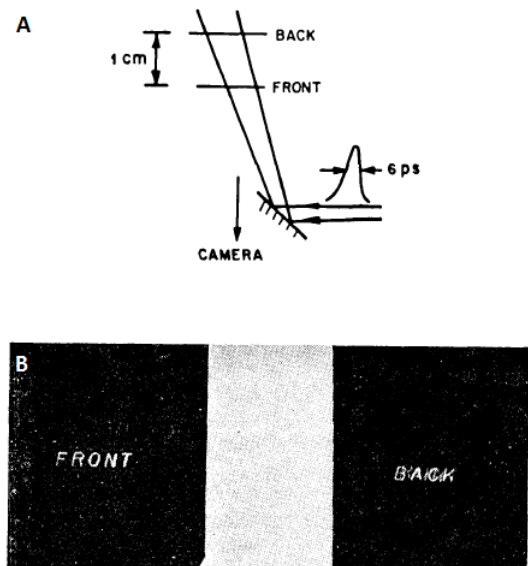
Figure 1.3: (A) Setup used to picture two glass slides on which the words front and back had been engraved. (B) Each slide is selectively photographed by properly adjusting the delay line in Figure 1.2[3].

Duguay recognized the medical potential of this technique, acknowledging that if subpicosecond pulses became available, it would permit picture ranging with submillimeter resolution which might allow seeing through the human skin.

In 1986, driven by the need of measuring the depth of corneal incisions by a

new mechanism based on argon-fluoride excimer lasers, J. G. Fujimoto developed a femtosecond optical ranging technique[4]. This approach can be considered an optical analogue of ultrasonic pachymetry (process of measuring the thickness of the cornea). It consisted on measuring the time required for a femtosecond laser pulse to make a round trip between the corneal surface and the bottom of the incision. This time can be converted to distance multiplying it by the speed of light. Because this physical constant is so great $(0.3\mu m/fsec)$, femtosecond pulses are necessary if longitudinal resolution in order of microns is to be achieved.
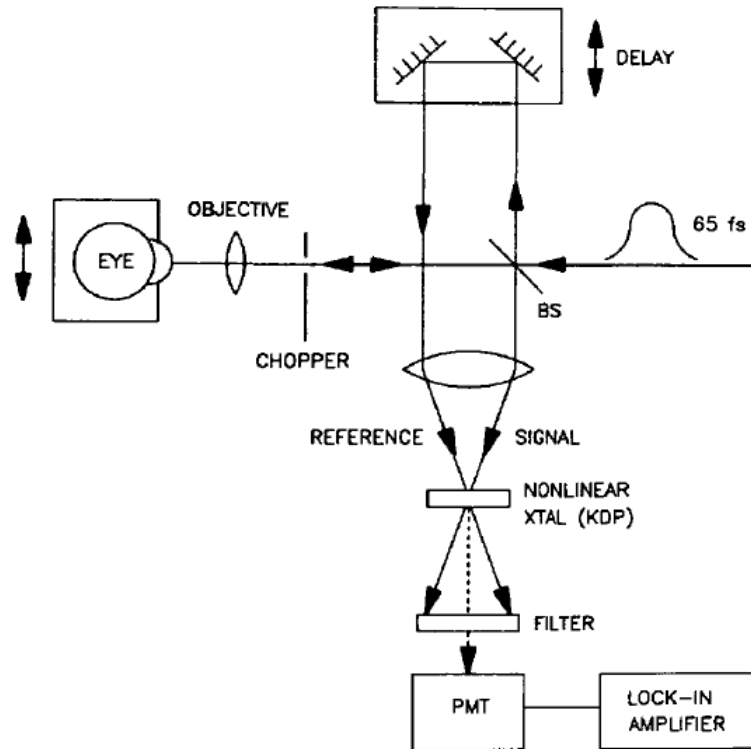
Figure 1.4: The cross-correlation apparatus used for femtosecond optical ranging. (BS = beam splitter, PMT = photomultiplier tube)[4].

As can be seen in Figure 1.4, a backscattered and a reference pulsed light are cross-correlated in a non-linear crystal. The non-linear mixing process creates an ultrahigh speed optical gate and generates a second harmonic pulse from which it is possible to measure the intensity and time delay of the desired optical signal. The second harmonic signal generation requires that both signals are matched in time, which is made by adjusting the delay mirrors. The filter blocks the signal and reference pulses and transmits the second harmonic generated by the non-linear crystal. The chopper and lock-in amplifier increase the signal-to-noise ratio. By measuring the round-trip transit time of the light pulse between the anterior and posterior corneal surfaces, it is also possible to use this technique to determine corneal thickness. Longitudinal and transverse resolution were estimated to be of $5\mu m$ and $10\mu m$, respectively. Experimental results obtained by Fujimoto are shown in Figure 1.5-B.

Another approach for measuring the length of the optical axis *in vivo* using light waves and a Fabry-Pérot interferometer was developed in 1988 by A. F. Fercher, which he named interferometry with partially coherent light[5]. As opposed to the femtosecond technique, a statistically fluctuating light beam emitted by a semiconductor laser was used. Also, the cross correlation of the field's amplitudes of the measurement
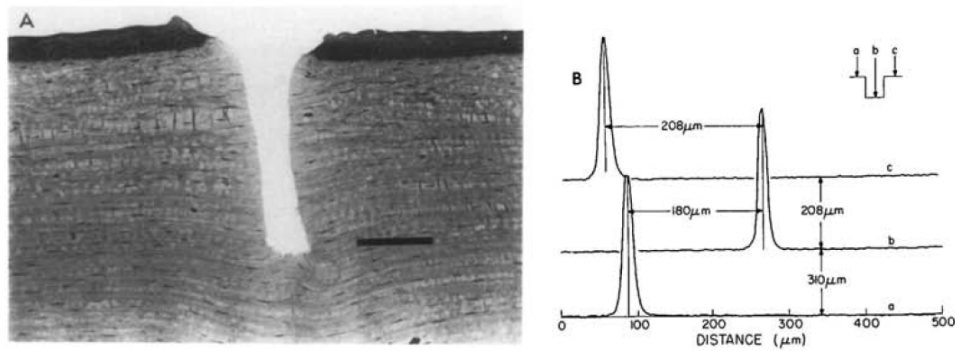
Figure 1.5: (A) Histologic section of a shallow corneal incision created by an excimer laser. (B) Femtosecond optical ranging of this incision. For traces a and c the probe beam was focused on the corneal surface while for trace b it was focused into the incision [4].

beam and the reference beam was used, rather than that of the intensities. Because the used laser emitted more than 10 freely oscillating radiation modes it could be considered to have, to a good approximation, statistically stationary fluctuations. In this case the light beam is a train of random light pulses with fluctuating amplitudes and phases. If the delay path length equals the measurement path length, interference will be seen and can be used as an indicator for the path-length matching. An estimate of the resolution can be obtained by considering the length of the corresponding light pulses. This method succeeded in measuring the optical length of the eye within a precision of 0.03 mm. The experimental setup is presented in Figure 1.6.
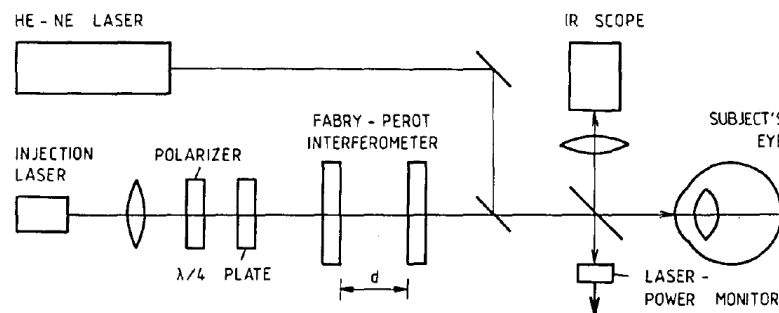
Figure 1.6: Optics of the interferometer used to measure the length of the optical axis of the human eye *in vivo* [5].

A He-Ne laser is used only to adjust the position and alignment of the subject's eye and the interferometer. When the correct position is achieved, interference rings are visible in the IR scope (Figure 1.7). Interestingly, these rings pulsate with the subject's heart beat. This interference pattern is caused by the superposition of the light beam reflected at the inner sclera with the light beam reflected at the anterior surface of the cornea (Figure 1.8).

New significant progress occurred in 1991, when X. Clivaz applied, for the first time, optical low-coherence reflectometry (OLCR) to investigate diffusive biological tissues (samples of fresh arteries) with a single-mode fiber probe [6]. This method allowed the determination of optical parameters such as the index of refraction, transmission properties and the tissue thickness. This technique was based on coherent cross-correlation detection of light reflected from the sample, using a Michelson interferometer with a broadband light source of short coherence time. As can be seen in Figure 1.9-A, a light-emitting diode (LED) is used as a continuous light source. The interferometer is built with single-mode polarization-maintaining fiber and a

Figure 1.7: Interference phenomenon observed when the Fabry-Perót plate distance matches the optical length of the eye.[5].
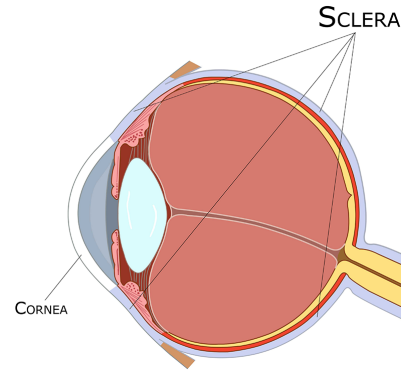
Figure 1.8: Position of the cornea and sclera in the human eye.

50:50 coupler (PMC). The sample (SAM) is mounted at the end of the measurement arm, either close to or in contact with the fiber and a mirror is mounted on a stepper translator at the end of the reference arm (REF). A phase modulation at -117 Hz is generated by a 3 cm long piezoelectric element (MOD) that stresses the fiber on the reference arm. The interference signal is then detected by an InGaAs photodiode (PD). The measured physical value is the interference term of the optical power P_i reaching the detector as a function of the round-trip propagation time of the light τ in the reference arm of the interferometer, obtained indirectly by recording the position of the mirror.
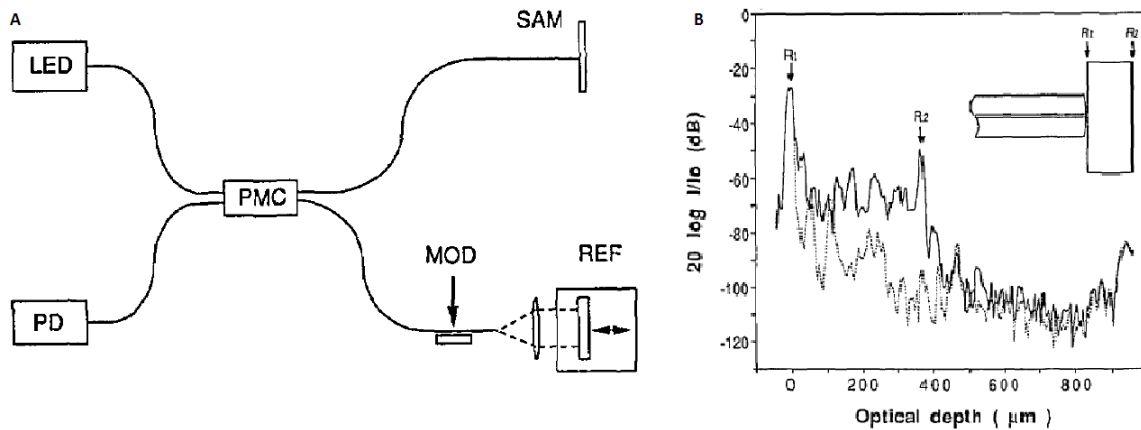
Figure 1.9: Schematic of the experimental setup for OLCR measurements[6]. Reflection signal as a function of the optical depth in a logarithmic representation[6].

Experimental results obtained are presented in Figure 1.9-B. The dotted curve represents the normalized reference curve from the bare fiber in air and the solid curve represents arterial wall in contact with the fiber end. R1 and R2 are reflections in the fiber-artery and artery-air interfaces, respectively. The two peaks are separated by a distance of 365 μm, corresponding to the measured displacement of the reference mirror.

Finally, later in 1991, optical coherence tomography (OCT) was first developed for noninvasive cross-sectional imaging in biological systems by James G. Fujimoto's group at MIT[7]. Similarly to OLCR, the heart of the system is the fiber optic Michelson interferometer illuminated by low-coherence light. However, instead of simply measuring optical distances, OCT also produces a two-dimensional image of

optical scattering from internal tissue microstructures. The conceived experimental setup is presented in Figure 1.10-A.
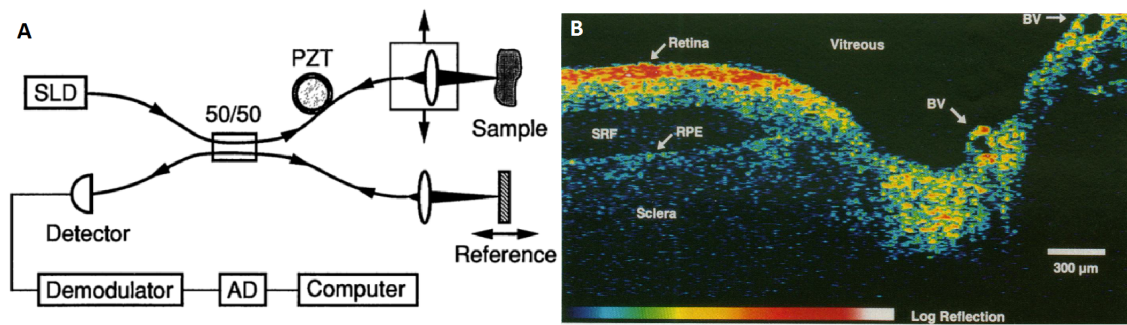
Figure 1.10: (A) Schematic of the OCT scanner [7]. (B) Optical coherence tomography of human retina and optic disk *in vitro*. (BV = blood vessel, SRF = subretinal fluid, RPE = retinal pigment epithelium) [7].

The superluminescent diode (SLD) output at 830 nm is coupled into a single mode fiber and split at the 50:50 coupler into the sample and reference arms. Reflections from these two arms are again combined at the coupler and detected by the photodiode. Longitudinal scanning of the sample is performed by translating the reference mirror with a stepper motor. The piezoelectric transducer (PZT) in the sample arm further provides phase modulation to the interferometric signal. Interferometric modulation of the output intensity is detected by the photodetector when the reference and sample arm delays are nearly matched. The detector output is demodulated to produce the envelope of the interferometric signal, which is then digitized (AD) and stored on a computer. The lateral beam position is translated after each longitudinal scan. Experimental results obtained are shown in Figure 1.10-B.

Because of its versatility, Huang recognized OCT as a promising technique for both basic research and clinical applications. In the following section, the optical principles behind OCT functioning will be exposed in detail.

1.2 Physical Principles and Optical Properties

As previously claimed, to successfully develop work in OCT's data acquisition it is vital to understand the preceding fundamental processes, which will now be covered. In certain parts of this topic, a significant amount of mathematical explanation is required and thus will be presented. However, the reader is meant to be able to understand the exposed principles even without giving great consideration for the mathematical analysis.

1.2.1 Coherence

A short description of coherence would be the measurement of the degree of phase correlation that exists in the radiation field of a light source at different locations

and different times[8]. In a more strict approach, it can be described in terms of temporal coherence and spatial coherence. While temporal coherence is a measure of the degree of monochromaticity of the light, spatial coherence is a measure of the uniformity of phase across the optical wavefront. This matter is easier to understand resorting to a graphical approach. Let us then consider the monochromatic punctual light source in Figure 1.11.
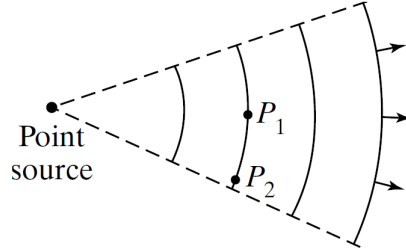
Figure 1.11: Portion of the wavefronts associated with a perfectly coherent light field produced by an ideal monochromatic point source[8].

The electromagnetic field produced by this ideal source can be considered to have perfect temporal and spatial coherence. The temporal coherence is perfect because, since the wave has a single frequency, the knowledge of the phase at a given point P_1 and a given at time t_1 allows one to predict with complete confidence the phase of the field at that same point at a later time t_2. If the frequency of the point source varied in a randomly, temporal coherence would be reduced.

The spatial coherence of the wavefield is also perfect since along each wavefront there is no relative variation of the field's phase. Thus, the knowledge of the phase at point P_1 at time t_1 allows one to predict with perfect confidence the phase of the field in this same instant at a spatially distinct point P_2 along the same wavefront. If there were several nearby point sources emitting light of the same frequency but with random relative phases, the spatial coherence of the resulting wavefield would be reduced.

The coherence length l_c of a light source is defined as[9]:

$$l_c = \frac{4\ ln(2)}{\pi} \frac{\lambda_0^2}{\Delta\lambda} \tag{1.1}$$

where λ_0 is the center wavelength and $\Delta\lambda$ is the bandwidth of the light source with a Gaussian profile. The Gaussian source approximation is convenient and well established in the OCT community.

Coherence time t_c can be easily obtained from 1.1 by relating l_c to the speed of light c[9]:

$$t_c = \frac{l_c}{c} = \frac{4\ ln(2)}{c\ \pi} \frac{\lambda_0^2}{\Delta\lambda} \tag{1.2}$$

Nonlaser light sources emit light primarily via the uncorrelated spontaneous emission of many atoms, resulting in the generation of incoherent light. In contrast, a laser source, by the nature of its stimulated emission, ensures both a narrow-band output and a high degree of phase correlation, generating in coherent light. However, OCT uses a low-coherence light source to generate the interference. This characteristic ensures that the interferometric signal is only observed over a limited depth of the sample, in order to achieve higher spatial resolution. Since interference is only observed when the path-lengths are matched to within a coherence length, the shorter the coherence length, the better the signal resolution will be[9]. In other

words, if a coherent light source was used, interference would occur over a wide range of path length differences, not allowing the detection of the desired optical echoes. For that reason, light sources in OCT must have a small coherence length, which is why this technique is said to rely on low-coherence interferometry.

1.2.2   Superposition of Waves

The superposition of waves is a fundamental principle of OCT imaging since it relates to the phenomena of polarization, interference and diffraction. All of them are present in the process of generating relevant data for subsequent acquisition, and its comprehension is essential.

The Principle of Superposition can be easily described as the property that suggests that the resultant disturbance at any point in a medium is the algebraic sum of the separate constituent waves[10]. In an algebraic method, this principle can be exposed considering the general wave equation:

$$E(x,t) = E_0 \sin[\omega t - (kx + \varepsilon)] \tag{1.3}$$

in which E_0 is the amplitude of the harmonic disturbance propagating along the positive x-axis. To separate the space and time parts of the phase, let us consider

$$\alpha(x,\varepsilon) = -(kx + \varepsilon) \tag{1.4}$$

thus obtaining:

$$E = E_0 sin(\omega t + \alpha) \tag{1.5}$$

Supposing then that we have two different waves described by:

$$E_1 = E_{01} sin(\omega_1 t + \alpha_1) \tag{1.6}$$

$$E_2 = E_{02} sin(\omega_2 t + \alpha_2) \tag{1.7}$$

The resulting disturbance is the linear superposition of these waves:

$$E = E_1 + E_2 = E_{01} sin(\omega_1 t + \alpha_1) + E_{02} sin(\omega_2 t + \alpha_2) \tag{1.8}$$

If we considerer the superposition of waves with the same frequency, i.e., $\omega_1 = \omega_2$, three different cases may occur. Figure 1.12 illustrates the case of constructive interference. Because E_1 and E_2 are in phase, the peaks of the waves occur at the same time and the amplitude of the resultant wave is simply the sum of the amplitudes of E_1 and E_2. Considering this, it can be described by:

$$E = E_1 + E_2 = (E_{01} + E_{02}) sin(\omega t + \alpha) \tag{1.9}$$
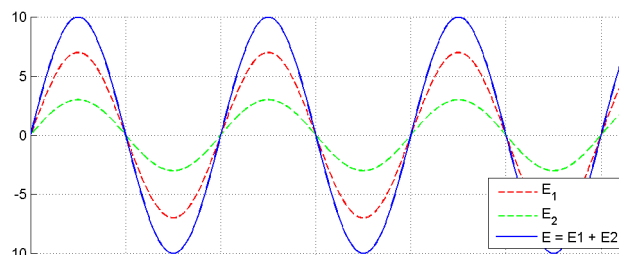
Figure 1.12: Constructive interference.

On the other hand, if the two superposing waves differ in phase by π (generally designated as being in antiphase), the peaks of one wave coincide with the troughs of the other, resulting in destructive interference. In this case, the amplitude of the resultant wave is equal to the difference in the amplitudes of E_1 and E_2. As the difference in their phase is an odd multiple of π, i.e., $\alpha_1 - \alpha_2 = (2m+1)\pi$, where m is an integer, the resulting wave can be written as:

$$E = E_1 + E_2 = (E_{01} - E_{02})sin(\omega t + \alpha_1) \tag{1.10}$$
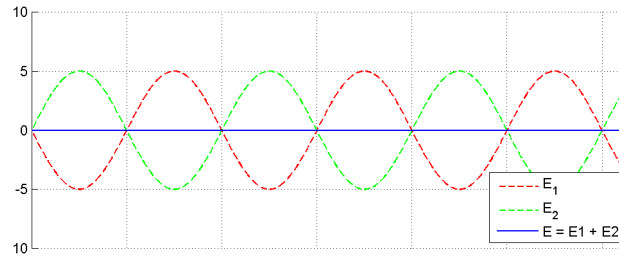
Figure 1.13: Destructive interference.

By analyzing Equation 1.10, we can conclude that if the superposing waves have have equal amplitude, the resulting disturbance is zero, as shown in Figure 1.13.

Finally, in the most general case, the superposing waves are neither in phase nor in antiphase. Consequently, the amplitude of the resulting wave is neither the sum nor the difference of the amplitudes of E_1 and E_2. Instead, it intermediates in magnitude between the magnitude of the sum and of the difference of the amplitudes of the waves being superposed.
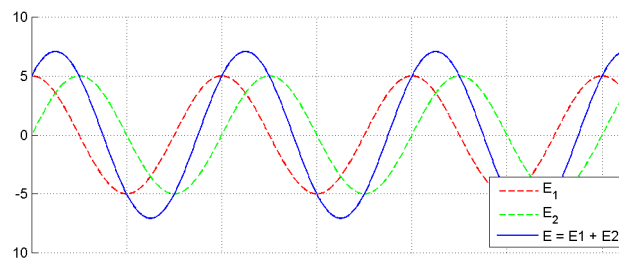
Figure 1.14: General superposition.

So far, only the superposition of waves of the same frequency has been discussed. However, realistically one never has light strictly monochromatic. In the best case, light can be considered quasi-monochromatic, being composed by a narrow range of frequencies. If the two superposing waves travel with different frequencies, a beat pattern is produced (Figure 1.15), with a beat frequency defined as $\omega_1 - \omega_2$. This type of superposition raises new concepts such as the distinction between group velocity, relating to the rate at which the modulation envelope advances and phase velocity, the rate at which the phase of the wave propagates in space.
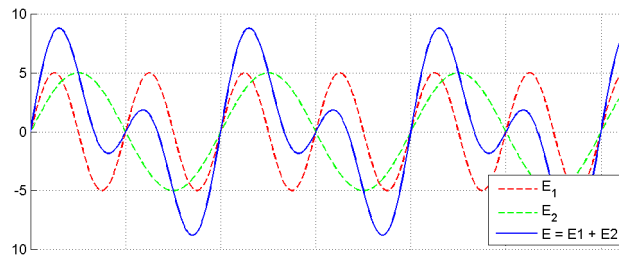
Figure 1.15: Superposition of two waves with the different frequency.

1.2.3 Light Polarization

Light polarization is an optical parameter used to describe the behavior of a wave's electric field in the plain perpendicular to the direction of propagation. It can be classified as linear, circular or elliptical.

Light in the form of a plane wave in space is said to be linearly polarized. If we envision the light propagating in the z direction and the transverse electric field exclusively in the x direction, the electric field can be represented by[11]:

$$\mathbf{E}_x(z,t) = \pm E_{0x}cos(kz - \omega t)\mathbf{i} \qquad (1.11)$$
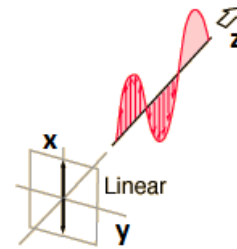
Figure 1.16: Side and end view of light polarization in a linear state.

If the light wave is composed by two plane waves of equal amplitude and differing phase in 90°, light is said to be circularly polarized:

$$\begin{aligned} \mathbf{E}(z,t) = &\pm E_{0x}cos(kz - \omega t \pm \varphi_x)\mathbf{i} \\ &\pm E_{0y}cos(kz - \omega t \pm \varphi_y)\mathbf{j}, \end{aligned} \qquad (1.12)$$

$$E_{0x} = E_{0y}; \quad \varphi_x - \varphi_y = \pm\tfrac{\pi}{2};$$
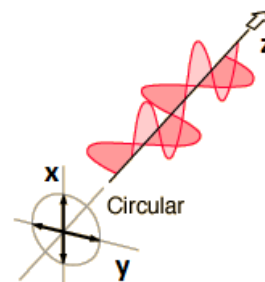
Figure 1.17: Side and end view of light polarization in a circular state.

When two perpendicular waves have unequal amplitudes, elliptically polarized light is produced (Figure 1.18).

By analyzing Equations 1.12 and 1.13 we conclude that circular polarization is in fact a special case of elliptic polarization, which is the most common case. Physically this means that as light rotates around the x and y axis, its irradiance

$$\mathbf{E}(z,t) = \pm\, E_{0x}cos(kz - \omega t \pm \varphi_x)\mathbf{i}$$
$$\pm\, E_{0y}cos(kz - \omega t \pm \varphi_y)\mathbf{j}, \qquad (1.13)$$

$$E_{0x} \neq E_{0y};$$
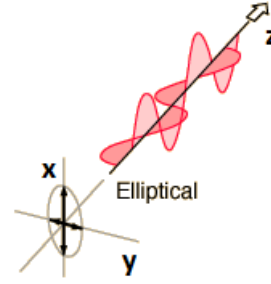
Figure 1.18: Side and end view of light polarization in a elliptical state.

varies. Therefore, as we look at the light coming from the source, it has an elliptical appearance with respect to rotation around the z axis[11].

1.2.4 Interferometry

Interference can be considered the most fundamental physical principle in OCT. In fact, the intensity of interference signals is what is measured in order to assess the backreflection intensity indirectly, since due to the high speed of light propagation it is not possible to directly measure it.

As seen in section 1.2.2, light obeys to the principle of superposition. Accordingly, the resultant electric-field intensity, at a point in space where two or more lightwaves overlap, is equal to the vector sum of the individual constituent disturbances. Briefly then, optical interference corresponds to the interaction of two or more lightwaves yielding a resultant irradiance derived from the sum of the component irradiances[10]. When conditions of enhancement, resulting in constructive interference, and diminution, resulting in destructive interference, alternate in a spatial display, the interference produces a pattern of fringes, which actually can be found in a multitude of phenomena[8].

So, in order to produce the desired interference, OCT must use an interferometer. The setup used is based on the Michelson interferometer (Figure 1.19).
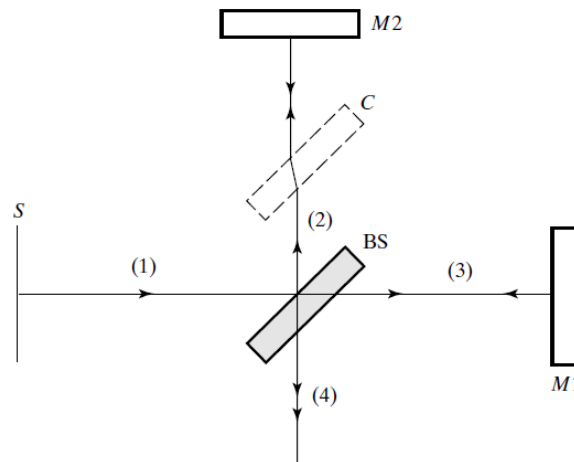
Figure 1.19: The Michelson interferometer[8].

From a light source S, beam 1 is split by a beam splitter BS by means of a thin,

semitransparent material, resulting in a reflected beam 2 and a transmitted beam 3, of roughly equal amplitudes. These beams reach the perfectly reflecting mirrors M2 and M1, respectively, where their directions are reversed. On their return to the BS, beam 2 is now transmitted and beam 3 is reflected, so that they come together again and leave the interferometer as beam 4. The aperture of this double-beam interferometer is such that all rays striking M1 and M2 will be perpendicular, or nearly so. Thus, beam 4 includes rays that have traveled different optical paths and will demonstrate interference. At least one of the mirrors is movable along the direction of the beam, allowing the gradual variation of the difference between the optical paths of beams 2 and 3. Notice that beam 3 traverses the beam splitter three times, whereas beam 2 traverses it only once. In order to make the optical paths of the two beams precisely equal, a compensator plate C made of the same material and dimensions as BS is inserted parallel to BS in the path of beam 2. Any small remaining inequalities in optical paths can be removed by allowing the compensator to rotate, thus varying the optical path through the thickness of its glass plate[8].

1.2.5   Interaction of Light with Matter

So far, it was mostly described the intrinsic behavior and properties of light when propagating in vacuum. However, in any OCT system light will be traveling through optical fibers, air and the material that composes the sample being analyzed, which in our case is ultimately biological tissue. In these cases, there is an interaction of light photons with particles from the surrounding medium which motivate different phenomena that alter the behavior of light that would otherwise be expected.

OCT imaging only makes sense when light manages to get through to the examined layers of the sample and back outside to the detection system. Since optical fibers are fabricated to transport light while minimizing unwanted effects of the interaction of light with matter, the biggest impact of this happens when light reaches and passes through the biological tissue being sampled.

The most relevant cases of interaction will be addressed in order to understand how they affect OCT development, imaging performance and what techniques are used to minimize their negative impact.

Dispersion

The origin of this physical phenomenon is the fact that the refractive index of a material is frequency dependent. As a result, when light passes through a medium, different wavelengths will travel at different speeds, an effect known as dispersion.

This effect is sometimes intentionally used in certain applications, such as the case of light decomposition into its frequency components when passing through a prism. As light is directed at a certain angle, the angle at which it leaves the prism is dependent on the refractive index and therefore the frequency.

However, dispersion often has a negative impact on imaging applications. As previously discussed (1.2.2 Superposition of Waves), when light is composed by different wavelengths it travels with a certain group velocity. This makes it vulnerable to velocity group dispersion, which affects light as it enters tissue rather than when reflecting off a mirror. As a consequence of this dispersion, different wavelengths

return at slightly different times. The broader the bandwidth, the greater are the effects of dispersion. If dispersion is too great, light from the reference and sample arm will no longer interfere in a useful way for OCT functioning[11]. For this reason, dispersion is a factor that should be taken into consideration, and is generally compensated in OCT systems.

Absorption and Scattering

Typically, the optical properties of a tissue are characterized by the absorption and scattering coefficient[12].

The explanation of the frequency dependence of the refractive index can be found by examining the interaction of an incident electromagnetic wave with the array of atoms composing a dielectric material. An atom can react to incoming light in two different ways, depending on the incident photon's frequency. Generally, the atom will "scatter" the light, redirecting it without otherwise altering it. But if the photon's energy matches that of one of the excited states, the atom will absorb the light, making a quantum jump to a higher energy level[10].

Because of this close relation between these physical processes, both will be addressed in this same section. We will start with absorption.

When an electron interacts with light, it absorbs the energy of a photon of specific frequency and goes into a higher energy state. An electron from a given atom or molecule can only receive photons of a specific frequency or energy. In OCT, imaging is performed in the near-infrared (NIR) region and generally involves electrons in bonds. These bonds have quantum mechanical vibrational or rotational states and the absorption of a photon causes the bond to go to a higher energy state[11].

Absorption, dispersion, and refractive index are closely related. Figure 1.20 shows a plot of frequency versus real refractive index, which describes energy storage and hence affects the speed of light in a medium[13]. At the resonance frequency ω_0, absorption will occur. However, as ω approaches the resonance frequency, the real refractive index changes rapidly. This is because the energy is not absorbed but re-radiated at a different phase. Furthermore, since the real refractive index changes rapidly near the absorption peak, dispersion is particularly prominent.
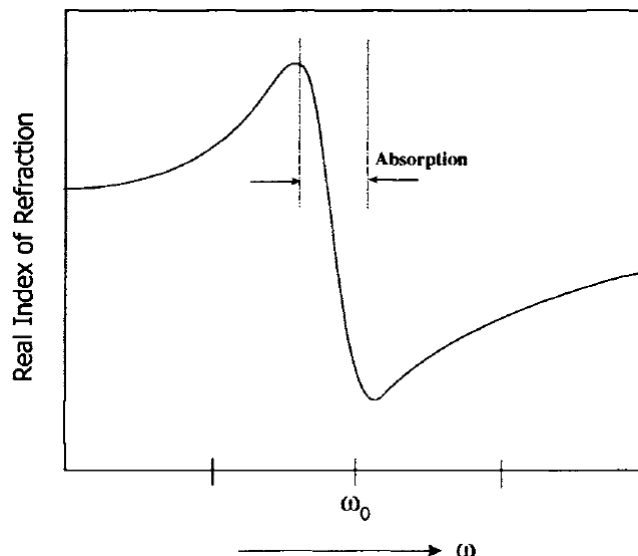
Figure 1.20: Plot of frequency versus real refractive index[11].

A light-absorbing medium will absorb a fraction of incident light per incremental path length of travel within the medium. The absorption coefficient $\mu_a(cm^{-1})$ is defined as[13]:

$$\mu_a = -\frac{1}{T}\frac{\partial T}{\partial L} \tag{1.14}$$

where T (dimensionless) is the transmitted fraction of the incident light after an incremental path length $\partial L(cm)$. This fractional change $\partial T/T$ per ∂L yields an exponential decrease in the intensity of light as a function of an increasing path length L[13]:

$$T = e^{-\mu_a L} \tag{1.15}$$

In the case of retinal OCT imaging, the absorption in water plays an important role since it is the main absorber at visible and NIR (approximately 700–2000 nm) wavelengths (Figure 1.21).
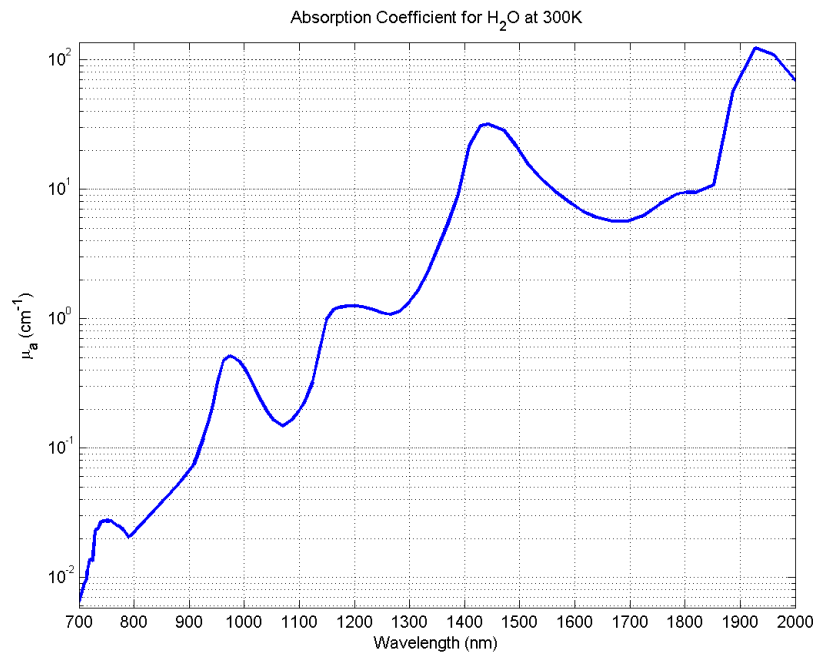
Figure 1.21: Absorption coefficient for distilled water at 300 K dependency on wavelength, in logarithmic representation. Based on experimental data from[13].

Considering the average axial length of a rat's eye to be 5.98 mm[16], and that in an OCT exam light would traverse it twice, we can make a simple model of this sample by considering it consist of approximately 12 mm of water. Applying Equation 1.15 to the experimental data presented in Figure 1.21, we can calculate the fraction of light that would be transmitted in this model of the rat's eye (Figure 1.22).

We verify that for wavelengths below 1100 nm the effect of absorption results in a negligible attenuation of the optical power. For wavelengths higher than 1300 nm this effect starts to be considerable.

Taking into account the influence of absorption in retinal imaging, it seems optimal to use light sources within the wave range of 700 nm to 1300 nm, in order to assure that light from the sampling beam is weakly absorbed before it gets to the
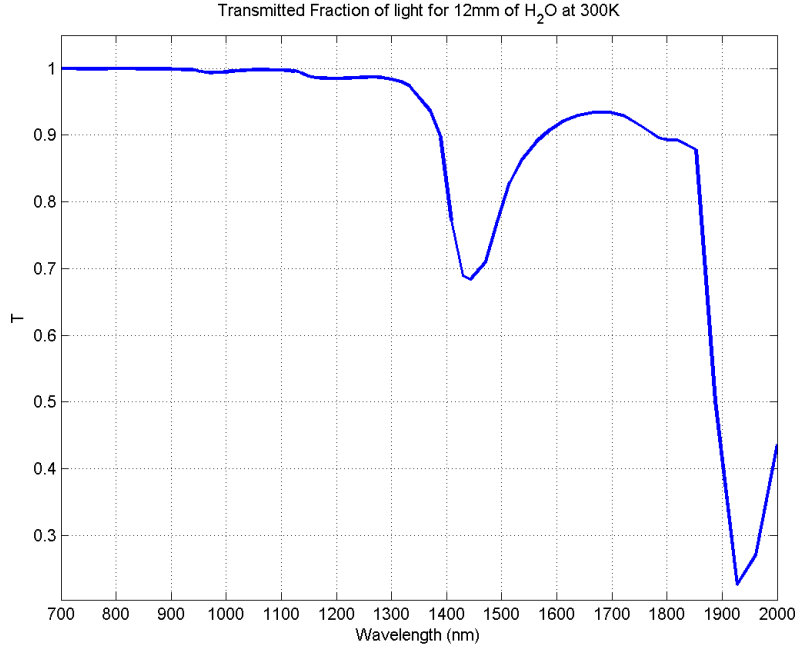
Figure 1.22: Transmitted fraction of the incident light through $12mm$ of water, simulating a rat's eye. Based on data from Figure 1.21 and Equation 1.15.

detector. However, a precise optimal choice of the spectral range depends on the application in which OCT imaging is meant to be used.[15].

For a generic tissue, other than the eye, other absorbers are more relevant than water at visible and NIR wavelengths, such as blood, bilirubin, fat, and melanin[13].

Having addressed the absorption phenomenon we will now turn to scattering, which is one of the fundamental principles for OCT imaging.

With scattering, there is no energy transformation, but a change in the spatial distribution of the energy, as photons are forced to deviate from a straight trajectory by force of the collisions they suffer while passing through tissue and interacting with its microstructures. As a result, scattered light consists of a photon that sails off in some direction carrying the same amount of energy as the incident photon (elastic scattering)[10].

Optical scattering can be theoretically described either as scattering by particles that have a refractive index different from the surrounding medium, or as scattering by a medium with a continuous but fluctuating refractive index. Both descriptions are adjusted to match experimental data and hence both are valid descriptors for the scattering behavior of tissues.[13].

The scattering coefficient μ_s is the factor that expresses the attenuation caused by scattering in units of reciprocal distance, which can be written as[12]:

$$\mu_s = \frac{\mu'_s}{1 - g} \tag{1.16}$$

where μ'_s is the reduced scattering coefficient and g is the anisotropy factor of scattering. For many tissues in the visible and NIR region the tabled anisotropy factor is $g = 0.9$[12].

A suitable fit for reduced scattering coefficient μ'_s, which is not exhaustive but sufficient to characterize the behavior of tissues such as skin, brain, breast, bone

and fatty tissues, can be given by[13]:

$$\mu_s' = a\left(\frac{\lambda}{500\ (nm)}\right)^{-b} \tag{1.17}$$

where the wavelength λ is normalized by a reference wavelength, $500\ nm$, to yield a dimensionless value, which is then raised to a power b, called the "scattering power". This term characterizes the wavelength dependence of μ_s'. The factor a is the value $\mu_s'(\lambda = 500\ nm)$ which scales the wavelength-dependence term. These terms are empirically obtained, and some values present literature are presented in Table 1.1

Tissue	Skin	Brain	Breast	Bone	Fatty tissue
a (cm^{-1})	46.0	24.2	16.8	22.9	18.4
b	1.421	1.611	1.055	0.716	0.672

Table 1.1: Parameters specifying the reduced scattering coefficient of different tissues, obtained by an average of data from different authors. (Adapted from a more extensive table[13]).

OCT has been used to measure the scattering coefficient of tissues μ_s, by several authors[17][18][19], being one reliable and powerful tool in the determination of such biological tissue properties.

Optical Penetration Depth

The penetration depth of light into a biological tissue is an important parameter that should be previously known before an OCT exam, since it determines how far into the tissue we can hope to acquire information. It is also relevant in other tests or medical exams, as for the determination of the irradiation dose in photothermal and photodynamic therapy of various diseases[20].

In biological tissue, the imaging depth is limited by both absorption and scattering, discussed in the previous section. An estimation of light penetration depth δ in tissue in terms of the effects of absorption and scattering can be considered by[12]:

$$\delta = \frac{1}{\sqrt{3\mu_a(\mu_a + \mu_s')}} \tag{1.18}$$

The dependence on the source's wavelength in Equation 1.18 is present in the terms μ_a and μ_s', as afore presented. Results from calculation of the optical penetration depth using Equation 1.18 with absorption and reduced scattering coefficient reference values have been determined for human skin by A. N. Bashaktov[12] for visible and NIR light (Figure 1.23).

Ultimately, it is the light source's wavelength that determines the achievable penetration depth in an OCT system. In non-transparent biological tissues high resolution images have been obtained at depths between $1\ mm$ and $3\ mm$ depending on the wavelength of the light source used and the opacity of the tissue[9][17][18][19].

Besides the inevitable source's wavelength restriction on the imaging depth of OCT systems, other artifacts may affect it. The most common and relevant are: optical attenuation, depth of focus and sensitivity roll-off[21]. Optical attenuation derives from the fact that OCT only detects singly-scattered light and beyond a certain penetration depth essentially all of the incident light will have been repetitively scattered, restricting the potential imaging depth. For biological tissues imaging at
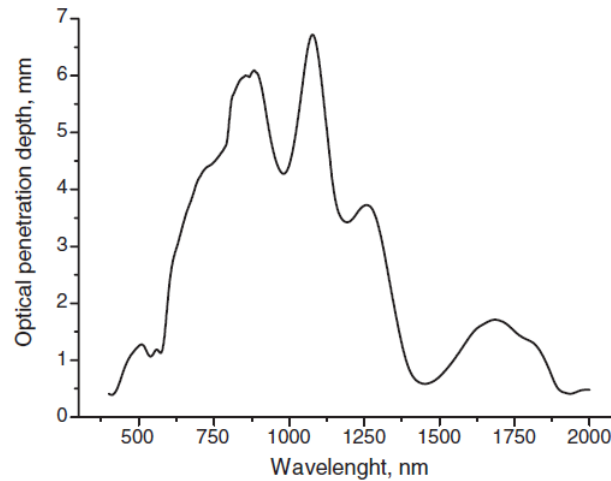
Figure 1.23: The optical penetration depth of light into human skin over the wavelength range from 400 to 2000 nm. The maximal penetration depth 3.5 mm is observed at the wavelength 1090 nm[12].

NIR optical wavelengths, optical attenuation typically limits the usable imaging range to $1 - 2$ mm[21]. Additional imaging depth limitation may arise from the trade-off between depth of focus and lateral resolution. The sensitivity roll-off artifact also limits the imaging depth, but we will leave this discussion for section 1.5 - Imaging Artifacts.

1.3   Theoretical Formulation and Operation Principles

The theoretical formulation of data acquisition in OCT will now be addressed. An overview of the entire processes that occur from the moment light exits the light source to the moment data is acquired will also be exposed.

The basic setup of an OCT systems consists of a Michelson interferometer using a low-coherence light source as presented in Figure 1.24.

Light from a low-coherence source is directed into a 2x2 optical coupler, implementing the Michelson interferometer. The coupler may or may not split the incident optical power evenly between the reference and sample arms, according to the design that most benefits the practical application of the OCT system. Light exiting the reference fiber is incident upon a highly reflective mirror, causing a reference delay and then redirected back into the same fiber. Light exiting the sample fiber is incident upon a scanning mechanism, e.g. a galvanometer mirror system, designed scan the focused spot in one or two lateral directions of the sample[22]. Light backscattered or reflected from the sample is also redirected back through the same optical scanning system into the sample arm fiber. The mixing of the returning sample light beam with the returning reference light beam happens in a fiber coupler, either the one used previously to split the light or another one used exclusively to make the light beams interfere. Finally, the interference signal is redirected also through optical fibers into a detector, so that the data acquisition process can begin.

To describe OCT mathematically it is useful, for simplification purposes, to

Figure 1.24: Schematic of a generic fiber-optic OCT system[22] (adapted). Black lines represent fiber-optic paths, red lines represent free-space optical paths, green lines represent electronic signal paths and the blue line represents digital data transfers. Inside the dashed gray line are the blocks that make the data acquisition system.

express the electric field $E(\omega, t)$ in its complex exponential form[9]:

$$E(\omega, k, t) = s(k, \omega)e^{-i(\omega t + kz)} \qquad (1.19)$$

This equation is a plane polarized solution to the wave-equation, with source field amplitude spectrum $s(\omega, k)$, time variation t, distance z, angular frequency ω and wavenumber k . The last two account respectively for the temporal and spatial frequencies of each spectral component of the field with a wavelength λ and are given by:

$$\omega = 2\pi\nu \qquad (1.20)$$

$$k = \frac{2\pi}{\lambda} \qquad (1.21)$$

In turn, the wavelength λ and the frequency ν are coupled by the relation[22]:

$$\lambda\nu = \frac{c}{n(\lambda)} \qquad (1.22)$$

Where $n(\lambda)$ is the refraction index (which is wavelength dependent in a dispersive media) and c is the speed of light in vacuum.

The electrical field in each optical part of the interferometer is denoted by E_{in}, E_{out}, E_{ref} and E_{samp}, corresponding respectively to the input, output, reference and sample arms (as shown in Figure 1.24). Let us consider that as the fiber coupler splits

the light beam, it has a reference arm intensity transmittance T_{ref} and a sample arm intensity transmittance T_{samp} that relate in such way that $T_{ref} + T_{samp} = 1$. Let us also assume, for simplification purposes, that the reference mirror is ideal, having a reflectance of 100%, and that the interferometer is operating in air.

Making the above assumptions it is possible to write the component optical fields in terms of the input field[9]:

$$E_{in}(\omega, k, t) = s(\omega, k)e^{-i\omega t} \tag{1.23}$$

$$E_{ref}(\omega, k, t, \Delta z) = (T_{ref}T_{samp})^{1/2} \; E_{in} \; e^{-i\phi(\Delta z)} \tag{1.24}$$

$$E_{samp}(\omega, k, t) = (T_{ref}T_{samp})^{1/2} \; E_{in} \; H(\omega) \tag{1.25}$$

$$E_{out}(\omega, k, t, \Delta z) = E_{ref} \; + E_{samp} \tag{1.26}$$

The second term in the exponential of Equation 1.19 simply accounts for the phase throughout the interferometer. This term can be dropped from the input electric field (Equation 1.23) because the input phase is arbitrary, and the interferometer only measures the relative output phase between the two optical paths.

The factor $\phi(\Delta z)$ in the reference arm electrical field (Equation 1.24) is the phase accumulated by translating the reference mirror by a geometric distance Δz[9]:

$$\phi(\Delta z) = \frac{2\,\omega\,n_{air}\,\Delta z}{c} = 2\,\omega\,\Delta t \tag{1.27}$$

The factor of 2 arises from the Michelson interferometer configuration, where the path length change equals twice the distance the reference mirror is displaced. Δt is the corresponding optical time of flight, which relates to the translated distance Δz by:

$$\Delta z = \frac{\Delta t\,c}{n_{air}} \tag{1.28}$$

The term $H(\omega)$ in the sample arm electrical field (Equation 1.25) is the frequency domain response, which describes the overall reflections from all reflective structures of the sample in the z direction, accounting for the phase accumulation therein. It is given by[9]:

$$H(\omega) = \int_{-\infty}^{\infty} r_s(\omega, z)\; e^{i\,2\,n(\omega,z)\,\frac{\omega}{c}\,z}\; dz \tag{1.29}$$

$n(\omega, z)$ is the frequency dependent and depth varying group refractive index, and $r(\omega, z)$ is the backscattering coefficient from the sample structural layers. Both of these variables are characteristics of the sample. A discrete approximation of Equation 1.29 can be written by modeling the sample as a summation over a countable number N of individual reflective layers in the sample, and assuming a negligible dispersion[9]:

$$H(\omega) = \sum_{j=1}^{N} r_{s_j} \exp\left\{ i\,2\,n(\omega, z)\,\frac{\omega}{c}\,\sum_{m=1}^{j} n_m z_{s_m} \right\} \tag{1.30}$$

Here, z_{s_m} is the thickness of the mth sample's layer, with a group refractive index n_m. The electric field reflectivity of each layer r_{s_j} can be determined applying the Fresnel's equations[9]:

$$r_s = \frac{n_{j+1} - n_j}{n_{j+1} + n_j} \tag{1.31}$$

Where n_j is the refractive index of each layer j.

An OCT system aims for the mathematical description of the sample's depth profile. This profile is given by the function $r_s(z_s)$, accounting for continuous change of the reflectivity r_s as a function of the corresponding distance from the beam splitter (or other arbitrarily chosen distance) z_s. This depth dependent electric field reflectivity profile in the sample is given by a series of N discrete, real delta-function reflections[22]:

$$r_s(z_s) = \sum_{j=1}^{N} r_{s_j} \delta(z_s - z_{s_j}) \tag{1.32}$$

The reconstruction of the function $r_s(z_s)$ from interferometric measurements is the goal of low-coherence interferometry in OCT[22]. To understand how it is achieved it is necessary to analyze the mathematical formalism surrounding the operation of the detector. In an OCT system the detector is a square law intensity device, i.e. it measures light intensity proportionally to a time average of the product between the detected electric field and its complex conjugated[9][22]:

$$I_D(\omega, k, \Delta z) = \frac{\rho}{2} \lim_{T \to \infty} \frac{1}{2T} \int_{-T}^{T} E_{out}(\omega, k, t, \Delta z) E_{out}^*(\omega, k, t, \Delta z) dt \tag{1.33}$$

Here, ρ is the responsivity of the detector (in A/W) and the factor of 2 accounts for the second pass of each field through the beam splitter. In brackets notation we can write it in a simpler way:

$$I_D(\omega, \Delta z) = \frac{\rho}{2} \left\langle E_{out}(\omega, k, t, \Delta z) E_{out}^*(\omega, k, t, \Delta z) \right\rangle \tag{1.34}$$

When we substitute E_{out} by its value given in Equation 1.26 the obtained equation is[9][22]:

$$I_D(\omega, \Delta z) = \frac{\rho}{2} \left(\underbrace{\left\langle E_{samp} E_{samp}^* \right\rangle}_{\text{sample self-interference}} + \underbrace{\left\langle E_{ref} E_{ref}^* \right\rangle}_{\text{reference self-interference}} + \underbrace{2 Re\{ \left\langle E_{samp} E_{ref}^* \right\rangle \}}_{\text{cross-interference}} \right) \tag{1.35}$$

As exposed in Equation 1.35, the intensity at the detector is given by a sum of three terms: the sample and reference self-interference and the real part of the complex cross-interference. By replacing in this equation the terms given by Equations 1.24 and 1.25 and by substituting the field spectrum by $S(k) = s(\omega, h)$ which encodes the power spectral dependence of the light source we obtain a real result for the detector current as a function of wavenumber, commonly known as the "spectral interferogram"[22]:

$$I_D(k) = \frac{\rho}{4} T_{ref} T_{samp} S(k) \left(\sum_{j=1}^{N} R_{s_j} + 1 \right. \qquad \textbf{DC Component}$$

$$+ 2 \sum_{j=1}^{N} \sqrt{R_{s_j}} \cos\left(2k \times (z_{ref} - z_{s_j})\right) \qquad \textbf{Cross-interference}$$

$$\left. + 2 \sum_{j \neq i=1}^{N} \sqrt{R_{s_j} R_{s_i}} \cos\left(2k \times (z_{s_j} - z_{s_i})\right) \right) \textbf{Self-interference}$$

$$\tag{1.36}$$

where $R_{s_{j/i}} = |r_{s_{j/i}}|^2$ is the corresponding power reflectivity, z_{ref} is the distance from the beam splitter to the reference arm mirror and $z_{s_{j/i}}$ is the distance from the beam splitter to each reflective layer j/i of the sample. The surface of the beam splitter was arbitrarily set as $z = 0$.

Several mathematical steps where necessary to obtain this resulting equation which were not presented here to avoid an exhaustive mathematical description. They can however be consulted in literature[22].

By analyzing Equation 1.36 we conclude that the spectral interferogram of the detector is represented as a sum of three distinct components: the DC Component, the Cross-Interference and the Self-Interference, which will be briefly described next.

- **DC Component** - The DC component of the interference signal is a constant pathlength-independent offset, having an amplitude proportional to the power reflectivity of the reference mirror plus the sum of the power reflectivity of each layer of the sample[22].

- **Cross-interference** - The cross-interference (or cross-correlation) component is the relevant component to measure in OCT imaging. It corresponds to the cross-correlation between returning reference and returning sample optical signals, for each reflector within the sample. This depends on both light source wavenumber and the difference in the optical path length of the reference and sample's layers. This component is typically smaller than the DC component. However, the square root dependence brings an important logarithmic gain factor, reason why OCT images can benefit from logarithm representation, being in fact a common practice in OCT imaging[22].

- **Self-interference** - Self-interference (or auto-correlation) terms represent interference signals originated in reflections within the different layers of the sample. As they do not represent desired information, this component is considered an artifact in OCT imaging. Since the auto-correlation terms depend linearly upon the power reflectivity of the sample exclusively, the greater the reflectivity of the reference mirror, the smaller this artifact will be when compared to the DC and cross-interference components[22].

For most biological tissues, reflectivities are typically very small ($\sim 10^{-4}$ to 10^{-5})[22]. For this reason the reference's electrical field typically dominates the sample's electrical field when reaching the detector. OCT systems use optically coated mirrors as a reference, which allows having a power reflectivity greater than 0.9999. That is why the reference mirror was approximated to a perfect mirror in this mathematical formulation. However, if we wanted to account for this factor, we should substitute in Equation 1.36 the term 1 in the DC component for R_{ref}, as well as include it inside the square root in the cross-interference component, writing $\sqrt{R_{ref} R_{s_j}}$ instead.

Figure 1.25 helps us having an visual general understanding of Equation 1.36 by analyzing different numbers of sample reflectors. For a single reflector, the self-interference component does not exist. So, a single cross-interference component rides on top of the DC component. The resulting spectrum is composed by a cosinusoid wave whose period is proportional to the distance between the sample and reference mirror. In the case of a sample with multiple reflectors, the cross-correlation component is added, which is a superposition of cosinusoids, each having a specific frequency and amplitude that are characteristics of the sample[22].
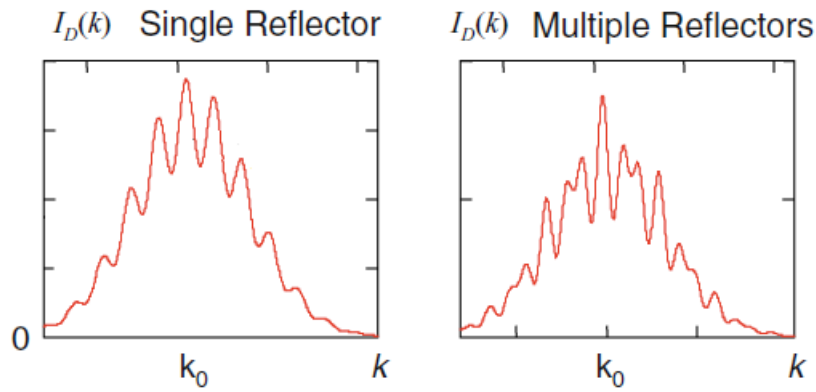
Figure 1.25: Comparison of a spectral interferogram between a sample with only one reflective layer (left) and a sample with multiple reflective layers (right)[22]. (Adapted).

Having addressed the optical principles behind the functioning of an OCT system, which allows relevant data to be generated, we will now focus on the complementary data acquisition (DAQ) system, which allows the generated data to be acquired, converting optical interference signals into useful and legible information to the user. The generic architecture of a DAQ system in OCT relies on the following units to acquire, process and display information to the user[23]:

- **Optical Detector** - Links the physical world to the electric version of it. In an OCT system it is responsible for converting the interference signals to proportional electric signals. Depending on the OCT functioning approach (which will be exposed in the next section) the detector used might be one photodiode or a detector array, namely Silicon Photodiode Arrays (PDA), Charged-Coupled Devices (CCD) or Complementary Metal-Oxide-Semiconductor (CMOS) image sensors. The use of detector arrays is restricted to an imaging OCT modality denominated Spectral Domain OCT, which will be explained ahead. The main differences between the three listed detector arrays is that the PDA is restricted to line (1D) imaging, as it is constituted only by of a linear array of photodiodes. A CMOS image sensor is based on a bi-dimensional array of photodiodes, allowing 2D imaging, and each pixel also contains transistors to buffer and amplify the collected photo-charge. In CCDs, the light to electron conversion mechanism is basically the same as in photodiodes with the main difference of the electric charges being stored in CMOS capacitors, and at regular time intervals the corresponding accumulated charge is transferred serially to the output of the device[24].

- **Signal processing and conditioning elements** - These include filters and amplifiers that shape the detected electric signal in order to optimize its acquisition. A simple example is the amplification and filtering of the signal to minimize its electric noise.

- **Acquisition Hardware** - It is the input of the measuring process, consisting on an interface that makes the conversions between the analogical electric signal domain to the digital domain using an Analog-to-Digital Converter (ADC). After this conversion, data is transfered to the host computer to be processed and displayed.

- **Acquisition Software** - Processes the acquired raw data for it to be displayed in a legible way to the user, either graphically or numerically. Most applications

of an OCT system require it to be imaging in real time. For that reason, of the most important acquisition aspects in an OCT DAQ system is the acquisition and processing speed. The acquisition software plays a fundamental role in the settlement of these parameters and therefore is organized to allow data acquisition, processing and display to happen as fast as possible.

- **Host Computer** - The data acquisition process requires the existence of a platform that ensures the control of the measuring process, the execution of the acquisition software and the visualization and storage of the acquired data. The host computer characteristics and specifications may influence important acquisition parameters such as acquisition speed, processing speed, data precision, and data storage capacity.

The sequential integration of the described stages in an OCT system is also represented in Figure 1.24.

1.4 Functioning Modalities

Information about the optical structure of the sample, which arises from Equation 1.36, can be obtained from measurements in both time or frequency domains. The differences in the experimental implementation of these two modalities, the implications such as imaging artifacts that derive from it and a comparison highlighting the benefits and handicaps of each one will be exposed throughout this section.

1.4.1 Time Domain

Time Domain OCT, commonly abbreviated in literature as TD-OCT, was the first modality implemented when the initial developments of OCT took place. The basic setup of a TD-OCT system is nowadays still based on the first OCT developed by James G. Fujimoto's group at MIT[7], and was already represented in Figure 1.10-A.

A TD-OCT system uses as light source a broadband continuous wave. The reference arm is scanned, altering the optical path length of the reference beam z_{ref} to match the different scattering layers of the sample, allowing the reconstruction of the sample's depth profile.

The interference patterns obtained for each of these layers can be described by integrating Equation 1.36 over all k [22]:

$$
I_D(k) = \frac{\rho}{4} \, T_{ref} T_{samp} \, S_0 \left(\sum_{j=1}^{N} R_{s_j} + 1 \right. \qquad \textbf{DC Component}
$$

$$
\left. + 2 \sum_{j=1}^{N} \sqrt{R_{s_j}} e^{-(z_{ref}-z_{s_j})^2 \Delta k^2} \cos\left(2k_0 \times (z_{ref} - z_{s_j})\right) \right) \textbf{Fringe Bursts}
$$

$$
(1.37)
$$

Here, $S_0 = \int_0^\infty S(k) \, dk$ is the result of the integration of the power source spectrum over k. The obtained result has again a component which refers to the DC part of the signal. The relevant component that describes the depth profile of the sample is given by the fringe burst component.

The depth profile of the sample is modulated by a cosinusoidal carrier wave at a frequency proportional to the source's center wavenumber k_0 and the difference between the reference and sample's optical paths $z_{ref} - z_{s_j}$. This difference represents the rapid oscillatory term of the cosine term of the fringe bursts component at Equation 1.37. The envelope of the carrier wave is the auto-correlation function defined by the exponential factor that gives a Gaussian shape to the interference signal and represents the slower oscillatory term (Figure 1.26-B). Since the reference arm length is typically scanned as a function of time, the difference $z_{ref} - z_{s_j}$ provides a convenient modulation frequency for lock-in detection, allowing high sensitivity detection of the reflectivity envelope and rejection of the DC offset[22].
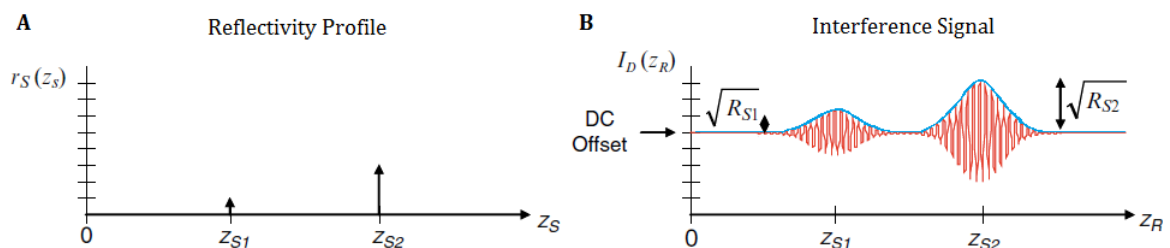
Figure 1.26: (A) Reflectivity profile $r_s(z_s)$ of an arbitrary sample, with two layers at z_{s_1} and z_{s_2}. (B) Simulation of the interference fringes that this sample would produce (red) and its envelope (blue)[22]. (Adapted).

As presented in Figure 1.26-B, the detected interference signal has a DC offset proportional to the sum of the sample's power reflectivities. Each scattering layer of the sample will produce an interference pattern with an amplitude of $\sqrt{R_{s_j}}$ to which is added the DC Offset. The required signal processing aims at detecting the envelope of the acquired fringe burst pattern, which would be the information visually displayed.

1.4.2   Fourier Domain

A more recent approach in OCT imaging gives an alternative to TD-OCT. It is the Fourier Domain OCT (FD-OCT). The popularity of this technique grew quickly, as it offered some advantages over the TD-OCT . We will leave this comparison to a further section and by now focus on the explanation of this functioning modality.

FD-OCT is actually more than a single imaging technique, because it can be implemented in two different ways, giving rise to two different OCT functioning approaches: Spectral Domain OCT (SD-OCT) and Swept Source OCT (SS-OCT). Both of them have common characteristics that differ them from TD-OCT. Namely, the fact that the reference mirror is now static. To reconstruct an approximation of the sample's reflectivity profile it is the wavenumber-dependent detector current $I_D(k)$ in Equation 1.36 that is directly captured and processed using Fourier analysis, which is the working base of FD-OCT[22].

However, SD-OCT and SS-OCT have divergences that are accentuated enough to be considered two different techniques, mainly in the characteristics of light source

used and the detection method. Both of these techniques will now be addressed with detail.

Spectral Domain

In SD-OCT, a continuous broadband source is used similarly to TD-OCT. However, as mentioned above, the reference arm path length is fixed and depth information is obtained by evaluating the spectrum of the processed interferogram by directing the returning light onto a detector array (PDAs, CMOS image sensors or CCDs, as previously described) placed at the output of a spectrometer, capturing all the components of $I_D(k)$ simultaneously[22]. A scheme of this basic setup is represented in Figure 1.27.
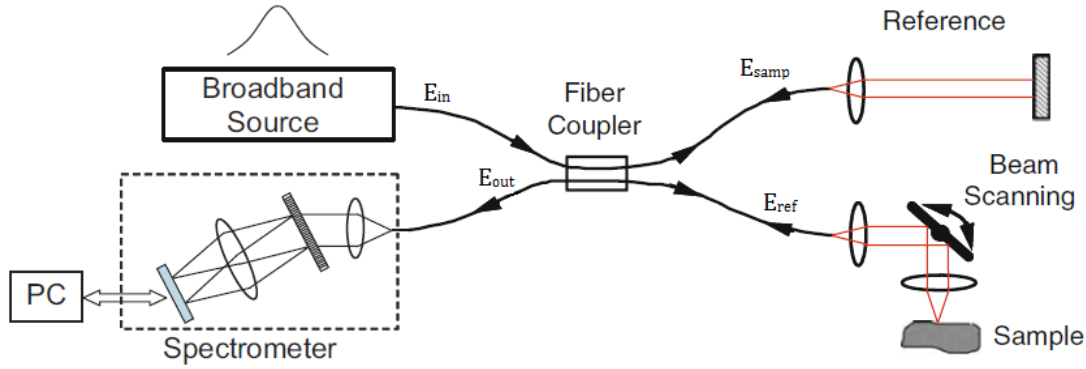
Figure 1.27: Basic setup of a SD-OCT system.

The sample reflectivity profile $r_s(z_s)$ can be estimated from the inverse Fourier transform of $I_D(k)$. To do so, it is necessary to consider the inverse Fourier transform of the normalized Gaussian function $S(k)$ which represents the spectral power and is given by $\gamma(z)$[22]:

$$\gamma(z) = e^{-z^2 \Delta k^2} \xrightarrow{FT} S(k) = \frac{1}{\Delta k \sqrt{\pi}} e^{-\left(\frac{k-k_0}{\Delta k}\right)^2} \tag{1.38}$$

Making use of the inverse Fourier transform of a cosine function (Equation 1.39) and the convolution property of Fourier transforms (Equation 1.40):

$$\frac{1}{2}[\delta(z+z_0) + \delta(z-z_0)] \xrightarrow{FT} \cos(kz_0) \tag{1.39}$$

$$x(z) \otimes y(z) \xrightarrow{FT} X(k)Y(k) \tag{1.40}$$

It is possible to calculate the inverse Fourier transform of Equation 1.36, obtaining[22]:

$$i_D(z) = \frac{\rho}{8} T_{ref} T_{samp} \left[\left(\gamma(z) \sum_{j=1}^{N} R_{s_j} + 1 \right) \right. \qquad \textbf{DC Component}$$

$$+ 2 \left(\gamma(z) \otimes \sum_{j=1}^{N} \sqrt{R_{s_j}} \left(\delta(z \pm 2(z_{ref} - z_{s_j})) \right) \right) \qquad \textbf{Cross-interference}$$

$$\left. + 2 \left(\gamma(z) \otimes \sum_{j \neq i=1}^{N} \sqrt{R_{s_j} R_{s_i}} \left(\delta(z \pm 2(z_{s_j} - z_{s_i})) \right) \right) \right] \qquad \textbf{Self-interference}$$

$$\tag{1.41}$$

Similarly to the original Equation 1.36, the desired reflectivity profile $\sqrt{R_s(z_s)} = \sum_{j=1}^{N} \delta(z_s - z_{s_j})$ (as exposed in Equation 1.32) is embedded in the cross-interference term. By calculating the result of the convolutions, we get to the result of the interferometric measurement [22]:

$$
\begin{aligned}
i_D(z) = \frac{\rho}{8} T_{ref} T_{samp} & \left[\left(\gamma(z) \sum_{j=1}^{N} R_{s_j} + 1 \right) \right. && \textbf{DC Component} \\
& + 2 \sum_{j=1}^{N} \sqrt{R_{s_j}} \Big(2\gamma(z_{ref} - z_{s_j}) - 2\gamma(z_{ref} - z_{s_j}) \Big) && \textbf{Cross-interference} \\
& \left. + \sum_{j \neq i=1}^{N} \sqrt{R_{s_j} R_{s_i}} \Big(2\gamma(z_{s_j} - z_{s_i}) - 2\gamma(z_{s_j} - z_{s_i}) \Big) \right] && \textbf{Self-interference}
\end{aligned}
$$

$$(1.42)$$

Besides the sample's reflectivity profile, Equation 1.42 also carries information that will produce imaging artifacts, but this discussion will be left to a further section (1.5 - Imaging Artifacts). The practical results of this equation considering discrete sample reflectors and a Gaussian-shaped source spectrum are plotted in Figure 1.28.
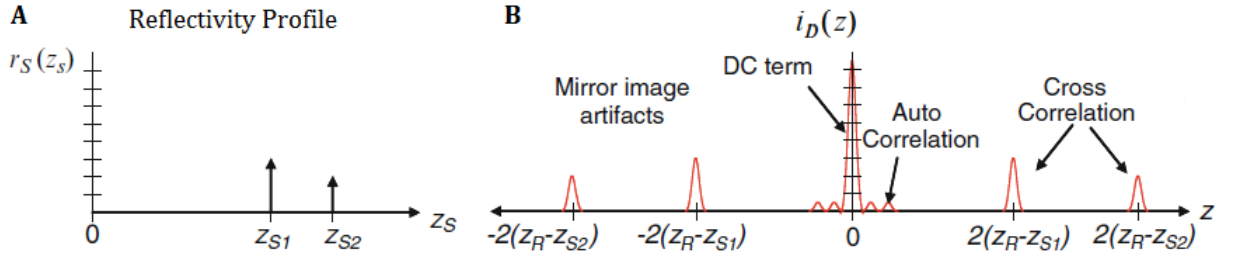
Figure 1.28: (A) Reflectivity profile $r_s(z_s)$ of an arbitrary sample, with two layers at z_{s_1} and z_{s_2}. (B) Simulation of the obtained reflectivity profile [22]. (Adapted).

As can be seen, due to the properties of the inverse Fourier transform on a real signal as the spectral interferogram, we get a symmetric result. This conjugate image horizontally inversed at the $z = 0$ position constitutes an imaging artifact that will be latter explained, along with others visible in Figure 1.28 (DC term and coherence noise derived from the auto correlation component).

The axial measurement range z_{max} depends on the detector's number of pixels M and the source's coherence length l_c and is given by [11] [25]:

$$z_{max} = \frac{M \ l_c}{2} = M \ \delta z \tag{1.43}$$

Due to the round trip propagation of the sample and reference beams, $l_c/2 = \delta z$ is recognized as the axial resolution (image resolution in the direction of the incident light), representing the pixel spacing. Considering that the detectors has M pixels linearly spaced in k with a sampling interval of δk, the wavenumber range collected is $\Delta k = M \delta k$. This sets the sampling interval in the z-domain as $\delta z = \frac{\pi}{2\Delta k}$. Attending to these considerations we can rewrite Equation 1.43 as [25]:

$$z_{max} = \frac{M \ \pi}{2\Delta k} = \frac{\pi}{2 \ \delta k} \tag{1.44}$$

Swept Source

An alternative to the Spectral Domain OCT, where all of the components of $I_D(k)$ are detected simultaneously using a spectrometer, is capturing these components sequentially in a single detector while synchronously varying and recording the wavenumber of a narrow band swept-laser source. That is the working principle of Swept Source OCT (SS-OCT) and its basic setup is illustrated in Figure 1.29.
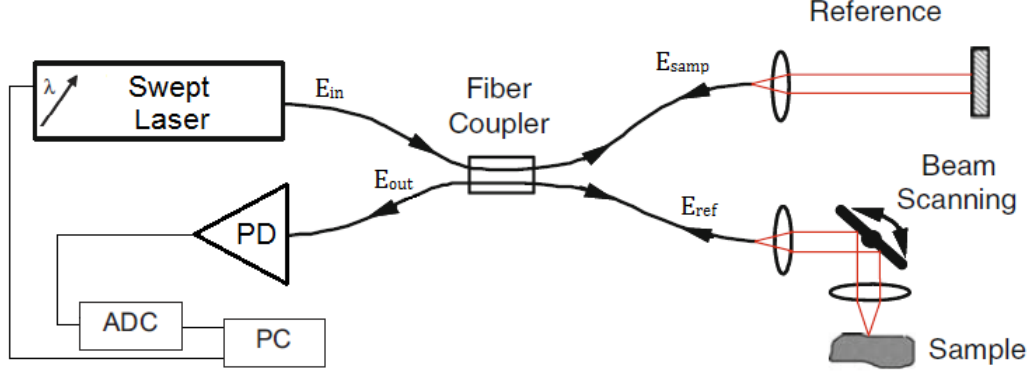
Figure 1.29: Basic setup of a SS-OCT system.

Because of the requirement of synchronization between the acquired signal and the wavenumber to which that data corresponds to, there is the need to also acquire the source's wavenumber, thus the link between the laser source and the PC portrayed in Figure 1.29.

Although the signal is detected in a different way, the mathematical formalism that describes it is the same as in the SD-OCT, so an inverse Fourier transform must also be applied, obtaining a result similar to Equation 1.42 and as represented in Figure 1.28. The axial measurement range z_{max} in this modality is also given by Equation 1.44, if we consider this time M evenly spaced wavenumbers, instead of the number of the detector's pixels, in such way that $\Delta k = M\delta k$ is still verified[22][25].

The cross-interference term for a single reflector has a frequency proportional to the wavenumber sweep resolution δk, the sweep frequency f_{sweep} and the maximum path lenght difference between the sample and reference arms which corresponds to the maximum axial measurement depth z_{max}. Thus, the maximum detectable frequency of the interference signal is given by[26]:

$$f_{max} = \delta k \ f_{sweep} \ \frac{z_{max}}{\pi} \tag{1.45}$$

With the swept wavenumber resolution δk being given by[26]:

$$\delta k = 2\pi \left(\frac{1}{\lambda_0 - \frac{\Delta\lambda}{2}} - \frac{1}{\lambda_0 + \frac{\Delta\lambda}{2}} \right) = 2\pi \ \frac{\Delta\lambda}{\lambda_0^2 - \frac{\Delta\lambda^2}{4}} \tag{1.46}$$

This parameter is important to select an appropriate detector, capable of matching the source's and the optical setup requirements. If the selected detector's bandwidth is inferior to the maximum detectable frequency of the interference signal f_{max}, a restriction on the axial measurement range z_{max} will occur[26] .

1.4.3 Overall Comparison

Now that both time domain and Fourier domain OCT main features were exposed, we are in conditions of making a comparison between these modalities, as well as between spectral and swept source in the Fourier domain.

Several important parameters of an OCT system are equal in both cases. Namely the axial resolution, which is theoretically the same for FD-OCT and TD-OCT, since it is determined by the light source. Also, most noise sources such as $1/f$ noise, dark current noise, Johnson noise and preamplifier noise do not alter for each case, as does not the DC component of the signal[11]. However, other important aspects of OCT imaging determine that one modality can now be considered superior in many aspects to the other.

In fact, most research in OCT is currently performed using FD-OCT systems, which have now clearly surpassed TD-OCT. The main reasons for this are the two most clear and attractive advantages of FD-OCT over TD-OCT: the superior imaging speed and the higher sensitivity[27].

The fact of no moving parts are required in FD-OCT is a big advantage because it prevents compromising the image quality with the acquisition speed. The moving mirror also limits the acquisition speed, making the system impractical to perform *in vivo* OCT imaging, where high acquisition speed is an essential condition in order to allow the visualization of the sample in real time. Therefore this requirement of TD-OCT compromises most clinical potentialities, which is the biggest market for OCT systems. When compared to FD-OCT, the potential imaging speed of the last one can be up to 1000 times faster[21][25].

To compare the sensibility between both functioning modalities, we can rely on the analysis of the Signal-to-Noise Ratio (SNR) for each case. Since the important parameter to make the comparison is the final result, we are not going through an exhaustive mathematical treatment (which can however be consulted in literature[22][25]). It has been proved that the relation between the SNR in time domain and in Fourier domain (both spectral and swept source) is given by:

$$SNR_{\text{FD}} = SNR_{\text{TD}} + 10\log\left(\frac{M}{2}\right) \tag{1.47}$$

Which proves that a FD-OCT system is more sensitive than a TD-OCT by a factor of $M/2$, where M accounts for the number of pixels in the detector in SD-OCT or the equivalent number of evenly spaced wavenumbers in SS-OCT. This improvement in sensibility means that with FD-OCT it is possible to detect weaker reflections from scattering layers of the sample, acquiring data that could be invisible to a TD-OCT. To obtain the same SNR in time domain, it would be necessary to decrease the source's bandwidth which leading to a greater coherence length and ultimately compromising the axial resolution.

Naturally, FD-OCT systems also show some drawbacks. One of them is the fact that this modality is more sensitive to motion artifacts. That is partially because, contrarily to TD-OCT in which only a fraction of the sample's volume is measured at a time, in Fourier domain all the waves reflected by the sample's layers display interference simultaneously during the exposure time. This causes FD-OCT to be more sensitive to vibrations or moving scatterers[24]. Another disadvantage of FD-OCT, namely in spectral domain, is the considerable technical effort needed for the high resolution spectrometer for larger wavelengths ($> \sim 1300\ nm$), that

are not easily detected by Silicon technology[24]. The sensitivity roll-off with the imaging depth increase is another drawback that only happens in FD-OCT[27]. This optical parameter can be considered an imaging artifact and will be explained on the next section. In fact, the main disadvantages of FD-OCT are related with undesirable imaging artifacts that do not exist in TD-OCT, such as coherence noise and complex conjugated image. These will also be exposed in the next section (1.5 - Imaging Artifacts).

As for the comparison between the two possible implementations of FD-OCT, some considerations can also be taken. Because SS-OCT uses a single photodetector, it has the advantage of being able to simply eliminate the unwanted DC component by high-pass filtering the photodetector output signal[24]. In SS-OCT it is also possible to strongly attenuate the DC component by using a balanced detector with a High Common Mode Rejection Ration (CMRR), assessing however the same information about the depth profile of the sample as the SD-OCT[26]. In SD-OCT, data collected by the detector array is sampled in evenly spaced wavelength intervals $\Delta\lambda$. However, because of the non-linear relation between k and λ (Equation 1.21), the Fourier transform (which links the z and k space) of data acquired directly from the spectrometer is improper for applying the inverse Fourier transform. Therefore, because the signal is unevenly sampled in the k space but evenly sampled in the λ space, data preprocessing is needed, which is typically done with a non-linear scaling algorithm. This results in the broadening of the Point Spread Function (PSF) - the impulse response of a focused optical system, causing an imaging artifact that will be exposed in the next section[11]. It also represents an extra step in data processing to which a greater computation effort and time is associated. SS-OCT systems can complement the laser output with a clock signal which is linear in the k space rather than in the λ space to simply overcome this issue. On the other hand, the implementation of a SS-OCT system involves a relatively complex synchronization system, in order to make the correspondence between each interference spectrum acquired to the wavenumber interval Δk swept. Besides generating the laser output, swept sources also generate a Sweep Trigger to create a gating pulse in which the interference spectrum will be contained, and a clock signal to assist the synchronization in the digitalization of the signal. This need for synchronization also makes software development in SS-OCT a more complicated task. Finally, when we compare commercial OCT systems available, it is generally true to say that SS-OCT systems are capable of acquiring data at greater acquisition rates.

The most appropriate way to make a quantitative comparison between Fourier domain and swept source OCT systems is to compare the most relevant specifications of some popular commercially available systems of both types. This comparison is exposed in Table 1.2.

Briefly and generally speaking, it would not be legitimate to indisputably declare that one of these Fourier domain modalities is superior to the other, and the specific goals of the system in which OCT imaging is being applied plays a determinant role in the choice between them. However, it is generally true to say that, currently, the fastest high-quality OCT imaging can be done with SS-OCT.

We can conclude from the above considerations that FD-OCT allows systems to acquire images at a higher speed and resolution, reasons why SD-OCT and SS-OCT are nowadays, the most popular modalities in OCT imaging. An overall imaging comparison between time and Fourier domain can be made by analyzing Figure 1.30 and its acquisition parameters, present in the corresponding caption. However,

OCT System	Axial Resolution δz	Lateral Resolution δx	Imaging Depth z_{max}	Imaging Speed
Phoenix OCT (SD-OCT)	3 μm	1.8 μm	1.4 μm	13 000 A-Scans/s
Spectralis OCT (SD-OCT)	3.9 μm	14 μm	1.9 μm	40 000 A-Scans/s
Cirrus OCT (SD-OCT)	5 μm	15 μm	2 μm	68 000 A-Scans/s
DRI OCT Triton (SS-OCT)	2.6 μm	20 μm	3.3 μm	100 000 A-Scans/s
IVS-1000-100 (SS-OCT)	8 μm	6 μm	2.5 μm	100 000 A-Scans/s

Table 1.2: Comparison between the most relevant imaging specifications of some of the most popular commercially available OCT systems.
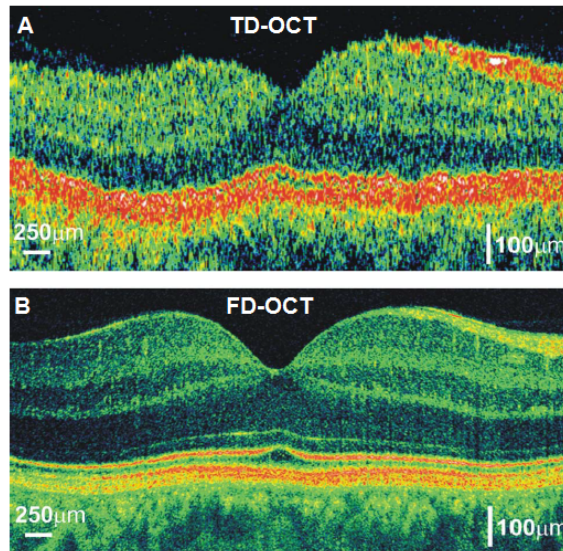
Figure 1.30: Comparison of a cross-sectional image *in vivo* of an human eye using a TD-OCT and a FD-OCT. (A) Detection in time domain using the commercial device OCT Stratus (Zeiss) with axial axial resolution 10 μm and acquisition speed 400 A-Scans/s. (B) Detection in Fourier domain, using a laboratory system of the Institute of Physics, Niculaus Copernicus University, Torun, Poland with axial resolution 2 μm and acquisition speed 30 000 A-Scans/s [15].

with these techniques arose new imaging artifacts that can deteriorate the acquired information and for this motive it is important to develop techniques to make up for this disadvantage. An insight into these imaging artifacts and how to overcome them is precisely the discussion theme of next section.

1.5   Imaging Artifacts

As previously said, besides the desirable information on the depth profile of the sample, Equation 1.42 also carries information that will produce intrinsic imaging artifacts. Some of them are easily removed or compensated by proper interpretation of data. Others, however, can inevitably contaminate useful information of acquired images. It is, thus, important to identify and understand the origin of these artifacts and methods to overcome them. An overview of the most significant ones in FD-OCT

will now follow.

1.5.1   Sample Layers Displacement

To begin with, the factor of 2 preceding the summation in Equation 1.42 (which can be understood from the fact that the interferometer measures the round-trip distance to each reflector) results in a displacement of each sample layer from the reference position, doubling it. This can be simply compensated by relabeling axial distances, accounting for this factor of 2[22].

1.5.2   Broadened Peaks

Another artifact is the fact that each reflector appears broadened out to a width of about a coherence length by convolution with the function $\gamma(z)$. As previously said, this is the definition of a Point Spread Function (PSF). Given the inverse relationship between the coherence length l_c and the light source bandwidth Δk (Equation 1.1), by using a source with a bandwidth as broad as possible, the Full Width at Half Maximum (FWHM) of each peak, corresponding to each layer of the sample, can be narrowed[22].

1.5.3   Sensitivity Roll-Off

Sensitivity roll-off is another exclusive imaging artifact of FD-OCT. However its origin is different for each Fourier domain modality treated. Whereas in SD-OCT it is caused by the limited spectral resolving power of the detector array, in SS-OCT its origin is the finite linewidth $\delta\lambda$ of swept laser source[15], according to the previously discussed relation[25]:

$$\delta\lambda = \frac{\Delta\lambda}{M} \tag{1.48}$$

The consequence of this effect is an attenuation of the system's sensitivity over the axial measurement range, as represented in Figure 1.31. This parameter can be measured in an OCT system by calculating the peak of its PSF (interference spectrum obtained when using a mirror as sample) for a sequence of successive reference mirror positions.

This sensitivity decay is one of the imaging artifacts present in Figure 1.33.

1.5.4   DC Component

The DC component identified in Equation 1.42 gives rise to a large artifactual signal centered at position $z = 0$ (as represented in Figure 1.28), with a FWHM of one coherence length[22]:
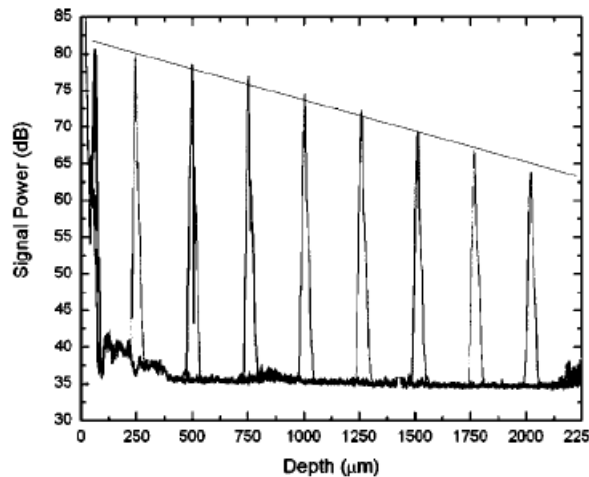
Figure 1.31: Illustration of the sensitivity roll-off parameter[26]. (Adapted).

$$\text{FWHM}_{\text{DC}} = l_c \tag{1.49}$$

Despite this FWHM value not appearing very wide, it is much larger than the cross-correlation terms and can overwhelm the desired signal components in the proximities of $z = 0$. The largest component of the DC artifact comes from the high reflectivity of the reference mirror ($r_{ref} \approx 1$). Thus, a simple method to eliminate this artifact is to record a spectral interferometric signal with only the reference mirror present, not placing any sample in the sample arm, and subtract this acquired signal to the subsequent spectral interferometric signals[22]. This artifact can also be significantly attenuated in SS-OCT by using a balanced detector with a high CMRR. A visual interpretation of this artifact is also present in Figure 1.33.

1.5.5 Coherence Noise

The auto-correlation terms in Equation 1.42 give rise to an undesirable signal component commonly designated as coherence noise. There are two possible origins for this imaging artifact: either from reflections within the optical apparatus of the OCT system that also contribute to the total signal collected, or from reflection within the reflective layers of the sample that also cause interference[15]. The first one, which is not correlated with the sample, can be simply eliminated by signal subtraction similarly to the elimination of the DC component, registering the interference spectrum when no sample is present in the sampling arm. However, it is more difficult to get rid of coherence noise related to the sample's internal reflections. Because the distances between reflectors within a sample are typically much smaller than the path length distance between any sample reflector to the reference arm, this artificial components appear closer to the $z = 0$ position[22]. Nonetheless, it can be mixed with relevant cross correlation terms, either in-between scattering layers of the sample or coinciding with them and therefore contaminating the image. The best method to attenuate it is to ensure a very high reference reflectivity, so that the amplitude of the auto-correlation component is very small when compared to that of the cross-correlation[22]. In the case of thin objects (at least twice as thin as the total measurement range), there is also the possibility of separating this component of the

coherence noise from the sample's depth profile information via a proper selection of the optical path difference between the reference mirror and the first surface of the examined sample[15], avoiding any layer of it being close to the smaller path length z values where this component of the coherence noise takes place.

This imaging artifact is also visible in Figure 1.33.

1.5.6   Complex Conjugate

Since the detected interferometric spectrum is necessarily a real signal, its inverse Fourier transform must be an Hermitian function. In other words, because the positive and negatives z values are complex conjugates of each other and they are real, the complex conjugate is equal to the original function. Therefore, when recreating the structure of the sample from one spectral interference signal, two symmetrical images are obtained, with its symmetry point in $z = 0$[15] [22].

We can identify in Equation 1.42 the negative terms in the cross-interference and the self-interference components as the responsible for this effect: term $-(z_{ref} - z_{s_j})$ in the cross-interference component and term $-(z_{s_j} - z_{s_i})$ in the self-interference component[26].

This artifact does not contaminate the relevant information on the sample's depth profile as long as the sample is kept entirely to either the positive or the negative side of the path length z. However, if a sample's surface is positioned over the $z = 0$ border, the reconstruction of the sample through imaging will be situated both in the positive and in the negative values. In this case, symmetric images will be superimposed, which prevents a reliable analysis of the sample's structure. This overlapping mirror image issue cannot be removed by image processing alone[15] [22].

The image contamination caused by this effect is exposed in Figure 1.32, where the depth profile of the same sample is reconstructed via FD-OCT with and without the complex conjugate artifact.
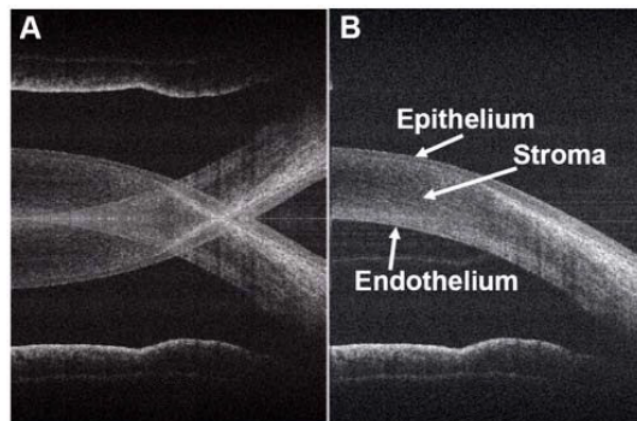
Figure 1.32: (A) FD-OCT image of human cornea and iris contaminated with the complex conjugate artifact. (B) The same image with the artifact resolved[21].

Having now addressed the most relevant imaging artifacts associated with a FD-OCT system, their combined presence in an interference spectrum is visually represented in Figure 1.33.
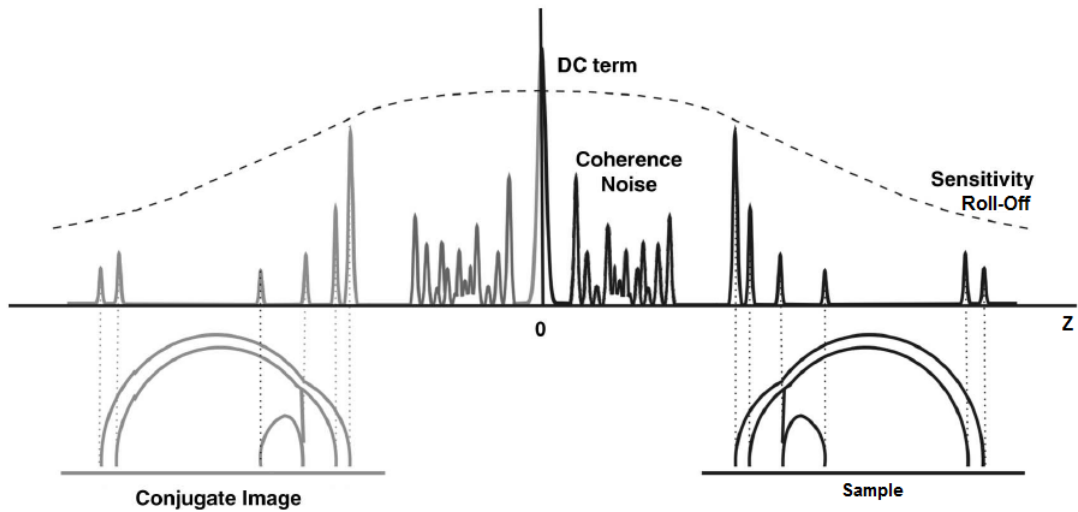
Figure 1.33: Imaging artifacts in a spectral interferogram using FD-OCT. Beyond the desired information of the sample it is also present the DC component of the signal, coherence noise terms and the complex conjugate of the data. Additionally, the signal is affected by the sensitivity roll-off artifact[15] (Adapted).

1.6   Scanning Modalities

Being an imaging technique, the ultimate purpose of an OCT system is to give visual information on the depth profile of a sample, as it has been highlighted throughout this work. Any analyzed sample will necessarily have 3 physical dimensions. However, the information collected by the OCT system may be restrained to 1 or 2 dimensions, as well as include the whole 3 dimensions of it. The determination of the extension of the sample's analyzed dimensions is made by the beam scanning mechanism of the OCT.

As previously shown in Figure 1.24, the basic setup of an OCT system must include a scanning apparatus which allows focusing the light beam on different locations of the sample. If no scanning exists, only one point of the sample will be focused and consequently only a 1 dimensional depth profile will be acquired. However, if the beam focus is swept across the sample, either vertically or horizontally, it is possible to associate a depth profile to each different position of the incident beam and therefore make a 2 dimensional correspondence. If both vertical and horizontal sweeping motion of the light beam across the sample are present in a synchronized way, the whole 3 dimensions of the sample can be analyzed and a 3 dimensional acquisition is achieved.

This sweeping motion of the light beam across the sample is usually assured by a scanning galvo mirror system. The data acquisition process must be in complete synchrony with the scanning system, and the assurance of this synchronization is often a complex process when developing an OCT system.

This section will be dedicated the correspondence between the type of scanning motion acting on a sample and the nomenclature of the acquired image. Labeling data acquisitions with this technical language is vital to easily identify and communicate the type of scanning motion associated with a certain acquired image.

1.6.1   A-Scan

An A-Scan is simply the depth profile of one point of the sample, i.e. a single interference spectrum. In TD-OCT there is the need to apply a scanning motion, not in the sample arm but on the reference arm, varying the reference mirror position to scan successive depth positions of the sample. However, since in FD-OCT the reference mirror is fixed, there is no need for any scanning motion at all. The equivalent result of this scanning is made either by the individualized acquisition of the spectral components in SD-OCT or by the laser frequency sweeping in SS-OCT

1.6.2   B-Scan

By collecting adjacent A-scans in successive positions along a vertical or horizontal line across the sample, a cross-section image is obtained, termed as a B-Scan. Most commonly, the B-Scan image corresponds to longitudinal section of the sample, obtained by acquisition of multiple pixels along a transversal (x-axis) coordinate (Figure 1.34) which is slowly scanned, while the scanning in the direction of the optical axis is faster (either by the reference mirror motion in TD-OCT, by the individualized acquisition of the spectral components in SD-OCT or by the laser frequency sweeping in SS-OCT).
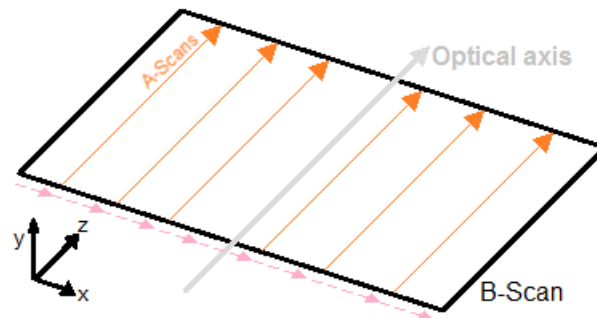
Figure 1.34: Scanning mechanism associated with a B-Scan image acquisition. The scanning is faster axially (z-axis) and slower laterally (x-axis), as represented by the orange and pink arrows, respectively.

The axial and transversal scanning motion should be synchronized and never simultaneous. In order to be able to associate each A-Scan to the depth profile of a single point in the sample's surface, for each axial scanning the transversal scanning mechanism must be stopped. It should only move to the next position after the A-Scan of the focused point is acquired.

A B-Scan image can then be perceived as multiple A-Scans displayed side by side, as represented in Figure 1.35.
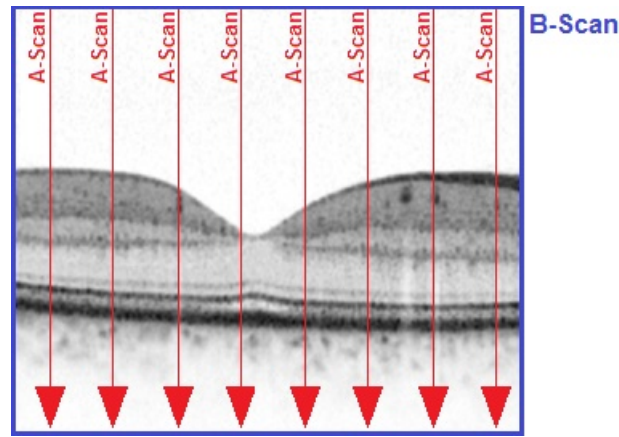
Figure 1.35: Overview of the relation between A-Scans and a B-Scan. Obviously, every vertical pixel line present in the image is an A-Scan, but for a clearer representation only a few were characterized by the red arrow.

1.6.3   T-Scan

A T-Scan can be compared to the A-Scan, but instead of giving information on the axial direction, it gives information on the transverse one[26]. Therefore, a T-Scan also gives rise to a 1 dimensional piece of information, but this time collected by varying the beam focus transversally, while maintaining the axial coordinate fixed. In TD-OCT this is done by scanning the sample transversally with the scanning mechanism while the reference mirror is at rest in a fixed position[28].

Fourier domain OCT systems, however, can only output A-Scans and not T-Scans, as the axial scanning cannot be restrained. Therefore, the only way to visualize a T-Scan in FD-OCT is through data manipulation of a collection of A-Scans in a B-Scan.

1.6.4   C-Scan (or en-face image)

The same way the T-Scan was compared to the A-Scan, a C-Scan can be compared to a B-Scan. We can say that the A-Scan is for the B-Scan as the T-Scan is for the C-Scan, which can be perceived when comparing Figures 1.34 and 1.36.

In TD-OCT, a C-Scan is acquired by collecting T-Scans for adjacent values of the orthogonal lateral coordinate. Considering T-Scans oriented along the x coordinate, the process would be to repeat this acquisitions along the y coordinate[28].

Since FD-OCT systems cannot output T-Scans, they naturally cannot directly output C-Scans either. Nonetheless, C-Scans can be obtained in this modality via data manipulation after a whole volume of the sample is acquired. To do so, a series of B-scans are firstly acquired for different transverse coordinates. After this, the acquired 3 dimensional volume is sectioned to slice a C-Scan[28]. Therefore, unlike a TD-OCT system, a FD-OCT cannot produce a C-scan image in real time.
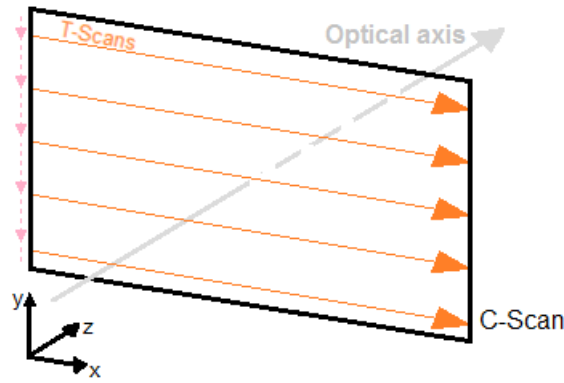
Figure 1.36: Scanning mechanism associated with a C-Scan image acquisition. The scanning is faster laterally (x-axis) and slower transversally (y-axis), as represented by the orange and pink arrows, respectively.

1.6.5   Volume

A volume consists of a collection of B-Scans, acquired along successive planes of the y axis, considering that the A-Scans are acquired as was portrait in Figure 1.34. Therefore, besides the scanning along the optical axis, the sample is scanned in two transversal dimensions, allowing a 3 dimensional acquisition of the sample. For this, the scanning motion along the x and y axis must be synchronized: only after the x mirror scans a whole horizontal line, corresponding to a B-Scan, should a new y position in the sample be focused by moving the y mirror. This synchronization is visually explained in Figure 1.37.
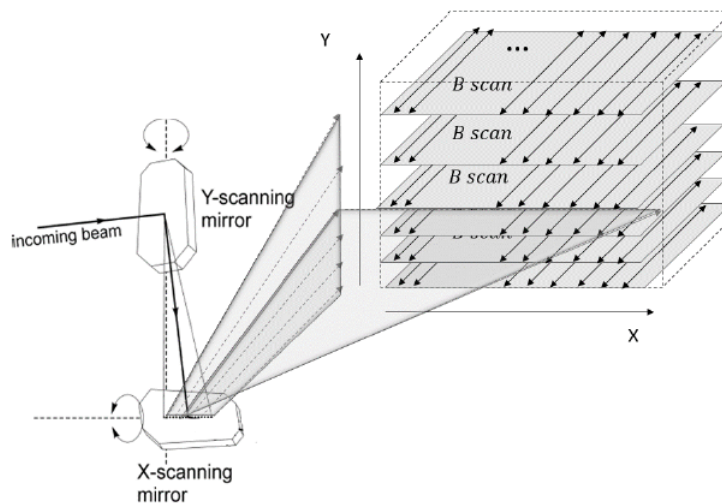
Figure 1.37: The acquisition of a volume is enabled by two scanning mirrors. By moving the x-scannin mirror a B-Scan can be acquired. By synchronously adding the y-scanning mirror movement the acquisition of multiple B-Scans is enabled, obtaining a volume[26].

1.6.6   Projection

A projection is a useful representation of certain volume acquisitions, allowing the reconstruction of the surface of the sample.

Neither in TD-OCT nor FD-OCT is possible to directly acquire a projection, being only achievable through means of data manipulation. For this, it is necessary to firstly acquire an entire volume of the sample and after that calculate each point of the projection image $P_{b,a}$ according on the formula:

$$P_{b,a} = \sum_{i=1}^{M} D_{b,a,i} \tag{1.50}$$

in which $b = 1, 2, ..., N_B$ and $a = 1, 2, ..., N_A$, considering N_B B-Scans in the volume and N_A A-Scans in each B-Scan. $D_{b,a,i}$ corresponds to the data value i of the M data values acquired in the A-Scan a, of the B-Scan b. Therefore, each point in a projection image corresponds to the sum of the acquired data throughout an A-Scan. This concept may become clearer with a graphical explanation, as shown in Figure 1.38.
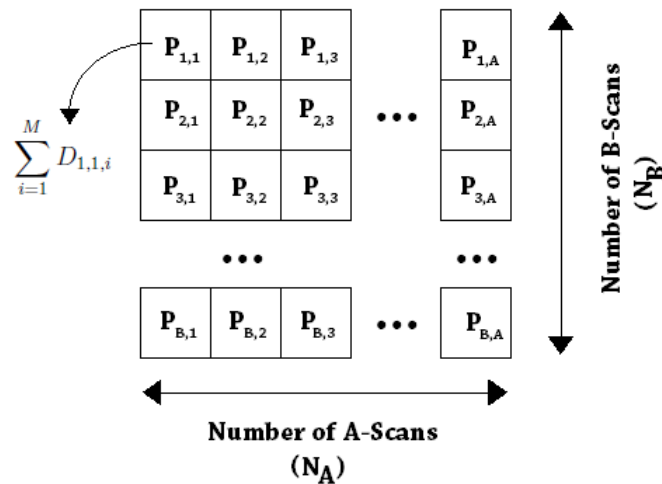
Figure 1.38: Representative scheme on how to obtain a projection image from a volume acquisition with N_B B-Scans, each containing N_A A-Scans with M data points D.

The result of this operation is a two dimensional image with a height proportional to the number of B-Scans of the volume and a width proportional to the number of A-Scans in each B-Scan. Therefore, its horizontal resolution increases with the number of A-Scans and its vertical resolution increases with the number of B-Scans.

The information contained in this image is the projection of the sample along the depth scanned axis (z), resembling the surface of the sample seen from the front.

Figure 1.39 is a good support to understand how a B-Scan, a volume and its projection are related.
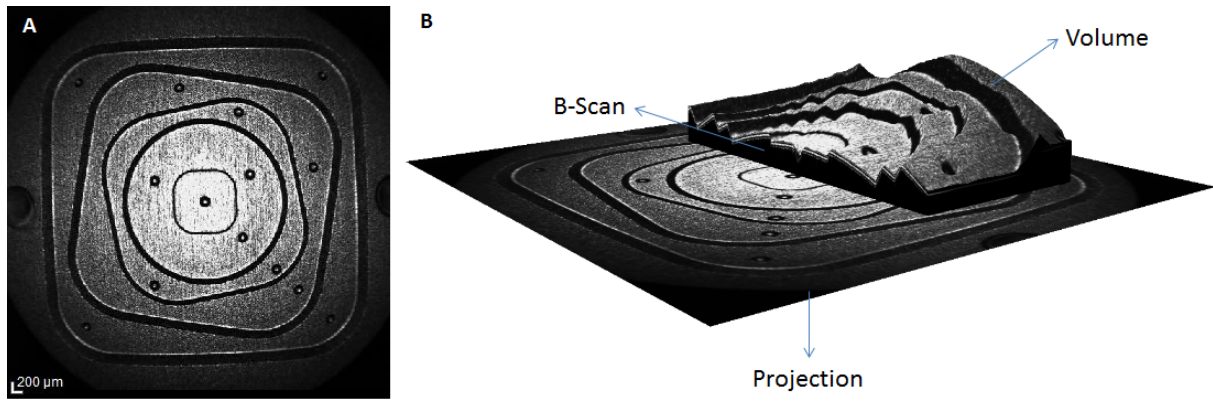
Figure 1.39: (A) Image of a target with reliefs that differ in height. (B) Results of an OCT test applied to the same target using an OCT system from Heidelberg Engineering.

2 | *IBILI's SS-OCT System*

Now that the basic concepts and nomenclature associated with an OCT system have been explained, it is time to present the specific system on which the development work was performed.

To do so, an overview of the components and signals present in the system will be presented throughout this chapter, as well as how these components and signals relate to each other, from the instant the light leaves the source to the instant the depth profile of the sample is displayed to the user. The description of the optical components currently used in the experimental setup have already been described in several works[26][27][29][30], and no significant modifications have occurred since these. For this reason and because the aim of this thesis is to focus on the data acquisition system, only the components that are directly related to it will be presented in detail, sparing the repetition of a thorough description of some optical components, namely the optical fibers, couplers, polarization controllers, collimators and objective lenses.

The function of the mentioned optical components will, however, be addressed in the overall description of the system, which will be the discussion theme of the first section of this chapter. The following sections will be dedicated to the description of the specifications and characteristics of each component in the setup.

2.1 Setup Scheme and Overall Description

This section will briefly describe the functioning of the developed SS-OCT system at IBILI.

To easily and chronologically follow each relevant signal in the OCT as it travels along the different components of the system, we will start by showing its setup scheme in Figure 2.1.
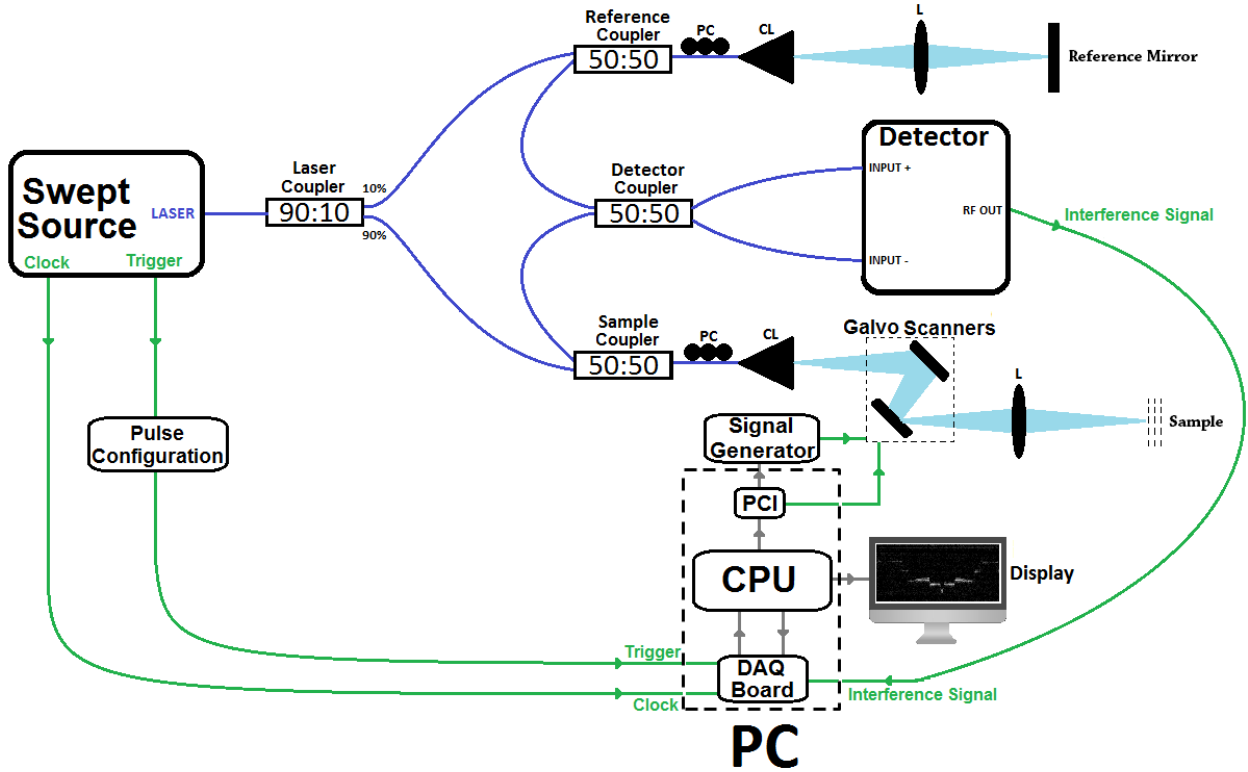
Figure 2.1: Scheme of the SS-OCT setup developed at IBILI. Blue lines represent optical fiber paths and light blue lines represent light traveling in air. Green arrows represent electronic signals paths and gray arrows represent data transfers between components of the data acquisition system. The letters identifying some of the optical components stand for: PC - Polarization Controller; CL - Collimator; L - Objective Lens.

As shown in this scheme, the swept source outputs 3 signals: the Laser Output, the Sweep Trigger and the Clock. We will begin by following the laser path.

As it leaves the light source traveling in optical fiber, the laser is forwarded to a 90:10 coupler, where 90% of the optical power heads to the sample arm and the remaining 10% to the reference arm. In both arms there is a fiber polarization controller which is manually adjusted to match the polarization between light from the sample and from the reference arms. This is done by physically tightening the optical fiber and it is an important process as it assures that the interference occurs in optimal conditions, improving the sensitivity of the system. After that, and for both arms, light reaches a collimator that narrows and directs the beam with minimal dispersion. When leaving the collimator, light from the reference arm passes through an objective lens which focuses the beam in a highly reflective ($\approx 95\%$ reflectivity) gold coated mirror. As for the light in the sample arm, it is directed into a dual axis galvanometer system which directs the beam to an objective lens to be focused in the sample. The reflected beam from either the reference mirror or the reflective layers of the sample make the same path backwards along the optical

fiber, being this time, however, deflected in the reference or the sample coupler, accordingly. This directs each beam into an input of the detector coupler, which is where the beams come together and the interference occurs. Both outputs of the coupler are then directed into the inputs of a balanced detector, concluding the optical process of data generation, culminating in an A-Scan. From this stage on, electrical signals are in charge of controlling the acquisition of this A-Scan. These signals are the output of the balanced detector containing the desired information, along with a trigger and clock signal generated by the swept laser source responsible for synchronizing the acquisition process, as it will be explained ahead. These are also the inputs of the DAQ board, in charge of converting the detector's analogical electric signal into digitized data to be processed and displayed to the user.

In this brief description the main components of an OCT system, related to both optics and data acquisition were mentioned. Others were left out such as the ones responsible for controlling the galvo mirrors (the PCI and the Signal Generator) and the digital delay. However, every single component represented in the scheme of Figure 2.1 is essential to the proper functioning of the system, as we will see throughout this chapter. Before attending to the singular description of each component, a picture of the OCT system in focus is presented in Figure 2.2, to give body to the schematic representation.
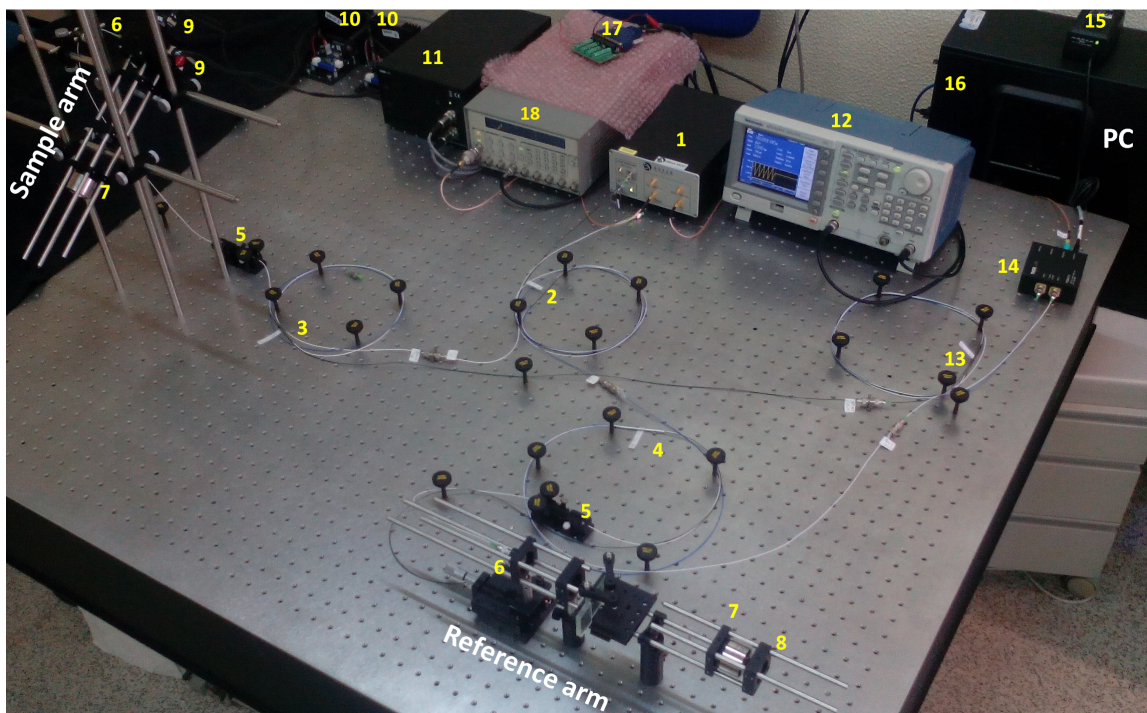
Figure 2.2: Picture of the SS-OCT setup developed at IBILI. Legend: 1 - Swept Source; 2 - Laser Coupler; 3 - Sample Coupler; 4 - Reference Coupler; 5 - Polarization Controllers; 6 - Collimators; 7 - Objective Lenses; 8 - Reference Mirror; 9 - Galvanometer Mirrors; 10 - Galvanometer Servo Drivers; 11 - Galvanometer Power Supply; 12 - Signal Generator; 13 - Detector Coupler; 14 - Detector; 15 - Detector Power Supply; 16 - DAQ Board; 17 - PCI; 18 - Pulse Configuration.

2.2　　　Swept Laser Source

The light source is the central component of an OCT system, since it is the responsible for imposing the limits of different imaging parameters such as the maximum depth and the axial resolution. In an SS-OCT its importance is even greater, as it typically also controls the A-Scan generation rate and the synchronization between the laser output and its digitalization along the swept wavelengths by generating a trigger and a clock signal.

The swept laser source used in this setup is the Axsun OCT Swept Source Engine Model SSOCT-1060 (Figure 2.3), developed specifically for SS-OCT imaging applications.

Figure 2.3: Axsun OCT Swept Source Engine Model SSOCT-1060[31].

2.2.1　Specifications and Operation Principles

The most relevant specifications of this light source are presented in Table 2.1.

Parameter	Value
Tunning Wavelength Range	985.0 - 1095.0 nm
Center Wavelength	1060 nm
Sweep Frequency	100 kHz
Average Output Power	Min 15 mW
Coherence Length	Min 10 mm (typical 12 mm)
Scan Range in Air	3.7 mm
Maximum Samples	1510
Selected Number of Samples	1376
Duty Cycle	45%
Estimated Clock Frequency	310 MHz ($\pm$ 20% variation)

Table 2.1: Typical scan parameters for the SSOCT-1060 Engine[31].

Firstly, it is important to point out that this laser has a safety class 3B, which means that it is hazardous if the eye is exposed directly, but diffuse reflections such

as from paper or other matte surfaces are not harmful[31]. Therefore, the laser should be carefully handled, to avoid direct exposure from the eye to the beam.

The sweep technology of this laser consists of a Semiconductor Optical Amplifier (SOA) and high finesse fiber Fabry-Perot tunable filter (FPF-TF) with a short cavity length to enable rapid tuning[26][27].

The specified center wavelength of 1060 nm was chosen for imaging the retina of small animals. This is a popular wavelength in several applications due to the fundamental wavelength emission of the Nd:YAG laser at 1064 nm, which makes a lot of optical components in the market optimized for working near this spectral region. There is a minimum of the absorption coefficient in watter in this range (as previously shown in Figure 1.21), which is an important aspect since water absorption plays a considerable role in this application. While a greater center wavelength would cause more undesirable water absorption, a smaller one would be more susceptible to scattering. Anyhow, for retinal imaging, it is preferable for the spectrum to be shifted slightly down in wavelength, to keep away from the increase in water absorption which starts to become significant at longer wavelengths.

The spectral power output has a tunning range of $1095.0 - 985.0 = 110$ nm, and its average values along this range are plotted in Figure 2.4.
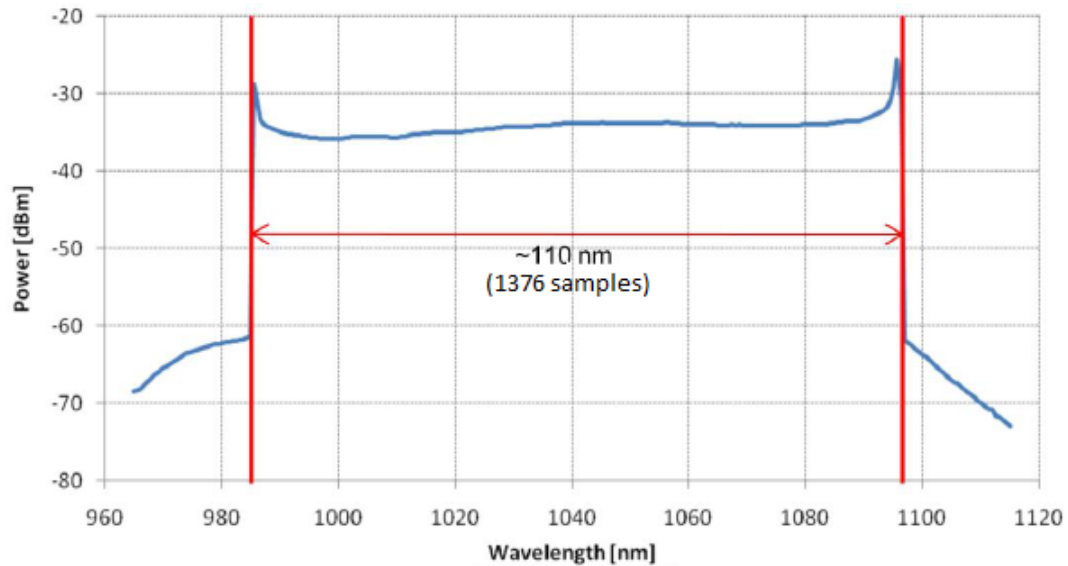
Figure 2.4: Time Averaged Power Output of a Typical SSOCT-1060 Engine[31].

Note that although the middle wavelength of this tunning bandwidth is actually $\frac{1095-985}{2} = 1040$ nm, the optical parameter denominated center wavelength is a power-weighted mean wavelength, given by:

$$\lambda_0 = \frac{1}{P_{total}} \int p(\lambda)\lambda d\lambda \qquad (2.1)$$

With the total power:

$$P_{total} = \int p(\lambda)d\lambda \qquad (2.2)$$

So, as presented in Table 2.1, for this light source the manufacturer specifies the center wavelength at $\lambda_0 = 1060$ nm.

Another important specification is the sweep frequency, which reflects how long it takes for the laser to sweep the whole wavelength range, and therefore defines the A-Scan generation rate. Since the sweep frequency has a value of 100 kHz,

this means that the laser source is capable of generating 100 000 A-Scans/s, which imposes the maximum imaging acquisition rate. This value is similar to most commercially available SS-OCT systems, as previously presented in Table 1.2.

Although the laser generates a maximum of 1510 samples, only 1376 of them are contained in the tunning range, where the wavelengths are conveniently swept. This imposes that only about 91% of the total bandwidth is used. In Figure 2.4 we can see that in reality an additional portion of wavelengths is present both above and below the tunning range. This 1376 samples will establish the number of points of the digitized A-Scan.

As previously mentioned, besides the laser output, the light source is also responsible for generating two electronic signals: the Sweep Trigger and the Clock signal, whose functionality will hereafter be addressed.

2.2.2   Sweep Trigger and Clock

The Sweep Trigger can be considered an auxiliary signal used to coordinate the initialization of each A-Scan with its acquisition process. It consists on a digital wave which changes its state from low to high when the sweeping of the wavelengths begins, returns to the low state when the whole 1510 samples are generated and goes back to high state almost immediately after to begin a new A-Scan sweeping and acquisition, repeating the cycle. The frequency of this signal is the specified sweep frequency of 100 kHz, that dictates the A-Scan generation rate.

Besides being synchronized with the laser output, the Sweep Trigger is also synchronized with the Clock signal. This clock is responsible for controlling the acquisition of an A-Scan, making the correspondence between the swept 110 nm and the 1376 digital samples dedicated to this bandwidth. For this, the Clock is clearly differentiated in two phases: A Sweeping Clock with a variable frequency that corresponds to the sweeping of the laser, and a Dummy Clock of constant frequency in which the laser output is actually turned off. In Table 2.1 it was specified a duty cycle of 45%. This parameter indicates the ratio between the time interval the laser is turned on and the time interval it is turned off. Because of the uneven Clock frequency, although the Sweeping Clock phase of the duty cycle is only 45%, 1376 of the total 1510 samples (about 91%) are generated during this phase.

A plot of the evolution of the laser output, Sweep Trigger and Clock signal through time is the best way to understand how they all relate. This is presented in Figure 2.5.

Note that the plotted variable in the bottom graph is the Clock frequency, which should not be mistaken for the Clock signal itself. The Clock signal can be seen in Figure 2.6.

The reason why the Sweeping Clock displays a frequency varying pattern is to automatically digitize the acquired interference signal into even intervals in the k space, producing a linear A-Scan. Because the acquired interference signal will be linearly distributed in time (λ space) but non-linearly distributed in the k space, this linearizion process is mandatory before applying the inverse Fourier transform (as explained in 1.4.3 - Overall Comparison). Doing so by taking advantage of this clock property rather than performing it by means of data preprocessing is a great advantage, reducing computation time and effort. As for the Dummy Clock, its function is to merely fill in the gap between the end of the sweeping process in
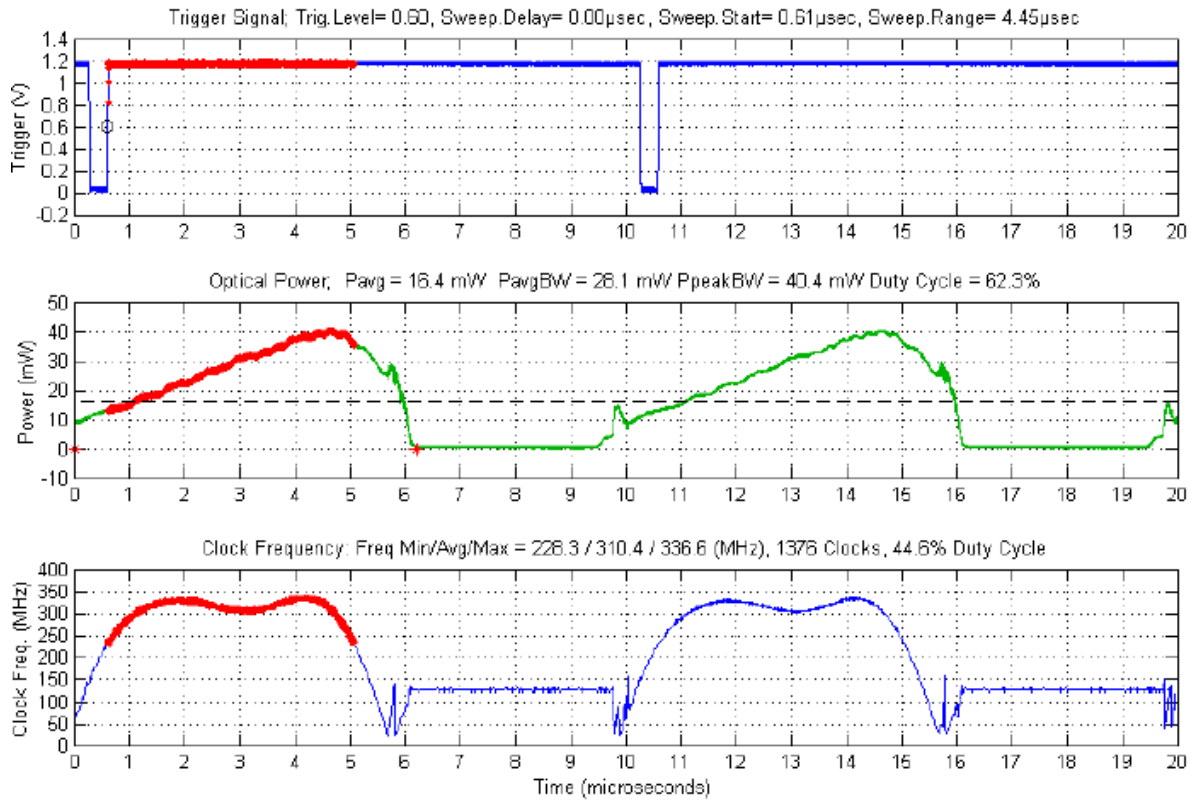
Figure 2.5: Typical Spectral Power and Clock Data for the SSOCT-1060 Engine[31].

which the laser output power gradually returns to zero and the beginning of a new one.

2.2.3 Limits on Imaging Parameters

Certain imaging optical parameters are limited by the light source, namely the axial resolution and the maximum imaging depth. As aforementioned, the axial resolution is an optical parameter set by the light source which expresses the image resolution in the direction of the incident light and is defined as half the coherence length l_c (given in Equation 1.1). Thus, it can be written as:

$$\delta z = \frac{l_c}{2} = \frac{2\ln(2)}{\pi}\frac{\lambda_0^2}{\Delta\lambda} \tag{2.3}$$

Where λ_0 is the central wavelength of the light source and $\Delta\lambda$ is the swept bandwidth. This equation also assumes a refractive index of $n = 1$, which is a fair assumption for an eye. If we do this calculation according the specifications of our light source the yield axial resolution is:

$$\delta z = 4.51\ \mu m$$

As for the maximum imaging depth, it can be calculated based on the previously presented Equation 1.43. By substituting $M = 1376$ and δz for the above value, we obtain the value:

$$z_{max} = 6.21\ mm$$

49
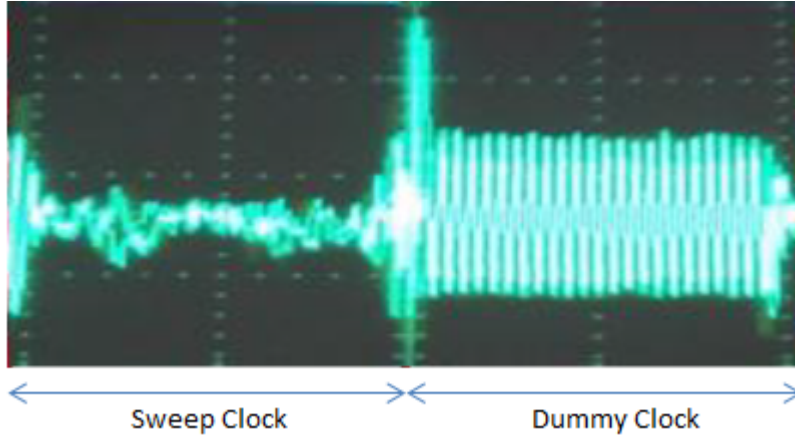
Figure 2.6: Clock signal of the SSOCT-1060 acquired by an oscilloscope.

It is important to note that these parameters are simply the limits imposed by the light source alone, and do not account for imaging artifacts nor the properties of the sample such as scattering or absorption coefficients, that also have an impact in the axial resolution and maximum scanning depth. Therefore, when measuring these parameters they will naturally not be as favorable as here expressed.

We can also calculate the instantaneous swept linewidth $\delta\lambda$ and swept wavenumber interval δk using the previously presented Equations 1.48 and 1.46, respectively, yielding the values:

$$\delta\lambda = \frac{110\ nm}{1376} = 79.9\ pm$$

$$\delta k = 2\pi\ \frac{110}{1060^2 - \frac{110^2}{4}} = 6.17 \times 10^{-4} rad/nm$$

As expected of an SS-OCT system, although a broadband of bandwidths is swept, each swept bandwidth $\delta\lambda$ (referred to as linewidth) is actually quite narrow.

Finally, it is also possible to calculate the source's coherence length using Equation 1.1. However, because a swept source is being used, it is the instantaneous linewidth that should be taken into account for this calculation, instead of the entire bandwidth of the light source. When doing so, we obtain:

$$l_c = 12.41\ mm$$

Which is within the typical range specified by the manufacturers (Table 2.1).

2.3   Balanced Detector

In any acquisition system, the detector makes the link between the physical world and the electric version of it. The detector used in this OCT is a balanced detector, which means that it has two inputs, and outputs a voltage proportional to the difference of the photocurrents in the two inputs. As discussed in 1.5.4 -

DC Component, this balancing brings a great advantage in terms of reducing the DC component artifact. The balanced detector chosen was a Thorlabs PDB471C (Figure 2.7).

Figure 2.7: Thorlabs PDB471C.

2.3.1 Specifications and Operation Principles

The most relevant specifications of this detector for an OCT imaging application are presented in Table 2.2.

Parameter	Value
Operating Wavelength	900 - 1400 nm
RF Output Bandwidth	0 - 400 MHz
Responsivity	0.72 A/W at 1060 nm
RF Output Transimpedance Gain	10×10^3 V/A
Max RF Output Voltage	$\pm$ 3.8 V (high impedance loads) $\pm$ 1.9 V (50 Ω loads)
CMRR	>25 dB (typical 30 dB)
RF Output Impedance	50 Ω
Overall Output Voltage Noise	<2.0 mV_{RMS}

Table 2.2: Technical specifications for the Thorlabs PDB471C (Valid for 23 ± 5 ℃) [32].

This specific model is recommended by the manufacturers for OCT applications and is optimized for a wavelength of 1060 nm, which is a perfect match for this system. It consists on two well-matched InGaAs photodiodes and an ultra-low noise, ultra-low distortion, high-speed transimpedance amplifier that generates an output voltage (RF OUTPUT) proportional to the difference between the photocurrents of the two photodiodes, i.e. the difference between the two optical input signals (Figure 2.8) [32].

This output voltage can be mathematically expressed as [32]:

$$U_{RF,OUT} = (P_{opt,1} - P_{opt,2}) \times R(\lambda) \times G \tag{2.4}$$
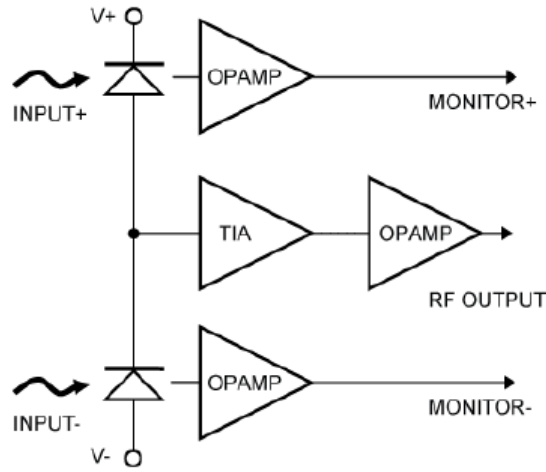
Figure 2.8: Functional block diagram of the Thorlabs PDB471C[32] .

In which $R(\lambda)$ symbolizes the responsivity of the photodiode at a given wavelength, $P_{opt,1}$ and $P_{opt,2}$ the input power of each input channel and G the transimpedance gain factor in the RF output. Although a specified value for the responsivity at wavelength of 1060 nm was given in Table 2.2, this parameter varies for different wavelengths according to the responsivity curve plotted in Figure 2.9.
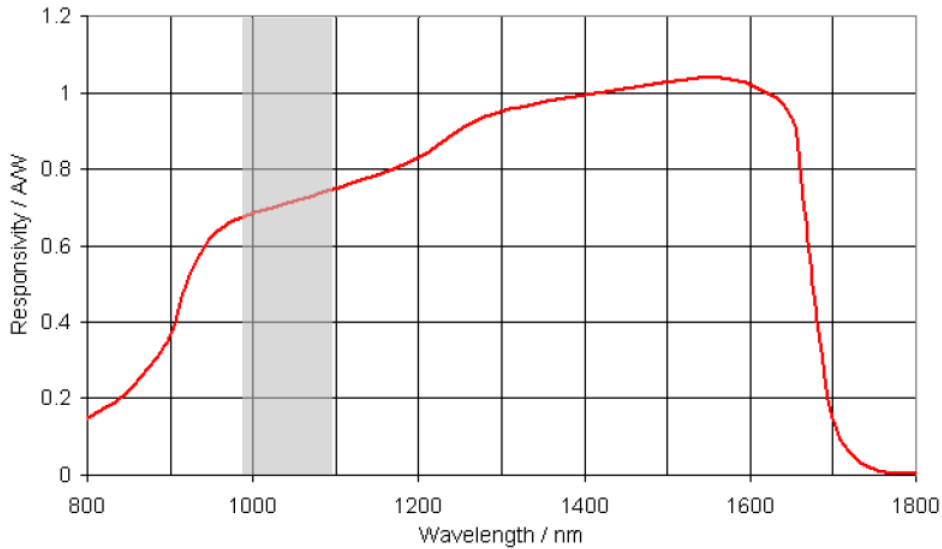
Figure 2.9: Typical responsivity of the Thorlabs PDB471C. The highlighted region corresponds to the wavelength range of the used light source[32]. (Adapted).

Because this detector is optimized for the central wavelength of 1060 nm, in the near region which includes the whole bandwidth of the light source, the responsivity curve is practically linear.

Additionally, as seen on Figure 2.8, this unit has two monitor outputs (MONITOR+ and MONITOR-) that allow the observation of the photodiode's power level in each optical input separately.

2.3.2   Limits on Imaging Parameters

The detector used in an OCT system can potentially limit the axial measurement range if its bandwidth is not greater than the maximum frequency of the interference signal, as explained when the functioning of a SS-OCT system was presented. Therefore, it is important to know the maximum detectable frequency of the system, which is given by Equation 1.45. The parameters δk, z_{max} and f_{sweep} were either calculated or specified in the last section, which allows us to perform the calculation:

$$f_{max} = (6.17 \times 10^{-4}) \; \times (100 \times 10^3) \; \times \frac{(6.21 \times 10^6)}{\pi} = 122.0 \; MHz$$

Because the selected detector has a maximum output bandwidth of $400 \; MHz$ (Table 2.2), its bandwidth is much greater than the maximum detectable frequency of the interference signal f_{max}. Consequently, we can safely consider that this detector will not limit the measurement depth range.

2.4   DAQ Board

This is the main component of the data acquisition system, since it is responsible for acquiring the analogical electrical signals, converting them to digital signals and sending them to the host PC for processing. In this specific OCT system, the DAQ board also plays a role in data processing, as we will see ahead.

The chosen unit is actually constituted by two elements: the XMC Module X5-400M by Innovative Integration (Figure 2.10), which is coupled with the PCI Express Host Interface also by Innovative Integration (Figure 2.11) to provide data transfers to the PC as well as from the PC to the X5-400M[33].
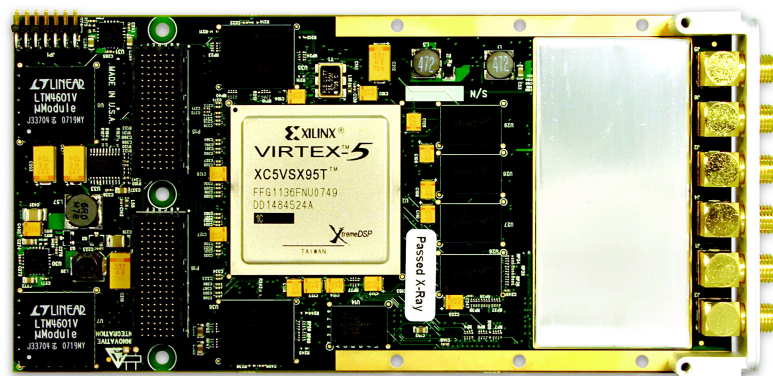
Figure 2.10: X5-400M by Innovative Integration[33].

Both of these components are located inside the host computer, as suggested in Figure 2.2.
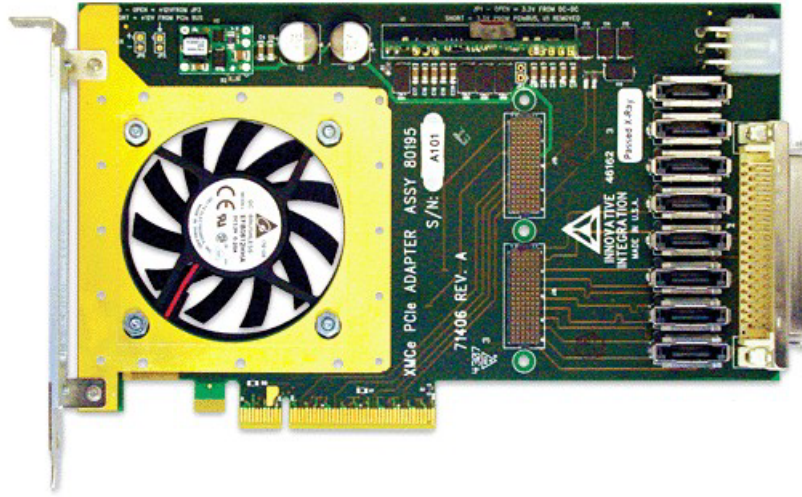
Figure 2.11: PCI Express Host Interface by Innovative Integration [33].

2.4.1   Features and Block Diagram

The main features of the X5-400M Module coupled with the PCIe (PCI Express) interface are presented in Table 2.3.

Features
Xilinx Virtex5 SX95T FPGA Computing Core
Two 14-bit ADC Channels (400 MSPS)
Two 16-bit DAC Channels (500 MSPS)
$\pm$ 1 V, 50 Ω, SMA Inputs and Outputs
Internal or External Clock
Internal or External Triggering
One bank of 512 MB DDR2 DRAM
Two banks of 2 MB QDR2 SRAM
>1 GB/s, 8-lane PCIe Host Interface

Table 2.3: Features of the X5-400M Module coupled with the PCIe interface [33].

The Virtex5 is an FPGA-based computing core that controls the data acquisition process, provides data buffing and I/O host communications. Despite being equipped with two ADC and two DAC channels, this specific application only makes use of one ADC channel, which has 14-bit resolution and sampling rate of 400 MSPS (Mega Samples Per Second). Because the two ADC channels are simultaneously sampling, even if only one is used, the data output format is codified in 2's complement [33]. We will get a deeper comprehension on this subject in the follwing chapter (3 - Acquisition Software). The ADC and DAC channels operate synchronously governed by the same clock. An internal or external clock can be used [33]. Since the light source provides an optimized Clock signal for OCT imaging, as previously explained, this external clock is used, being connected directly from the light source to the external clock input of the X5-400M (identified as CLK). The source's Sweep Trigger is also connected to one input of this board, this time the triggering input (identified as SYNC). The X5-400M also has two sets of memory devices, in charge of different functions as will be detailed ahead.

The attached PCIe interface is capable of providing over 1 GB/s sustained data transfers to the PC, and in both directions simultaneously[33].

To understand how these mentioned units correlate to each other, a block diagram is presented in Figure 2.12.
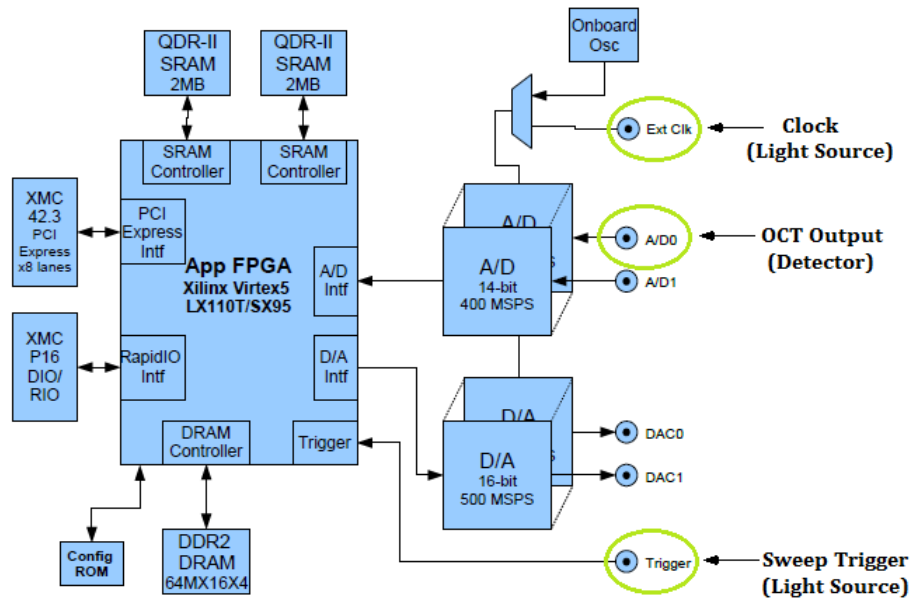
Figure 2.12: Block Diagram of the X5-400M. The green selections represent the inputs that connect with either the light source (Ext Clk and Trigger) or the detector (A/D0)[33]. (Adapted).

Despite being the A/D 0 channel input the selected one to connect with the detector output, this choice is absolutely arbitrarily, being the A/D 1 equally suitable.

2.4.2 Memory Types

There are two sets of memory devices attached to the FPGA: The SRAM (Static Random Access Memory) to provide computational memory and the DRAM (Dynamic Random Access Memory) for data buffering.

SRAM (Computational)

The X5-400M has two banks of 2 MB QDR SRAM (Quad Data Rate Static Random Access Memory) dedicated as FPGA local memory for computational tasks. Therefore, the SRAM devices connected to the FPGA are 4 MB in total size. This memory may also be used as a local buffer memory if the data buffer is too large to fit in FPGA block RAMs, or as memory for an embedded processor in the FPGA. Because all SRAM control and data lines pins are directly connected to the FPGA, the developer can customize this memory to suit the purposes of the specific application[32].

The SRAM has an high performance FIFO interface that allows the logic to fully exploit the high data rates to the QDR SRAM by providing support for posted writes, read address queue and read data queue[32].

DRAM (Data Buffering)

This set of memory provides a 512 MB DDR2 memory pool local to the FPGA. The data buffer is implemented with one or more queues for the A/D and D/A streams as appropriate for the particular X5 module[33].

Although the total DRAM on board the X5-400M is 512 MB, the standard firmware statically allocates one-quarter of this memory to each of the four analog I/O channels on the card[34]. Seeing that in our specific application only one I/O channel is used, the true available memory for data buffering is reduced to 128 MB.

2.4.3 Data Transfers

In this application, the X5-400M is coupled with a PCIe interface (Figure 2.11) in charge of transferring the acquired A-Scans, after being converted by the ADC and placed on the DRAM, from this memory to the host PC memory. It is also responsible for establishing the communication the other way around, by sending certain acquisition specifications from the host computer to the FPGA to optimize the acquisition process, such as the number of ADC channels used, the expected size of each data packet and other acquisition parameters. It provides a full duplex link to the host computer.

The application logic interface responsible for this data stream is the Velocia Packet Interface. When data packets are created by this application logic, in our case A/D samples, data flows over the data link as packets. The specified maximum transfer rate over the data link is 2 GB/s. However, the assured sustained rates are 1.2 GB/s when working at half-duplex and 1.0 GB/s when working at full-duplex[33].

2.4.4 FrameWork Logic

As previously mentioned, besides connecting the output of the detector to one of the ADC channels of this board, the Sweep Trigger and the Clock generated by the light source are also used as inputs. During the acquisition process, the clock specifies the instant in time when data is sampled, whereas triggering specifies when data is kept. This allows the application to collect data at the desired rate, and keep only the data that is required[33].

Additionally to these two acquisition control inputs, an internal digital signal nominated Sample Enable is used to regulate the acquisition. The signal in the ADC input channel is converted and acquired whenever the Sample Enabled is in high sate and a rising edge of the clock signal occurs. However, the application logic of the FPGA allows the support of two distinct acquisition modes: Unframed Mode and Framed Mode.

In unframed mode, the Sample Enable is simply a playback of the input trigger signal, i.e. it is true (high state) when the input trigger is true, and false (low state) when the input trigger is false. Therefore samples are collected whenever the input trigger is true and a rising edge of clock signal happens. Thus, we can speak of a continuous acquisition.

In framed mode, the Sample Enable signal goes true when a rising edge of the

input trigger occurs. However, this time it stays in this state for a predetermined number N of collected samples. Once this N A/D conversions are made, the Sample Enable goes back to false, regardless of the state of the input trigger. Even if the rising edge of the input trigger is immediately followed by a falling edge, the Sample Enable will stay true until the acquisition of the N samples is finished. On the other hand, rising edges of the input trigger that occur during this acquisition period are ignored. Only when the N points are acquired and new rising edge of the input trigger occurs will the Sample Enable be true again.

Both of these acquisition scenarios are conveniently represented in Figure 2.13.
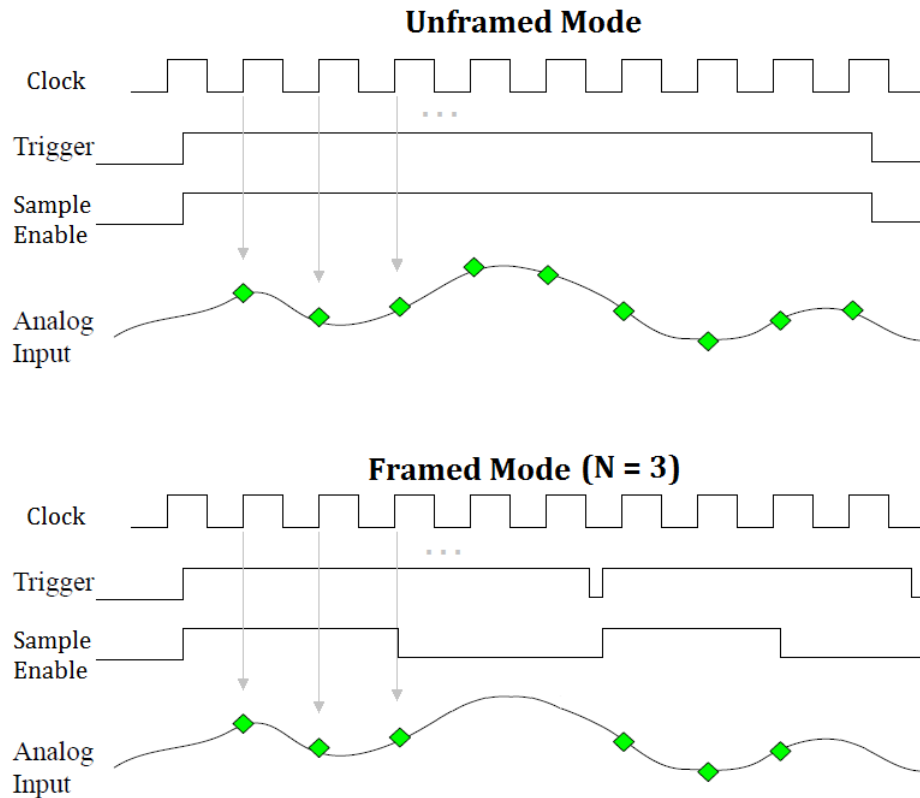
Figure 2.13: Example of the same analogical signal being acquired in Unframed Mode and in Framed Mode. Each green square symbolizes one A/D conversion and acquisition. The gray vertical arrow simply highlights that these conversions and acquisitions happen on the rising edge of the clock signal.[33] (Adapted).

Framed trigger mode is useful for collecting data sets of a fixed size each time the input trigger is fired[33]. This is precisely the case in this OCT application: Once the Sweep Trigger is fired, 1376 samples generated by the light source are expected to be acquired. Therefore, the framed mode is the acquisition mode selected for this application.

To maintain clarity throughout this work, we will designate as:

- **Sample/Point** - Each of the predetermined number of conversions N that are acquired when the Sweep Trigger is fired, thus corresponding to a data point on each A-Scan.

- **Frame** - The collection of the whole N Samples acquired on each fired Sweep Trigger, thus corresponding to the data of an entire A-Scan.

- **Packet** - The collection of Frames that are grouped together to be copied to the host PC simultaneously on a single instruction. It can have a variable size,

determined by the user when programming the acquisition parameters of the X5-400M.

For the framed mode, due to the X5-400M specifications, the predetermined frame size N must be a multiple of 256, between $2 < N < 16777216$, to reduce the number of bits used for comparison and control for simplicity [33]. This imposes a problem in our OCT application, since the light source generates a fixed number of 1376 samples in each Sweep Trigger, which is not a multiple of 256. To overcome this, the frame size selected should be the nearest multiple of 256 that is greater than 1376. That number is $N = 256 \times 6 = 1536$. This means that in each acquired frame, along with the 1376 relevant samples of the A-Scan, the remaining $1536 - 1376 = 160$ points will contain irrelevant data, as they will be acquired when the laser output is off at the pace of the Dummy Clock. Dealing with this extra information is a processing task at charge of the developed software for this OCT, and will be detailed in the follwing chapter (3 - Acquisition Software).

Figure 2.14 shows the whole FrameWork Logic data flow to summarize the above explanations.
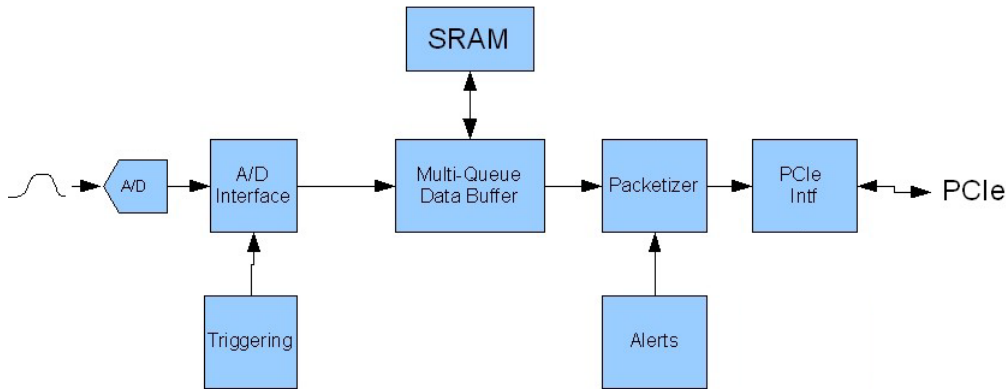
Figure 2.14: X5-400M FrameWork Logic Data Flow [33]. (Adapted).

2.4.5 Malibu Library

To provide an efficient communication between the DAQ board and the host PC, the X5-400M features a software library named Malibu, also developed by Innovative Integration. This library is designed to match up with the demands of software developing in applications where high-speed data flow is a requirement, to provide real time signal analysis on the PC as is necessary in OCT imaging. Besides supporting high-speed data streaming in communication with the host PC, it also features a wealth of host functions to perform data processing and visualization tasks.

To support programming of Innovative hardware products under Windows and Linux, Malibu combines with the Microsoft or Embarcadero (Windows) and GNU C++ compilers (Windows/Linux) and the MS Visual Studio and QtCreator IDEs. Malibu adds high performance data acquisition and data processing capabilities to Microsoft Visual C++, CodeGear or GNU C++ applications with a complete set of functions that solve data movement, analysis, viewing, logging and fully take advantage of the object-oriented nature of C++ [36].

2.5   Pulse Configuration

When leaving the Axsun SSOCT-1060 light source, the Sweep Trigger is a TTL wave with voltage ranging from $0\ V$ to $1.2\ V$. However, the X5-400M DAQ board requires an input trigger with range from $0\ V$ to $5\ V$. Because of this incompatibility, there is the need to amplify the Sweep Trigger as it leaves the light source, to assure the compliance with the DAQ board specifications.

However, this amplitude transformation is not the only one that needs to be made. As previously said, the Sweep Trigger is synchronized with the laser output as it sweeps the wavelength range. But it is important to notice that this synchronization is only true the instant these signals leave the light source. Because in this application light will travel a considerable length in both optical fiber and air, when both signals reach the DAQ board, the referred synchronization is lost, or at least not as precise as it should be. In previous work incident on this OCT system, the time delay associated with this desynchronization was determined to be $\Delta t = 90\ ns$[27]. Therefore, a delay adjustment of $90\ ns$ to the Sweep Trigger should also be taken into account.

To perform both these transformations, before entering the DAQ board the Sweep Trigger passes through the Digital Delay and Pulse Generator DG535 from Standford Research Systems (Figure 2.15). The output signal of this unit is the same as the input except for the mentioned amplification and time delay adjustments.

Figure 2.15: Digital Delay and Pulse Generator DG535[37].

Despite making use of the DG535, the same purposes could be served resorting to simple electronics. An electronic circuit (e.g. the standard non-inverting amplifier circuit) using only operational amplifiers and resistors with the right electrical resistance could produce the same desired amplitude gain.

As for the time delay adjustment, because the cables used to connect the Sweep Trigger have a specified propagation velocity of 69.5% the speed of light in vacuum, it is possible to calculate the cable length L required to produce the desired delay of $\Delta t = 90\ ns$:

$$L = v \times \Delta t = 0.695c \times (90 \times 10^{-9}) = 18.75\ m \tag{2.5}$$

Which is actually a quite considerable length. That being said, because this pulse configuration unit was available, it was considered the most practical and economical way of making the desired transformations to the Sweep Trigger.

2.6 Galvo Scanners

As previously mentioned, acquiring a B-Scan implies the need of focusing the incident laser beam in successive points across a line, which we will consider to be the x-axis. Furthermore, in order to acquire a volume, this laser sweep across the sample must be repeated for successive lines along the y-axis (refer back to Figure 1.37).

For this, a scanning mechanism must be in charge of directing the laser beam in the appropriate point of the sample. This task must be in complete harmony with the acquisition process, which is typically a big challenge and to successfully overcome it the scanning mechanism must be very precise and fast.

In this work the GVS002 Dual-Axis Scanning Galvo System (Figure 2.16) from Thorlabs is used for the mentioned job.
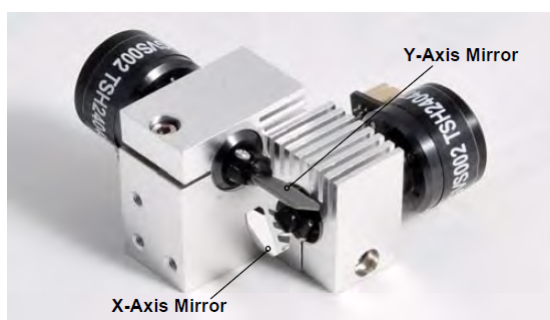
Figure 2.16: GVS002 Dual Axis Galvo/Mirror Assembly[38].

2.6.1 Specifications and Operation Principles

The most relevant specifications of the GVS002 are exposed in Table 2.4.

Parameter	Value
Scan Angle Range	± 12.5°
Input Position Signal Range	± 10 V
Input Position Signal Scale Factor	switchable: 0.5V/ °, 0.8V/ °or 1.0 V/ °
Full Scale Bandwidth	Square wave - 100 Hz Sine wave - 250 Hz Sawtooth wave - 175 Hz
Small Angle (± 0.2 °) Response	300 μs
Resolution	0.0008°
Linearity	99.9 %
Output Position Signal Scale Factor	0.5 V/ °

Table 2.4: Technical specifications of the GVS002 Galvanometer System (Valid for temperatures < 50 ℃)[38].

The galvanometer system consists of two galvanometer-based scanning motors with a silver coated mirror mounted on the shaft of each one, providing a reflectivity greater than 95 % for the used wavelength range. The movement of the mirrors is

driven by a galvo motor featuring a rotating magnet and a stationary coil design. This configuration provides faster response and higher system-resonant frequencies when compared to moving coil configurations[38].

The system is also equipped with a feedback system that provides information on the mirror's position (Output Positional Signal), a useful tool to monitor the mirror behavior and its response to the Input Position Signal. The mirror position information is provided by an optical position detector, which consists of two pairs of photodiodes and a light source. As the mirrors are moved, differing amounts of light are detected by the photodiodes and a current is produced relatively to the galvo actuator position[38].

The functioning of these two main components is driven by a servo driver circuit (Figure 2.17), which is the intermediary between the mirrors and the signals sent to or received from it.
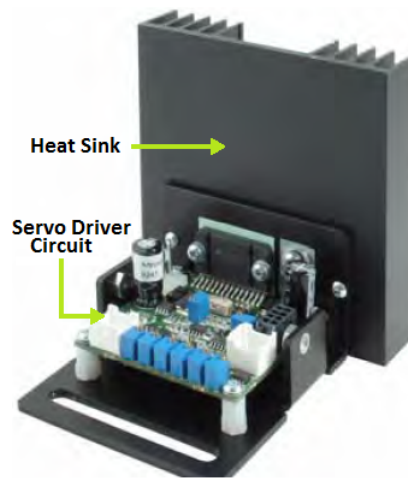
Figure 2.17: Servo Driver Board with the Heat Sink attached[38].

The power supply of the driver board is in charge of the GPS011 unit (Component 11 in Figure 2.2), as recommended by Thorlabs in order to maximize the capabilities of the galvanometer system.

As mentioned in the specifications presented in Table 2.4, a switchable scale factor allows having three different ratios between the amplitude (Volts) of the input signal and the corresponding position (°) of the mirror: 1 V/° 0.8 V/° and 0.5 V/° . This selection is made by setting the position of a jumper present in servo driver circuit as indicated in Figure 2.18.
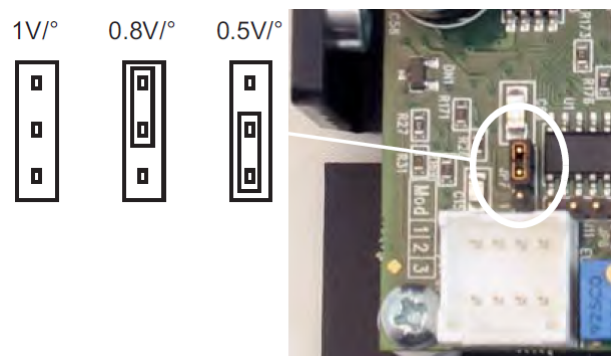
Figure 2.18: Setting the Volts/Degree Scaling Factor[38].

Taking into consideration the input position signal range of ± 10 V, the 1 V/° scale will allow a maximum scan angle of $\frac{\pm 10}{1} = \pm 10°$ whereas the 0.8 V/° scale

grants the maximum angle range of $\frac{\pm 10}{0.8} = \pm 12.5°$. As for the 0.5V/° scaling factor, it is provided to allow the full scan angle to be achieved using small input signals, limited to ± 6.25 V. Therefore it equally allows obtaining the range $\frac{\pm 6.25}{0.5} = \pm 12.5°$ but using inputs signals with lower amplitude[38].

In this OCT imaging application, either using a small animal's eye or in other samples for testing, the scanning angle is typically inferior to ± 5 °, therefore the scaling factor typically used is the 1 V/° which is more than enough to grant that the whole sample can be scanned if the appropriate input signal is used.

2.6.2   X-Axis Mirror Scan

As has been highlighted throughout this work, it is essential to assure the synchronization between the scanning and the acquisition. In other words, it is only possible to successfully build a B-Scan through data processing of a collection of A-Scans if these are acquired at the correct instants and positions. Once the acquisition process begins, a previously defined number of A-Scans are expected to be contained in a B-Scan. The same logic is expanded when acquiring a volume: a previously defined number of B-Scans are expected to be contained in the volume scan. Therefore the acquisition settings must be in agreement with the input position waveform sent to the galvo mirrors.

Let us define N_A as the number of A-Scans in each B-Scan. If the acquisition software is expecting to acquire N_A A-Scans, the duration of this acquisition is given by the duration of each Sweep Trigger (corresponding to the acquisition of 1 A-Scan) multiplied the N_A intended A-Scans. The scanning frequency of the x-axis mirror is then given by:

$$f_x = \frac{f_{\text{sweep}}}{N_A} \tag{2.6}$$

As previously discussed, the sweeping frequency is a characteristic determined by the light source and has a fixed value of $f_{\text{sweep}} = 100 \ kHz$.

If traducing the x-mirror scan movement when acquiring a B-Scan to a waveform, it would ideally be a sawtooth wave with a 100:0% symmetry, i. e. composed by an ascending phase which fits all of the N_A Sweep Triggers followed by an instantaneous drop, with a duration inferior to the interval in-between triggers, which is of $T_{\text{sweep}} = \frac{1}{f_{\text{sweep}}} = 10 \ \mu s$. Therefore, this is precisely the input position signal that is sent to the x-mirror servo driver, as represented in Figure 2.19 additionally with the output position read from the correspondent connector from the same servo driver board.

Note that, as specified in Table 2.18, the output position signal has a scaling factor of 0.5 V/° which is why the amplitude (vertical division) of the oscilloscope channel reading this signal was adjusted to be the double of the input signal.

Although the GVS002 specifications indicate a small response time of 300 μs, it only accounts for the time it takes for the mirror to settle into position when the angle shift is inferior to ± 0.2 °. For a larger angle such as the case of the sudden drop from the maximum to the minimum amplitude of the input waveform, the response will be considerably slower.

Therefore, the response time on this situation was empirically determined by experiments similar to the one presented in Figure 2.19. As can be seen, it takes about 1 ms for the mirror to get back to the initial position to start a new scan.
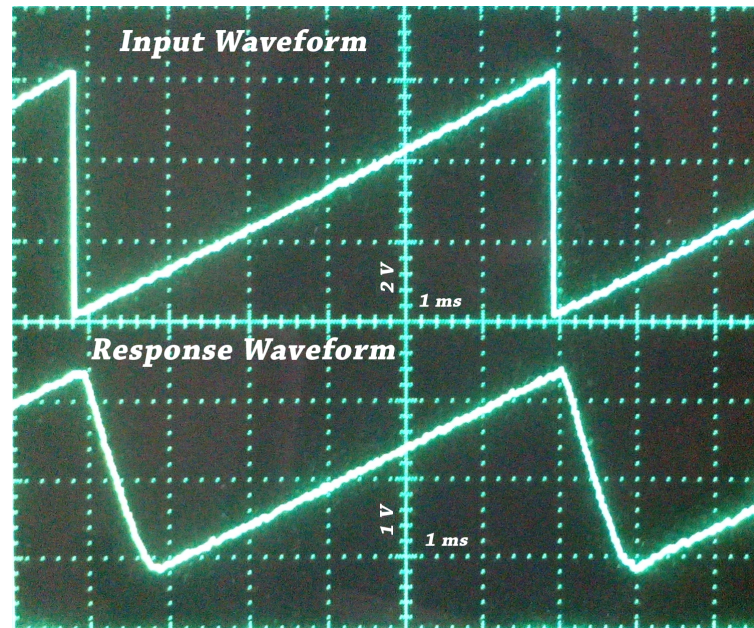
Figure 2.19: Input waveform (above) and response waveform (below) representing respectively the input position signal and the feedback output position signal of the x-axis mirror. The waveforms correspond to a B-Scan acquisition containing 612 A-Scans.

Seeing that $f_{\text{sweep}} = 100 \ kHz$, around 100 A-Scans are acquired in this backward movement which do not correspond to a proper scanning of the sample and therefore are ignored in the data processing. This subject will be detailed in Chapter 3 - Acquisition Software.

By analyzing Figure 2.19 we can also detect a small drop in the amplitude of the response waveform, meaning that the mirror begins the descending motion before reaching the supposed maximum scan angle and vice-versa for the minimum scan angle. This is because in this test, referring to an acquisition of 612 A-Scans, the theoretical x-mirror galvo frequency is of $f_x = 163.4 \ Hz$. Although the specified full scale bandwidth for a sawtooth wave is 175 Hz, this value supposes a symmetrical 50:50 % sawtooth wave, which is not the case. In fact, the input waveform can be considered a mid-term between a sawtooth wave and a square wave. Because for a square wave we have a maximum bandwidth of 100 Hz, it is comprehensible that the determined input signal frequency for this specific waveform exceeds the recommended full scale bandwidth, giving rise to this amplitude decrease. By performing similar tests along a range of input wavelengths it was concluded that for input signals inferior to about 150 Hz this artifact is no longer verified. In any case, it is important to mention that this scanning angle amplitude decrease is not necessarily prejudicial in this OCT application because the galvanometer system allows a scan angle range much wider than necessary.

2.6.3 Y-Axis Mirror Scan

The y-axis scanning is necessary when acquiring a volume of the sample. While the x-axis mirror changes the scanning angle for each A-Scan acquisition, the y-axis mirror varies the scanning angle for every B-Scan acquisition. In fact, it is crucial that the y-axis mirror remains static while each B-Scan is acquired to ensure that

the A-Scans are scanned throughout a one dimensional line. Only after each B-Scan acquisition is finished should the y-axis mirror change its scan angle.

From the above explanation we can conclude that the input waveform frequency of the y-axis mirror shall be inferior to the x-axis one, being given by:

$$f_y = \frac{f_{\text{sweep}}}{N_A \times N_B} = \frac{f_x}{N_B} \tag{2.7}$$

In which N_B accounts for the number of B-Scans in each volume scan. This time, when the y-axis scanning is concluded an entire volume was acquired. Therefore, the time it takes to acquire a volume of the sample is:

$$T_{\text{volume}} = \frac{1}{f_y} = \frac{N_A \times N_B}{f_{\text{sweep}}} \tag{2.8}$$

To give a clearer insight on how both scanning mirrors relate to each other, the input waveforms injected to each of them was simultaneously acquired by different channels of an oscilloscope, with the result presented in Figure 2.20-A. The scanning parameters were relative to consecutive volume acquisitions of 128 B-Scans, each containing 612 A-Scans (from now on we will abbreviate this as a 612×128 volume).
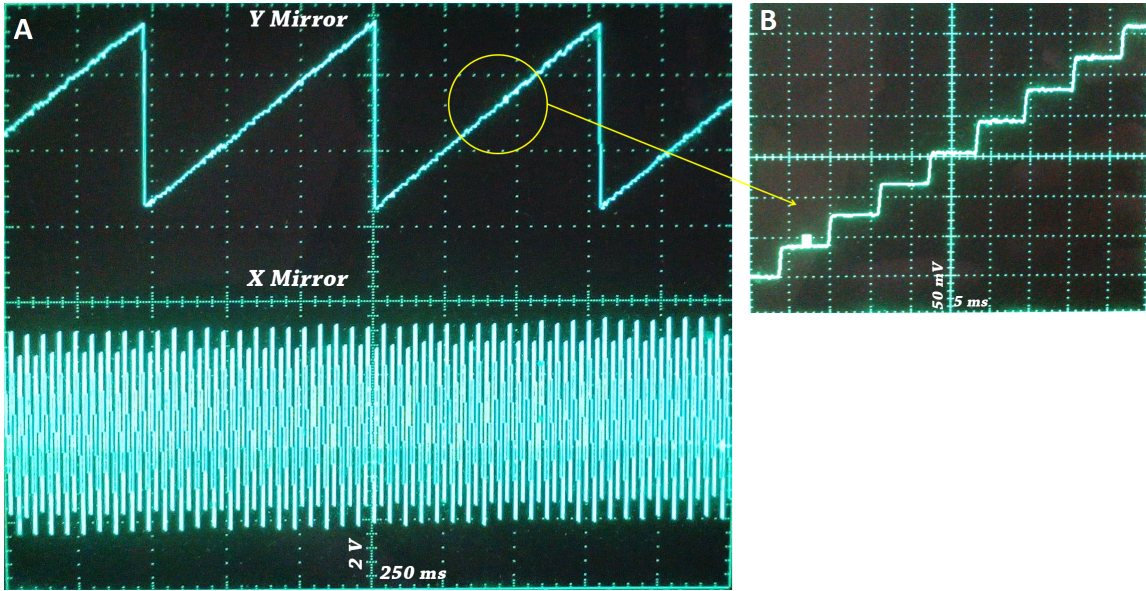
Figure 2.20: (A) Input positional signal injected to the y-axis mirror (above) and the x-axis mirror (below), corresponding to consecutive volume acquisitions of 612×128. (B) Close up on the input positional signal injected to the y-axis, obtained by decreasing the oscilloscope's time scale.

As we can see, despite resembling a sawtooth similar to the x-axis mirror input waveform, the y-axis mirror one is actually not a continuously increasing function, but rather composed by several steps as can bee seen when the oscilloscope's time scale is decreased (Figure 2.20-B). For simplicity we will designate this waveform as the y-axis sawtooth.

The number of steps contained in this signal is equal to the determined number of B-Scans. As for the duration of each one, should be equal to the time it takes for the determined N_A A-Scans to be acquired, thereby equal to:

$$T_{\text{y-step}} = \frac{1}{f_x} = \frac{N_a}{f_{\text{sweep}}} \tag{2.9}$$

In the exemplified 612×128 volume this time should be of $T_{\text{y-step}} = \frac{612}{100 \ kHz} = 6.12 \ ms$, which is what we can observe in Figure 2.20-B.

The expected time to acquire the 612×128 volume can be calculated using Equation 2.8, yielding the value $T_{\text{volume}} = \frac{612 \times 128}{100 \ kHz} = 783 \ ms$, which is in accordance with what is observed in Figure 2.20-A.

2.7 Signal Generator

Now that the galvanometer mirror scanning system has been explained, only the components responsible for generating the signals injected to this system are left to present.

Because of the different shape and nature of the x-axis and y-axis scanning waveforms, as well as to facilitate the synchronism between the scanning and the acquisition, two different units are used to generate the mentioned waveforms. We will begin with the responsible for generating the x-axis scanning waveform, which is the AFG3101 Arbitrary Function Generator by Tektronix (Figure 2.21).
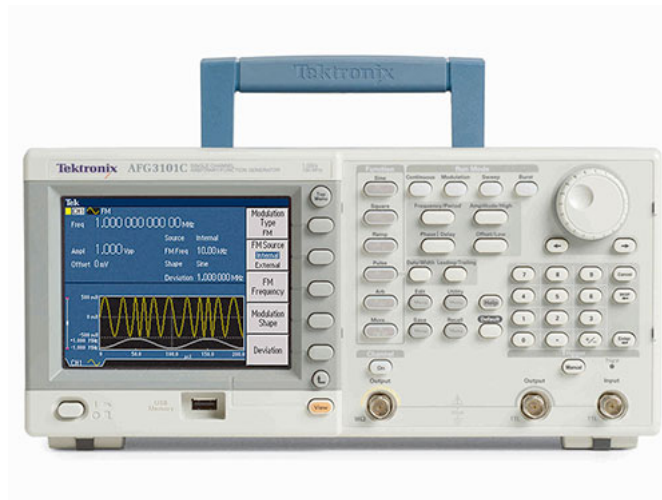
Figure 2.21: AFG3101 Arbitrary Function Generator used for generating the x-axis scanning waveform[39].

2.7.1 Specifications and Overview

This function generator has the ability of generating a multitude of different waveforms, such as: Sine, Square, Pulse, Ramp, DC, Random Noise, Sin(x)/x, Gaussian, Lorenz, Exponential (Rise and Decay) and Haversine[39].

Having explained the functioning principle of the x-axis scanning, we can easily understand that the suitable waveform for our purpose is the ramp. A ramp waveform is similar to a sawtooth, except that its ascending part is not necessarily symmetric to the descending part, in terms of time duration. We can say that a sawtooth is a particular ramp signal in which the symmetry is set to 50:50.

The most relevant specifications for a ramp waveform generated by the AFG3101 are presented in Table 2.5.

Parameter	Value (Ramp Wave)
Waveform Samples Range	2 to 16 384 Samples
Sampling Rate	1 GS/s
Frequency Range	1 mHz to 100 MHz
Frequency Resolution	1 μHz
Amplitude Range	20 mV$_{pp}$ to 10 V$_{pp}$
Amplitude Resolution	0.1 mV$_{pp}$
Symmetry Range	0 % to 100.0 %
Phase Range	-180.00° to 180.00°
DC Offset Range	$\pm$ 5 V$_{pp}$

Table 2.5: Technical specifications of the AFG3101 referring to a ramp waveform [39].

Besides setting the desired signal waveform, the user can also select different output modes: Continuous, Modulation, Sweep and Burst. In the Continuous, the unit is continuously outputting the determined waveform, while the Modulation mode also continuously outputs the selected waveform but modulated in amplitude with a certain frequency, shape and depth of modulation determined by the user. The Sweep mode outputs a waveform with the output signal frequency varying linearly or logarithmically. Finally, in the gated Burst mode, the output is enabled or disabled basing on the internal gate signal or an external signal applied to the front-panel Trigger Input connector. While the gate signal is true (high state), the instrument outputs a continuous waveform [39].

Since in our OCT application this unit is not controlled by the application software, the selected output mode is the Burst mode to prevent the galvo mirrors from being continuously scanning when the system is not making any acquisition. The burst trigger used to enable or disable the output is controlled by the acquisition software, and therefore can simply set this trigger signal to true just as the acquisition is about to begin, and to false as soon as it ends.

2.7.2   Adjusting the Waveform

An example of a waveform generated by this unit was already presented in Figure 2.19 (Input Waveform). This specific ramp signal has symmetry 100:0, an amplitude range $A = \pm 5V$ and a frequency $f_{out} = 163.659400\ Hz$. Although the x-axis mirror frequency has a theoretical value of $f_x = 163.4\ Hz$, in order to obtain successive A-Scans scanned in the exact same points of the sample, an adjustment of the f_{out} value has to be made manually and experimentally, which in this case results in a deviation of about $\Delta f \sim 0.26\ Hz$.

If the y-axis mirror is static while acquiring successive B-Scans, we expect to obtain a very similar sequence of images (considering that the sample itself undergoes no alterations). For that to happen, the N_A Sweep Triggers must fit perfectly into the x-axis waveform, in such way that all of the successive waveforms generated over time coincide with the Sweep Triggers at exactly the same instant. This way, it is assured that each Sweep Trigger will take place in the exact same scanned position of the sample over time, obtaining a result identical to the illustrated in Figure 2.22.

Correctly Adjusted Frequency
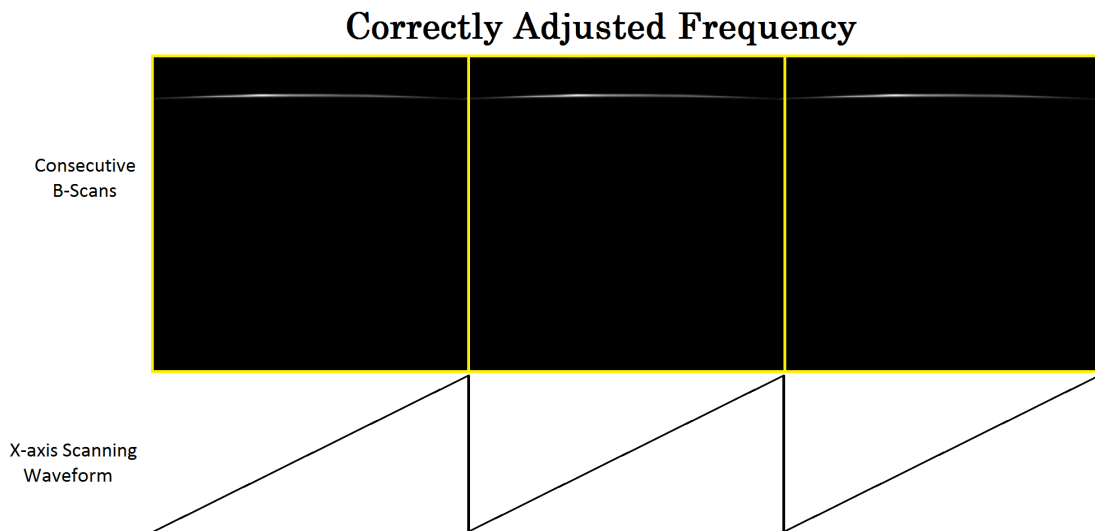
Figure 2.22: 3 sequential B-Scans in an acquisition with a correctly adjusted x-axis scanning frequency. As a result, all of the B-Scans acquired over time are identical.

On the other hand, if the x-axis scanning frequency is not in complete harmony with the Sweep Triggers, these will take place in slightly different instants over the consecutive ramp waveforms. Consequently, the acquisitions will be made in different points of the sample for each new scan. As a result, a shifting effect will occur, and each B-Scan will be different from the previous one. When viewing the successive B-Scans it looks as if they are shifting to the side at a constant speed, as represented in Figure 2.23.

Incorrectly Adjusted Frequency
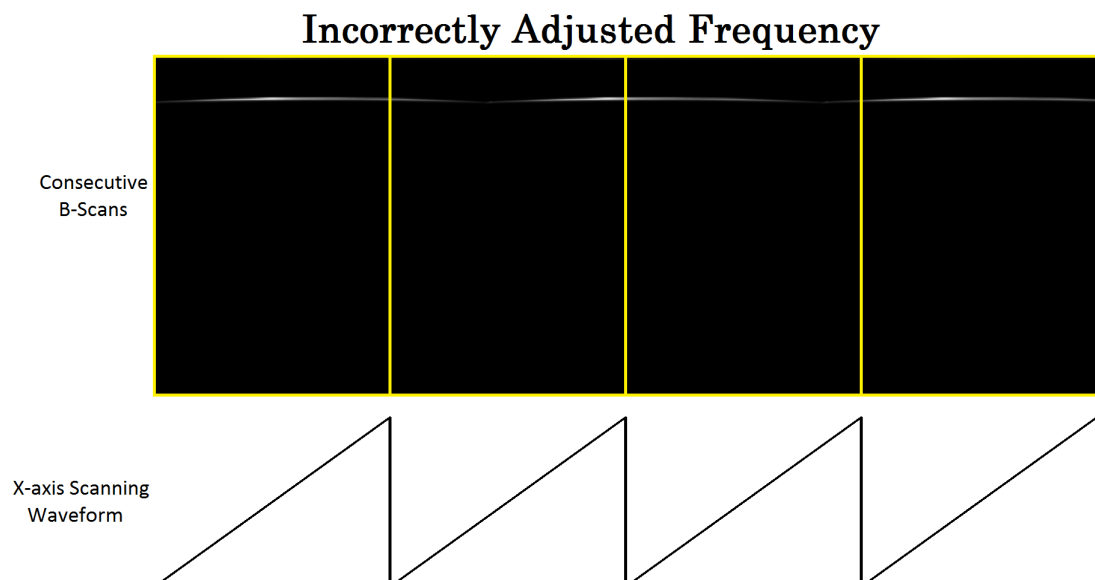
Figure 2.23: 4 sequential B-Scans in an acquisition with a incorrectly adjusted x-axis scanning frequency. The successive B-Scans show a shifting effect, as each one is different from the previously acquired one.

Therefore, for each acquisition with a certain number of A-Scans N_A per B-Scan, associated to a certain f_x, the frequency of the output signal generated f_{out} must be manually adjusted until the user verifies that the mentioned shifting effect is not present in successive B-Scans.

The fact that the AFG3101 has a memory which allows saving waveforms is quite

a handy feature, so that the user does not have to manually adjust each parameter of the output waveform every time the system is powered on or the acquisition parameters are altered, but rather simply load a previously saved one.

2.8   PCI

As already mentioned, it is convenient for the y-axis scanning to be controlled by the acquisition software, since it is aware of when an A-Scan acquisition is complete and can command the y-axis mirror to change its position immediately after. This instruction consists of altering the output voltage of an external unit which injects it to the y-axis mirror. This unit is the National Instruments' NI PCI-6010 (Figure 2.24-A), with the attached connector block NI CB-37F-LP (Figure 2.24-B). This connection is made using a 37-pin female D-SUB connector (NI SH37F-37M cable).
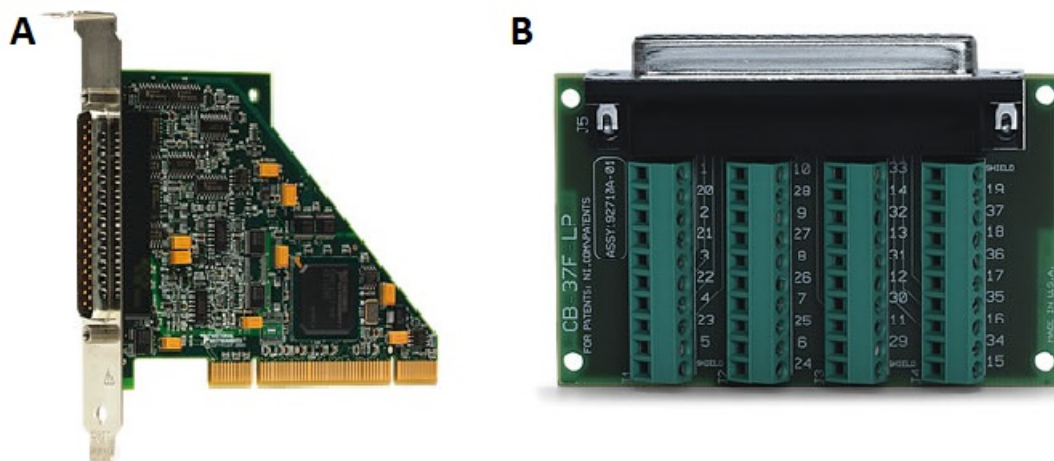
Figure 2.24: (A) NI PCI-6010. In the OCT system this unit is located inside the host PC. (B) NI CB-37F-LP connector block, which connects to the NI PCI-6010 using a 37-pin female D-SUB connector (NI SH37F-37M cable).

The CB-37F-LP terminal block is the unit the user uses to easily connect to the inputs and outputs of the PCI-6010 board, which is placed inside the host PC.

2.8.1   Specifications and Overview

The most relevant specifications to this application of the NI PCI-6010 are shown in Table 2.6.

National Instruments classifies this device as a low-cost multifunction DAQ board, incorporated with analog and digital inputs and outputs, counters and a digital trigger.

In our OCT application, only 1 analog output and 1 digital output are used. The analog one is responsible for generating the y-axis scanning waveform and the digital one for generating the above mentioned trigger signal that enables/disables the output of the Tektronix AFG3101 function generator.

Parameter	Value
Digital Output Channels	4
Analog Output Channels	2
Sampling Rate	200 KS/s
DAC Resolution	16 bits
Digital Output Range	0-5 V
Analog Output Range	$\pm$ 5 V
Analog Output Accuracy	5386 μV

Table 2.6: Technical specifications of the NI PCI-6010[40].

Although the X5-400M DAQ board also has the ability to generate analog output signals through the DAC channels, these along with the ADC channels operate synchronously governed by the same clock, which is non-linear in time. Therefore, it is not suitable for generating this desired signals.

2.8.2 Improvement of the Acquisition Time Span

It is important to mention that the use of the Tektronix AFG3101 to generate the x-axis scanning waveform is an important innovation in this OCT system, which previously used the PCI-6010 for this task as well[26] [27]. However, unlike the y-axis scanning which is shaped in steps, the x-axis one must be generated continuously, since every new sample is supposed to be different from the previous one. The only way of doing this was through a while cycle continuously generating new values in parallel with the acquisition and processing tasks, which limited the acquisition speed and demanded an enormous computational effort. It was also impossible to define an exact scanning frequency since samples are simply generated as quickly as possible after each instruction[41]. This great computational effort, affected the timing of other imperative tasks, such as data transfers, processing and display. Ultimately, this largely increased the required time to acquire a B-Scan and consequently a volume, which was no longer limited exclusively by the Sweep Triggers rate but also by the software x-axis scanning instructions. In fact, previous work reported that a volume of 512×128 would take about 25 seconds to be acquired and processed[26], when this time could be of only ~ 0.66 seconds (Equation 2.8), with an additional couple of seconds dedicated to the data processing tasks. The modification on the x-axis scanning waveform generation allowed obtaining these acquisition times, which is a major improvement in this OCT system, which now truly allows real time imaging.

3 | *Acquisition Software*

The development of the acquisition software of the OCT system is the core of this project. It is fundamentally responsible for acquiring each interference signal from the balanced detector and turn it into legible information that allows the user to have a perception of the sample's depth profile. This involves several data processing stages, which will be presented in this chapter by means of code description, flowcharts and state diagrams.

The communication between the system software and the hardware components of the OCT is restricted to the X5-400M board that digitalizes the analog signals in the output of the detector and to the PCI-6010 that controls the y-axis scanning. To support the tasks related with each of these components, they respectively feature the Malibu and the NIDAQmx software libraries. The programming language in which the software is built is C++, developed with the Microsoft integrated development environment Visual Studio.

It is important to refer that in this work the software was developed over an already existing version, documented in previous works[26][27]. As referred to in the end of the previous chapter the main practical problem of this older software version was the impossibility of performing real time imaging, because each B-Scan required too much time to be acquired. Besides overcoming this practical problem, the current version of the software also accomplished a lot of improvements in clarifying the software logic and its organization by implementing some better programing practices, which were lacking. A lot of new features and functionalities were also added, as we will see throughout this chapter.

For a clearer description of the software, its presentation will be made on a chronological order, from the moment the signal enters the DAQ system to the moment it is legible and available for the user to analyze.

3.1 State Diagram and Software Interaction

The state diagram is an useful tool to effortlessly obtain a general perception of the behavior and functioning principles of a system. The state diagram of the OCT system software is presented in Figure 3.1 and its description will now follow in tune with the respective evolution of the software window with which the user interacts.

3.1.1 ADC Configuration

When opening the executable application, the user will see the main interface window (Figure 3.2) and the system is by default waiting for the user to set the parameters for the ADC Configuration toolbox which is the only one enabled for the user to edit.
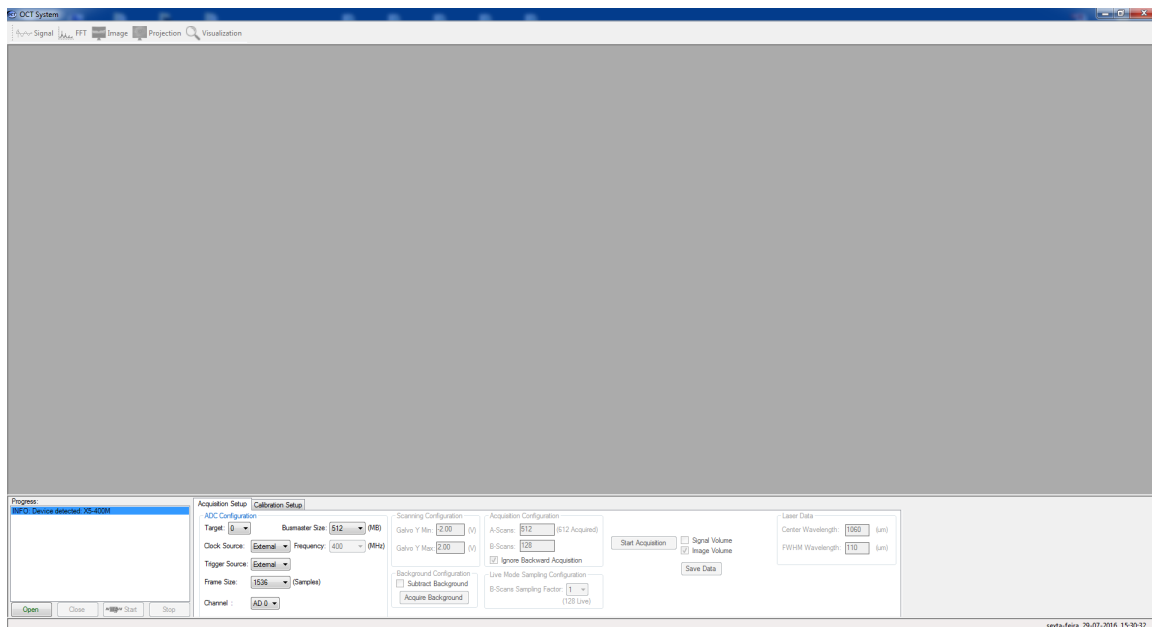
Figure 3.2: Main interface window of the OCT system software.

This corresponds to the first state represented in Figure 3.1 which is an idle state, meaning that it will not be altered until an event occurs, which in this case is clicking the Open button.

When doing so, the program will read the defined ADC Configuration toolbox (displayed in Figure 3.2) parameters. Despite being editable, the displayed default values of the parameters are the ones that the system is supposed to work with. These are:

- **Target** - Is used to identify and select the X5-400M board, seeing that each device in the system is given an unique code known as the Target ID. For instance, if there are three boards in a system, they will be targets 0,1 and 2. This index is determined by the location in the PCI bus, so the X5-400M will remain unchanged unless it is moved to a different slot or another target is installed[36]. This instruction is made in ApplicationIO::Open() (this nomenclature refers to the Open() method present in the ApplicationIO class):
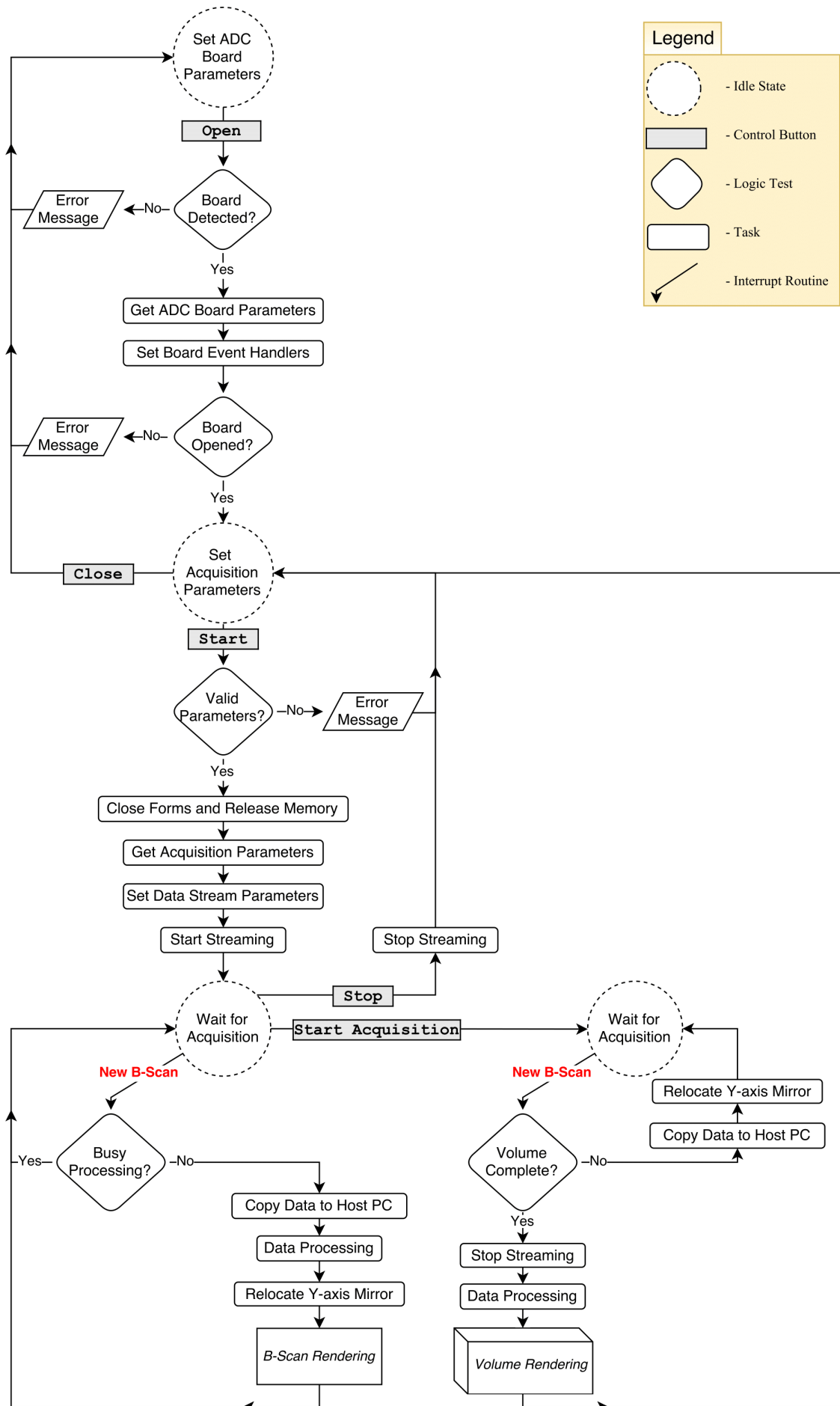
Figure 3.1: State Diagram of the OCT acquisition software.

```
// Define the board selected
Module().Target(Settings.Target);
```

The field `Settings.Target` passed as an argument holds the Target parameter value defined by the user.

- **Busmaster Size** - Sets the value of the memory that is saved for bus transfers. Larger values allow more overlap between the board and application, at the cost of a slower allocation at startup time. It must be a multiple of 4 and its value depends on the rates of bus-master transfer traffic which the board will generate[33]. Because we want to make use of the full speed capacity of the board, which will be detailed ahead, the default value is 512 MB. The code referring to this instruction is also present in the ApplicationIO::Open() method.

```
// Insure BusMasterSize is a multiple of 4 MB
const int BMSize = max(Settings.BusMasterSize/4, 1) * 4;
const int Mega = 1024 * 1024;
// Define the Incoming BMSize in bytes
Module().IncomingBusMasterSize(BMSize * Mega);
```

The field `Settings.BusMasterSize` holds the Busmaster Size value.

- **Clock Source** - The clock for this acquisition board can come from an external clock or from an onboard phase-locked loop (PLL). However, as aforementioned, this acquisition system uses an external clock provided by the light source, so the external option is meant to be chosen.

```
// Route clock to active analog devices
X5ClockIntf::IIClockSource src[] = { X5ClockIntf::csExternal,
                                     X5ClockIntf::csInternal };
Module().Clock().Source(src[Settings.ClockSource]);
```

This code is only reached after the Start button is pressed, when calling the method ApplicationIO::StartStreaming().

- **Frequency** - If the internal clock source was selected, the clock rate would be specified in the Frequency field in MHz (minimum 20 MHz and maximum 400 MHz). Because that is not the case, frequency control is meaningless and therefore is automatically disabled when the external clock option is selected.

```
// Set sample clock frequency (This is only significant on modules
// with onboard PLL)
Module().Clock().Frequency(SampleRate());
```

- **Trigger Source** - Triggers may be initiated via software or hardware, depending on the selected Trigger Source control. If the software triggers were selected (`Settings.TriggerSource = 0`), the application program would issue a command to initiate data flow. However, analogously to the clock, the trigger signal in this system is given by the light source and therefore the external trigger option (`Settings.TriggerSource = 1`) is the one set by default.

```
if (Settings.TriggerSource == 0)
    SoftwareTrigger();
else
    Module().Input().ExternalTrigger( (Settings.TriggerSource == 1) );
```

- **Frame Size** - The Frame Size is used as an auxiliary variable to determine the size of each data packet transfered from the X5-400M board to the host PC. Each data packet is set to contain a whole B-Scan as will be explained in a further section and its size is held by the variable `Settings.AnalogInPacketSize` defined in Main::System::buttonStreamStart_Click() (namespace System of the Main class) as:

```
Io->Settings.AnalogInPacketSize = Io->Settings.AScans *
                                         Io->Settings.AnalogInFrameSize;
```

The Frame Size specifies the number of collected samples (conversions made by the ADC channel) that will correspond to an A-Scan. As mentioned in 2.4.4 - FrameWork Logic, this value must be a multiple of 256, between 2 and 16777216. Attending to the 1376 samples generated by the light source, the most appropriate value to use is 1536. An error in the interpretation of the board's manual in previous works[26][27], made the previous software version only accept frame sizes that were a power of 2, so the default frame size was previously of 2048. This brought a negative impact by demanding a greater computational effort which was avoidable and decreased the imaging quality due of the nature of the inverse Fourier transform, as we will see ahead. Therefore setting the frame size to 1536 was an important correction.

This definition is made in ApplicationIO::StartStreaming():

```
//Packets scaled in units of events (samples per enabled channel)
int ActiveChannels = Module().Input().Info().Channels().
                                                ActiveChannels();
int SamplesPerWord = 4 / Module().Input().Info().Channels().
                                                BytesPerSample();
Module().Input().PacketSize((Settings.AnalogInPacketSize *
                             ActiveChannels / SamplesPerWord + 2) );
```

- **Channel** - This parameter is used to inform the software of what ADC channel (AD/0, AD/1 or both) is being used to acquired the data. This information is important because the board will output a different data packet format attending to number of channels (1 or 2) that are being used. If using only one channel the board will only regard the memory dedicated to that channel and therefore it is important to assure that the channel selected in this box corresponds to input channel that connects with the detector output.

```
// Channel Enables
Module().Input().Info().Channels().DisableAll();
Module().Input().Info().Channels().Enabled(Settings.AnalogInChannel,
                                                             true);
```

This section of the source code is also from the ApplicationIO::StartStreaming() method.

The above presented sections of the source code were developed basing on the examples presented in the Malibu library documentation[36]. Note that some of the presented line breaks are simply due to presentation and are not necessarily present in the actual source.

As suggested by Figure 3.1, after the program reads the ADC Configuration parameters and adapts the board's acquisition properties to them, the required event handlers are initialized. The stream events can be issued before the stream start (`HandleBeforeStreamStart`), after the stream start (`HandleAfterStreamStart`) or after the stream stop (`HandleAfterStreamStop`), each performing determined tasks when they are called. Another event handler initialized at this time is the `HandleDataAvailable`, which is called whenever a new packet is ready to be transfered to the PC and works as an interrupt routine to which the program always attends to, regardless of other tasks it may be dealing with. Insights on the tasks this event handler bares will be presented on a later section.

3.1.2 Acquisition and Scanning Configuration

After defining the ADC board parameters and setting the required event handlers, the software application arrives to a new idle state, in which it waits for the user to set the scanning and acquisition parameters, comprising the enabled boxes in Figure 3.3. This figure also shows the feedback information (on the left) which alerts the user with error messages if a malfunctioning of the board occurs (such as not being detected or failing to open) or with success messages otherwise.
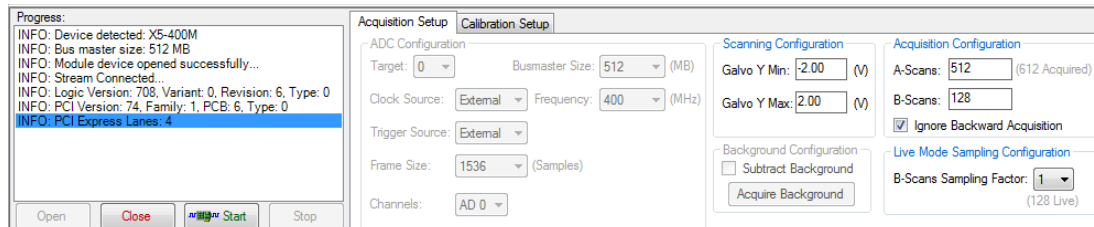
Figure 3.3: Setting up the scanning and acquisition parameters of the OCT system.

The editable parameters in this stage are the ones inside the enabled Scanning Configuration, Acquisition Configuration and Live Mode Sampling Configuration text boxes.

Acquisition Configuration

In the Acquisition Configuration toolbox the user defines the number of A-Scans and B-Scans wished to be visualized. The number of A-Scans must be adjusted in accordance with the x-axis mirror scanning (refer back to Figures 2.22 and 2.23). As previously explained, it is the scanning frequency that should be meticulously adjusted in accordance with the number of A-Scans, and not the other way around.

Additionally, a check box will determine if all of the A-Scans that acquired are meant to by visualized. If this check box is ticked, the number of visualized

A-Scans is actually not equal to the number of A-Scans acquired by the acquisition board. As aforementioned, physical limitations of the scanning mechanism impose that, after each B-Scan scanning, the mirror does not return to its initial position instantaneously, taking about 1 ms instead. The sweeping frequency of the source dictates that about 100 A-Scans will be acquired during this backward movement. Despite undesirable, this extra data acquisition is inevitable, since the conversions of the ADC channel are simply controlled by the Sweep Trigger that is continuously arriving to the board, independently of the laser scanning of the sample. That being said, it would be theoretically possible to avoid this backward scanning acquisition by suppressing the triggers precisely in the backward movement of the mirror. However, this would require a complex circuit that would demand a precise synchronization and differentiation of the scanning waveform. This circuit actually came to be developed in previous work but failed to deliver acceptable results[26]. Thus, the most reasonable and efficient way of dealing with this backward acquisition is to let it occur naturally, since the board is perfectly capable of storing this extra data. After this, because the number of A-Scans corresponding to this unwanted information is known, the data processing algorithm can simply neglect and skip the last 100 A-Scans in each acquired B-Scan. Its a much simpler way of overcoming this issue with no practical negative implications.

The information on the true number of A-Scans acquired by the board is displayed in front of the A-Scans text box and is refreshed whenever the user edits the mentioned text box or the check state of the Ignore Backwards Acquisition changes (if the number of A-Scans is not greater than 100 and the check box is ticked, this label will display "Error"). It could be useful not to ignore these 100 A-Scan in an acquisition in which no scanning is involved or if the user wants to assure that every A-Scan is consecutive, not having time gaps between some of them, reason why the user has the ability to chose if he wants this option enabled or not.

Scanning Configuration

The scanning parameters editable by means of software only refer to the y-axis mirror scanning, which is controlled by the NI PCI-6010 that features the NIDAQmx software library integrated in the OCT software. The user can determine the maximum and minimum voltage sent by the PCI-6010 DAC channel to the servo driver board of the y-axis mirror, thus defining the initial and final scanning position and consequently the scanning angle. The number of steps in the y-axis scanning waveform is equal to the number of B-Scans in the volume. Therefore, the height of each step, i.e. the voltage increment for each new position, will have a value of $V_{step} = \frac{V_{max} - V_{min}}{N_B}$. However, if only 1 B-Scan was defined in the B-Scans text box there should be no y-axis scanning. In this case only the Galvo Y Min text box is editable and the mirror position will be given by the value specified in this parameter. These tasks are done in the following method.

```
void Main::MoveGalvoY(){
  ///////////////////////// Multiple BScans /////////////////////////
  if (Io->Settings.BScans>1){
     nidaq->PositionGalvoY(GalvoYPos,nidaq->taskHandleGalvoY);
     GalvoYPos += (Io->Settings.GalvoYMax - (Io->Settings.GalvoYMin))
                                      /(Io->Settings.BScans);
     NumBScan++;
```

```
    if (NumBScan == Io->Settings.BScans){
      NumBScan = 0;
      GalvoYPos = Io->Settings.GalvoYMin;
      }
  }
////////////////////////// 1 BScan //////////////////////////
else{
    if (float::TryParse(textBoxGalvoYMin->Text, GalvoYPos))
      nidaq->PositionGalvoY(GalvoYPos,nidaq->taskHandleGalvoY);
  }
}
```

The `PositionGalvoY()` function is defined in class NIDAQ:

```
void NIDAQ::PositionGalvoY(float64 position, TaskHandle taskhandle){
  DAQmxWriteAnalogScalarF64(taskhandle, true, 1.0, position, NULL);
  }
```

The `DAQmxWriteAnalogScalarF64()` function writes a 64-bit floating point sample (`position`) to the analog output channel specified in the definition of `taskHandleGalvoY`. The function input with `true` value indicates that the function starts the task automatically, while the `1.0` parameter sets the maximum waiting time in seconds for the function to write the value. If this timeout elapses the function returns an error. The `NULL` parameter is meaningless and passed as a requirement of this function.

Live Mode Sampling Configuration

This new developed feature allows the user to chose a subsampling factor of 1 , 2 , 4 or 8. This factor passed to the variable `LiveSamplingFactor` refers to the number of B-Scans that are being visualized in real time. Before starting the data stream, the variable that memorizes the number of B-Scans selected by the user is updated according to the follwing instruction.

```
Settings.BScans = Settings.BScans/LiveSamplingFactor;
```

The reason for having this subsampling factor is attached to different performance priorities when imaging in live mode and when acquiring data in acquisition mode. These two modalities will be subsequently explained, but by now we can distinguish them by asserting that in live mode volumes are continuously being acquired and B-Scans as well as projection images can continuously be displayed to the user in real time (or as close to it as possible). However, because a certain amount of computation time is required to process and render data, this means that the B-Scans being visualized are not acquired by consecutive triggers. On the other hand, when the system is functioning in acquisition mode, all the tasks related with processing and rendering are suppressed and the system is only waiting for the specified volume to be acquired. This allows a much faster acquisition, although the user cannot see the acquisitions in real time, but rather only after the entire volume is acquired.

Therefore, when visualizing the sample in live mode, it is often preferable to compromise the resolution (in this case vertical resolution) of a projection image

in favor of a greater imaging speed, so that the projection image does not take so long to refresh. Note that only the projection image suffers this resolution decrease, since less B-Scan are being acquired and consequently there is a greater space gap between them as the sample is vertically swept.

When visualizing in live mode, the subsampled projection image is exactly the same that it would be displayed if no subsampling occurred but the initially defined number of B-Scans was set to be the division of the number of B-Scans by the subsampling factor. When acquiring data in acquisition mode, this subsampling factor is ignored (i.e. set to 1) and the number of B-Scans defined in the respective text box will be acquired.

The text label below the combo box informs the user of the number of B-Scans that will be visualized in live mode, and is updated whenever a different subsampling factor is selected or the number of B-Scans in the respective text box is altered.

3.1.3   Live Mode Imaging

One important alteration on the previous software version was the implementation of two distinct acquisition modes: the live mode imaging and the acquisition mode. We will begin by presenting the first.

Once the scanning and acquisition parameters are defined, the user can click the Start button to begin the data stream. When doing so, if the defined parameters are valid, some tasks are performed before the streaming can start. Firstly, all running tasks related to data processing or rendering are terminated and the memory reserved for these tasks is cleared. This is vital to assure that even if the user repetitively starts and stops the data stream (using the Start and Stop buttons), every new stream start is not affected by eventual previous ones. If this memory reset was neglected, new data streams would progressively keep reserving more memory in the PC, which would affect the computation speed. After this, the parameters are passed as variables to the acquisition software and the board's data stream parameters are defined, namely the packet size.

The data stream can then begin and the main interface window is updated, disabling the scanning and acquisition parameters and enabling the Background Configuration tool box (which will be detailed ahead) and the Start Acquisition button (Figure 3.4). In the bottom of this figure we can also see a status bar, that informs the user of how many packets, i. e. B-Scans, were transfered to the PC since the beginning of the stream, as well as the reception rate, i.e. the average packet size acquired per second. It also provides information on the temperature monitoring of the X5-400M which is used to prevent overheating, being an alert sent if it exceeds 85 (maximum safe operating temperature[33]) and finally indicates the index of the last acquired B-Scan of the volume. This status bar was defined to be updated periodically, every 0.1 seconds.
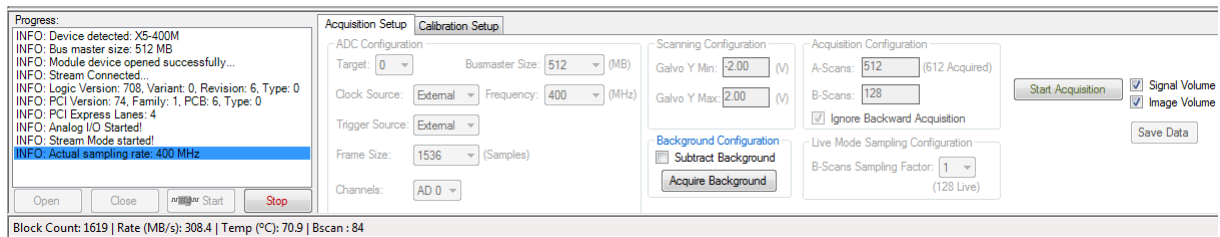
Figure 3.4: Presentation of the user interface window while imaging in live mode.

By clicking the Start button, the method responsible for generating the burst trigger used to enable/disable the output of the signal generator that controls the x-axis mirror, is also called:

```
void NIDAQ::DigitalSignalOut(bool state){
   if(!state)
      data = 0x00000000;
   else if(state)
      data = 0xffffffff;
   DAQmxWriteDigitalU32(DOTaskHandle, 1, 1, 10, DAQmx_Val_GroupByChannel,
                                              &data, &written, NULL);

   }
```

This method is called from the Main class and passes the boolean argument `state` as true. As a result the associated DAC channel of the NI PCI-6010 will output a 5V TTL signal which will enable the start of the x-axis mirror scanning.

As suggested by the state diagram in Figure 3.1, the software now enters a new idle state, which corresponds to the first stage of live mode imaging. The software can only leave the live mode imaging in two ways: either by clicking the Stop button, which stops the data stream and sends the application back to setting the scanning and acquisition parameters, or by clicking the Start Acquisition button which will initiate the acquisition mode.

On this idle state, the program is simply waiting for the acquisition board to alert that a new packet is ready to be transfered. This alert consists of the interrupt routine `HandleDataAvailable` that will be later presented. As aforementioned, the application always attends to this interrupt method. However, that does not imply that the packet is transfered to the PC every time this method is called. As can be seen by the state diagram in Figure 3.1, when this interruption routine occurs the program immediately checks if it is ready to receive a new data packet or if it is still busy processing the previously transfered one. In the second case, the program simply returns to the waiting state as the processing tasks proceed. If every incoming packet was transfered, the time delay between the visualized and the acquired data would be increasing with every new packet to a limit in which data would no longer be displayed in real time, but rather displaying data acquired a considerable amount of seconds ago.

If the system is ready for a new packet it is transfered, the instruction to begin the processing of the packet is given and the y-axis mirror is relocated to the new scanning position, so that the follwing acquired B-Scan will be scanned in the proper segment of the sample. Only after the current packet processing is finished will the system be able to receive a new one. Simultaneously to this authorization the data is displayed, which can be done in different ways according to the method chosen by the user as we will see ahead.

3.1.4   Acquisition Mode

The software goes in acquisition mode by clicking the Start Acquisition button (on Figure 3.4) during live mode imaging. As suggested by the state diagram in Figure 3.1, this action makes the program enter a new idle state in which is waiting for the interruption routine to signalize that a new packet is ready, similarly to the idle state in live mode imaging. However, the aim of this acquisition modality is to acquire the defined volume of the sample as quickly as possible. For this reason, the priority is to first acquire every packet consecutively and only after this acquisition is complete will the system perform the processing and rendering tasks. This high speed acquisition is fundamental when imaging living samples, since it is often very difficult to position the sample perfectly still (at a micrometer level) for several seconds. On acquisition mode, the time it takes to acquire a packet is simply defined by the sweep frequency (recall Equation 2.8). When the processing tasks take place there is no need for the sample to remain static or even present, since all the needed data was already acquired. Therefore it is harmless for this processing to take several seconds. The waiting time from the moment data is finished acquiring to when it is displayed to the user depends mostly on the size of the acquired volume, but also on the complexity of the processing tasks (e.g. background subtraction, logarithmic representation, or others that will be later addressed). But for the most complex and therefore time consuming case the mentioned elapsed time for a volume of 512×512 (which is considered a very large volume, that not all commercial OCT systems are capable of acquiring) is less than 18 seconds. For inferior volumes such as 512×256, which is also considered a large volume, this time is inferior to 9 seconds. Note that this computation time depends on the specifications of the PC used as host.

When the acquisition is over, the program returns to the idle state of setting the acquisition and scanning parameters. However, it is now also enabled the visualization of the volume (B-Scans and projection image) as well as saving each of the raw and the processed interference signals (A-Scans). Both of these options will be revisited in a further section.

3.2   Data Acquisition

An overview of the software logic, processes and stages was given so far in this chapter. From now on, we will detail these stages by making a more thorough analyses and description in a chronological order, according to the presented state diagram. Thus, we will start by the data acquisition process.

3.2.1   Stream Packet Format

In order to properly extract and decode the acquired data from the board, it is necessary to know how it is organized in the packet that is transfered to the PC.

Packet streams contain a variable number of sub-packets each consisting of a header field followed by a data field. The header filed contains 2 32-bit words with information about the subsequent data field. The data field contains the produced data in a collection of samples, which are 14-bits signed extended into a 16-bit field (two bytes/sample). That is, the X5-400M produces C-style short, 16-bit data words within the data field[42].

The length of the data field, i.e. the number of generated data words depends on the frame size defined by the user and on the number of enabled ADC channels. If the 2 ADC channels were enabled in the acquisition, each 32-bit data word would contain 2 16-bit samples, each corresponding to a different channel. Therefore, if each of the 2 enabled channels were acquiring N samples from 2 signals (or the same one), N data words would be generated.

On the other hand, if only one channel is enabled, as in our application, each 32-bit data word is composed by 2 consecutive 16-bit samples from the selected ADC channel. Therefore, if the software establishes an acquisition of N samples, only $N/2$ data words will be generated, since each 32-bit data word has the capacity to store 2 16-bit samples. In this case, the data field format is as follows:

Data Word 0	- bits 0-16 : Sample 1
	- bits 17-31: Sample 0
Data Word 1	- bits 0-16 : Sample 3
	- bits 17-31: Sample 2
	...
Data Word N/2-1	- bits 0-16 : Sample N-1
	- bits 17-31: Sample N-2

Figure 3.5 illustrates the described organization of the data field.

Data Word 0 (32-bit)		Data Word 1 (32-bit)		Data Word 2 (32-bit)			Data Word N/2-1 (32-bit)	
Sample 0 (16-bit)	Sample 1 (16-bit)	Sample 3 (16-bit)	Sample 2 (16-bit)	Sample 6 (16-bit)	Sample 5 (16-bit)	...	Sample N-1 (16-bit)	Sample N-2 (16-bit)
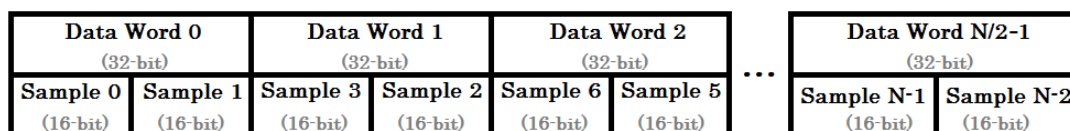
Figure 3.5: Data field format in each acquired sub-packet.

As for the information contained in the header field, it is organized in the follwing way:

Header Word 0	-bits 0-23 : Header + Data size (in 32-bit words units).
	-bits 24-31: ID of the peripheral which sourced the data.
Header Word 1	-All bits 0.

The ID field in header word 0 identifies the source of the data. For instance, ID 0 corresponds to A/D data sent from the card to the Host while ID 2 corresponds to D/A which is generated by the Host software and sent to the card. Word 1 is reserved for application-specific purposes, but is typically initialized to zero in stock factory logic[42].

Having clarified the format of a sub-packet in the streamed packet, its overall scheme is illustrated in Figure 3.6.
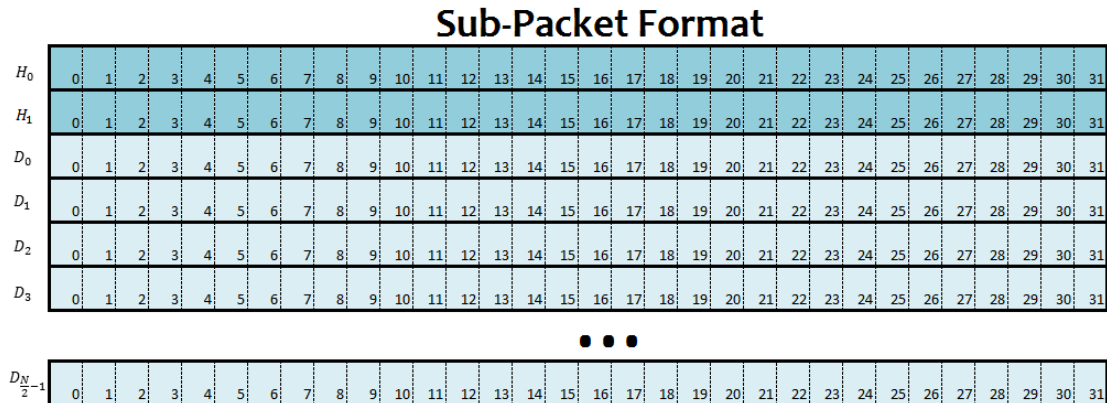
Figure 3.6: Format of the sub-packets in the packet stream. Each horizontal line represents a 32-bit word, while each numbered square inside it identifies a single bit. H - Header Word; D - Data Word (32-bit).

Now that the packet format has been detailed, it is only left to specify what corresponds to a packet, a sub-packet and a sample in our specific OCT application. Each packet transfered from the board to the PC will contain the information of 1 complete B-Scan, each sub-packet that composes it corresponds to 1 A-Scan and each 16-bit data sample corresponds to a sample of the A-Scan. Considering an acquisition frame size of $N = 1536$ samples, this means that $N/2 = 768$ 32-bit data words will be acquired in each A-Scan. According to this, we can determinate the size of each acquired A-Scan and consequently the size of a packet containing N_A A-Scans, which is of:

$$1 \text{ Sample} \quad \longmapsto \quad \frac{32 \; bit}{2} \; = \; 16 \; bit = \; 2 \text{ Bytes}$$

$$1 \text{ A-Scan} \quad \longmapsto (2 \text{ Bytes}) \times 1536 = 3072 \text{ Bytes}$$
$$1 \text{ Sub-Packet} \longmapsto (2 \times 4 \text{ Bytes}) + (3072 \text{ Bytes}) = 3080 \text{ Bytes}$$

$$1 \text{ B-Scan} \quad \longmapsto (3072 \text{ Bytes}) \times N_A = 3072 N_A \text{ Bytes}$$
$$1 \text{ Packet} \quad \longmapsto (3080 \text{ Bytes}) \times N_A = 3080 N_A \text{ Bytes}$$

Note that to the size of each sub-packet 2 32-bit header words (2×4 Bytes) must be added, which is consequently reflected in the size of the total packet.

To illustrate a practical example, the acquisition of a B-Scan with 612 A-Scans (512 visualized + 100 neglected corresponding to the backwards movement of the x-axis mirror), which is a very typical resolution, would be contained in a 1.88496 MB packet size.

3.2.2 Data Storage In Memory

Once the streaming is enabled and the module is triggered, data flow will commence. Samples will be accumulated into the onboard FIFO, before being bus-mastered to the host PC into driver-allocated memory[36].

According to the board's specifications, the DDR2 DRAM has a storage capacity of 512 MB. However, the standard firmware statically allocates a quarter of this memory to each of the 4 analog I/O channels on the card[34]. Therefore we are left with a total usable memory of 128 MB. Using this information and the fact that each packet has a size of $3080N_A$ Bytes, we can determine the maximum number of A-Scans that can be contained in the onboard memory, yielding:

$$N_{A_{\max}} = \frac{128 \text{ MB}}{3080 \times 10^{-6} \text{ MB}} = 41\ 588 \text{ A-Scans}$$

A B-Scan image composed by 1024 A-Scans is already considered a high resolution image, and this number is tiny when compared to the calculated $N_{A_{\max}}$. Therefore, we can be secure that the onboard memory is more that sufficient for the goals of our application, as long as the packet streams are properly handled to ensure that packets are being transfered to the PC at a higher rate than they are being acquired to the onboard memory. Otherwise, this memory would be gradually filling over time and eventually new packets would be lost. We will calculate and discuss this rates in detail later.

If the onboard memory fills and the trigger and clock that govern the data acquisition continue to arrive, the new incoming samples are discarded, rather than being written over previous data. When this condition occurs, if the overrun alert is enabled, an alert will be added to the PCIe stream signifying the condition[34].

Finally, we can calculate the theoretical rate at which data is being acquired. Knowing that a sub-packet with 3080 Bytes is the result of 1 A-Scan acquisition, and that these A-Scans arrive to the board at frequency f_{sweep}, we determine the acquisition rate to be of:

$$\text{Acquisition Rate} = 3080 \text{ Bytes} \times 100\ 000\ Hz = 308 \text{ MB/s}$$

Note that this rate is applicable for both acquisition mode and live imaging. Although in live mode most B-Scans are discarded to allow real time imaging, this only happens after being acquired and stored to the onboard memory, since as aforementioned this only depends on the trigger and clock signals and thereby cannot be prevented. The yielded value is, as expected, very close to the obtained in the real example illustrated in the status bar on the bottom of Figure 3.4 (Rate = 308.4 MB/s). The value displayed on the status bar is calculated exclusively by a Malibu function that keeps track of the amount of data that is being acquired and the time elapsed since the beginning of the stream.

3.2.3 Data Transfers

Upon receipt of a packet, Malibu signals the Stream.OnDataAvailable event, which was initialized to attach the method ApplicationIO::HandleDataAvailable().

By hooking this event which is signaled from within a background thread, the software can perform the processing tasks on each acquired packet[36].

```cpp
void ApplicationIO::HandleDataAvailable(PacketStreamDataEvent & Event){

  Buffer Packet;
  Event.Sender->Recv(Packet); //Extract the packet from the Incoming Queue

  if(ReadyForNewPacket){
    IntegerDG Packet_DG(Packet);

    if(!AcquisitionMode){ // Live Mode
      ReadyForNewPacket = false;
      IppCopyInt32Buffer(&Packet_DG[0], &LiveData[0],
                                      Settings.AnalogInPacketSize/2);
      UI->DataProcessing();
      UI->MoveGalvoY();
      }

    else if(AcquisitionMode){ // Acquisition Mode

        if(NumBScan < Settings.BScans-1){
          IppCopyInt32Buffer(&Packet_DG[0],
              &AcquisitionData[NumBScan*Settings.AnalogInPacketSize/2],
              Settings.AnalogInPacketSize/2);
          UI->MoveGalvoY();
          }
        else { // Finish Acquisition
          IppCopyInt32Buffer(&Packet_DG[0],
              &AcquisitionData[NumBScan*Settings.AnalogInPacketSize/2],
              Settings.AnalogInPacketSize/2);
          Stream.Stop();
          UI->DataProcessing();
          }
      }
    TallyBlock(Packet_DG.SizeInBytes());
    }
  }
```

When the event is signaled, the data buffer must always be copied from the board's bus-master pool into the application buffer, which is done by the instruction `Event.Sender->Recv(Packet)`. This is necessary to free the samples from the onboard FIFO memory[36], even if the packet will end up being discarded. The incoming packets are copied into the local Buffer called Packet. Since data sent from the hardware can be of arbitrary type (integers, floats, or even a mix, depending on the board and the source), Buffer objects have no assumed data type and have no functions to access data in them. Instead, a second class called a datagram wraps the buffer, providing specialized access to the data in the buffer[36]. In this application, the IntegerDG class is used, which provides access to the data in the packet as if it was an array of 32-bit integers[27].

As can be seen in the ApplicationIO::HandleDataAvailable() method above, when a new packet is ready for processing two boolean variables control the flow of tasks the software will perform. Firstly, the boolean `ReadyForNewPacket` signalizes

if the system is ready to receive a new packet or if it is still occupied processing a previously acquired B-Scan. If this first logical test returns true, a second one follows as the boolean `AcquisitionMode` verifies whether the system is performing live mode imaging or if it is in acquisition mode. The software tasks that follow depend on the result of this second logical test, and will be described subsequently.

As each packet is received, the `TallyBlock()` function is also called. This routine calculates the data flow rate and reports it through the status bar in the user interface[36].

Live Mode

If the system is in live mode and available for new processing tasks, the boolean `ReadyForNewPacket` switches its value to false when a new packet is transfered, so that the program acknowledges that a new processing task is occurring. The packet is transfered from the application buffer to the PC memory on call of the Malibu function `IppCopyInt32Buffer()`, which copies an array of 32-bit integers from the memory address given by the pointer passed as the first argument (`&Packet_DG[0]`), to the memory address given by the pointer passed as the second argument (`&LiveData[0]`). Since these pointers only point to the first index of each respective memory, it is also necessary to give information on how many values in the array will be copied, provided by the third argument (`Settings.AnalogInPacketSize/2`). The `Settings.AnalogInPacketSize` variable represents the number of samples in the data field of the packet, i.e. the multiplication of the number of defined A-Scans by the Frame Size of each one. Thus, it is expressed in units of 16-bit samples. Since the packet is copied as an array of 32-bit integers, this packet size must be divided by a factor of 2 to properly indicate the extent of the array.

After the data is copied to the PC memory the `DataProcessing()` method instructs the beginning of the processing tasks and the `MoveGalvo()` method relocates the y-axis mirror to the next scanning position.

The timing of the sample scanning, data acquisition, data transfers, and software tasks is summed up in Figure 3.7 for the case of live mode imaging. This is merely an illustrative scheme, so the suggested number of A-Scans per B-Scan is obviously much inferior to the one typically used.
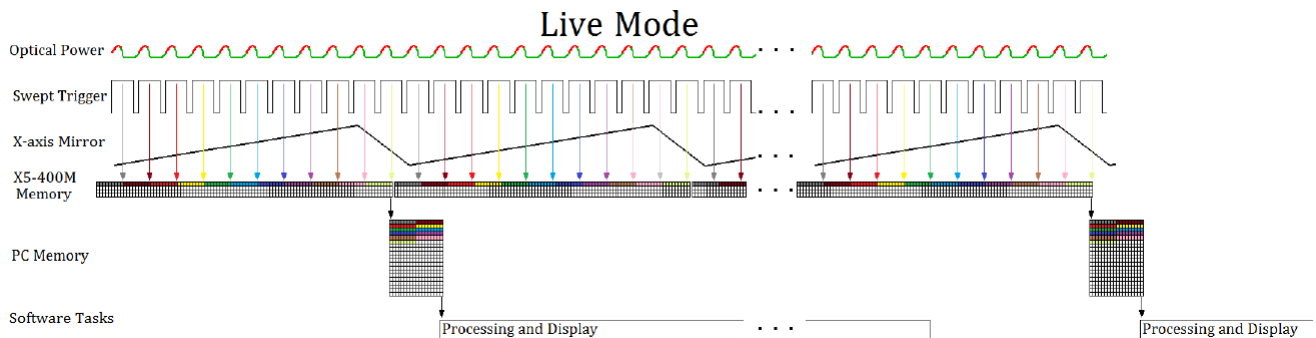
Figure 3.7: Timing of the sample scanning, data acquisition, data transfers, and software tasks in live mode imaging.

Acquisition Mode

If the system is in acquisition mode, the `ReadyForNewPacket` boolean will always remain true until the acquisition is over. The progress of the acquisition is marked by the counter `NumBScan` which for convenience is incremented in the `MoveGalvo()` method, whose code was also already exposed.

Although the system is operating in acquisition mode, the packet size continues to be the equivalent of 1 B-Scan acquisition, rather than the whole volume. This means that, as the volume is being acquired, the software will receive each B-Scan in a new call of the `HandleDataAvailable()`, instead of firstly acquiring the entire volume and only after copying it at once to the PC memory. This brings the advantage of being able to acquire a greater volume than the one the onboard memory could store. As previously determined, attending to the A-Scan size after being acquired the maximum number of A-Scans that can be held by the onboard memory is 41 588. If imaging at the typical value of 612 A-Scans (512 visualized + 100 neglected due to the backwards scanning) that would mean that the maximum volume that could be acquired would be of 67 B-Scans. This is a rather small volume, and a projected image of this volume would be significantly limited in its the vertical resolution.

Therefore, copying B-Scans as they are being acquired is a more favorable solution. However, since the packets are periodically released from the onboard memory, it is important to ensure that this frequency is greater than the one at which new packets are being stored in it. Otherwise the occupied memory would progressively increase and eventually would fill, being no longer able to acquire new data.

Both these rates can be predicted. To begin with, the rate at which packets are acquired is exclusively dependent on the sweep frequency $f_{\text{sweep}} = 100 \ KHz$. Therefore, the elapsed time when acquiring a packet with N_A A-Scans is:

$$t_{acquisition} = \frac{N_A}{f_{\text{sweep}}} = 10N_A \ \mu s$$

According to the boards specifications, the PCI Express provides 1000 MB/s sustained transfer rates to host memory[33]. Knowing that each packet has a size of $3080N_A$ Bytes, the time required to copy it to the PC memory is of:

$$t_{copy} = \frac{3080N_A \text{ Bytes}}{10^9 \text{ Bytes} \cdot s^{-1}} = 3.080N_A \ \mu s$$

Since $t_{copy} < t_{acquisition}$, and by a considerable factor, we can rest assure that the onboard data memory will never fill. Therefore, the maximum volume size that can be acquired by this OCT system is simply held back by the inconvenient of an excessive volume requiring a great time duration to be processed, displayed and saved.

When all of the expected data finishes being acquired and transfered to the PC, the data stream is immediately stopped (`Stream.Stop()` instruction) so that the program can focus only on the processing tasks. Similarly to what happened when pressing the Start button, by pressing the Stop button during live mode or when the acquisition mode is finished the burst trigger sent from the NI PCI-6010 to the signal generator returns to 0 by calling the same method, ceasing the scanning of the sample.

The timing of the sample scanning, data acquisition, data transfers, and software tasks is summarized in Figure 3.8 for the software working in acquisition mode.
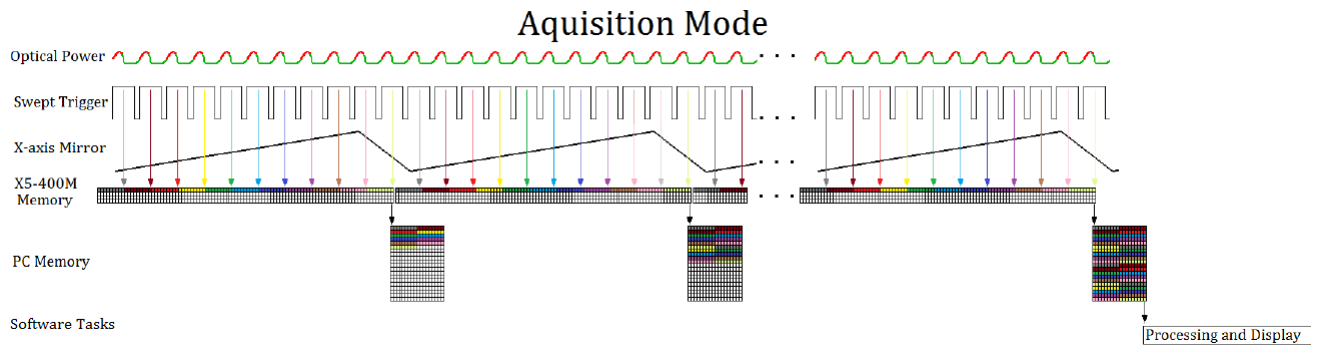
Figure 3.8: Timing of the sample scanning, data acquisition, data transfers, and software tasks in acquisition mode.

3.3 Data Processing

All data processing is done in the method `doProcessing()` of the ProcessingData class. This was a significant alteration from the previous version of the software, which processed each A-scan in the class correspondent to the selected visualization mode. As we will see ahead, data can be visualized in distinctive ways simultaneously, and each one of these visualization options is associated to a separate class. In the older software version, the same packet could be processed simultaneously in several places, performing the same tasks repetitively. The software organization was altered and all of the processing tasks are now done in the mentioned method, and if needed the required data will be transfered to the method in charge if displaying the information as selected by the user.

We can identity 3 stages of processing tasks on a packet, which will now be addressed in proper order.

3.3.1 2's Complement Decoding and Zero Padding

As previously said, the acquisition board outputs data in 2's complement, which is a classic format to represent signed integers. The first processing tasks consists on splitting these 32-bit integers, each corresponding to a 32-bit data word, into the two correspondent samples. Note that despite 32 bits being used for each data word, samples are actually 14-bit signed extended to 16-bit. This means that the 2 MSB's of each sample contain no useful information and are simply set to 0.

Since the ADC has a resolution of 14 bits and accepts an input range of ± 1 V (Table 2.3), positive and negative voltage values can be acquired, which is why samples are 14-bit signed. This means that in each sample the MSB (bit 13, since the first bit is counted as 0) holds the information on the sign of the sample, i.e. if the digitized value corresponds to a positive or a negative voltage: if bit $13 = 0$ the integer is equal or greater than zero, and if bit $13 = 1$ the integer is less than zero. Accounting for this sign bit, 13 bits are left to reproduce the magnitude of the acquired signal. Therefore this magnitude will be in the range $[0, 2^{13} - 1] = [0, 8191]$.

Therefore, although each 32-bit data word is red as an integer, the desired information is not simply its value but rather the information contained in its bits, which needs to be decoded.

Taking into account the above considerations, the processing of each sub-packet

(A-Scan) in a packet is made according to the following code:

```
for(int iW = 0; iW < Frames; iW++){ //Iterate the 32-bit Words
   if(iW < ZeroPadding){

      if (!AcquisitionMode)
         Word32 = (int)LiveData[iA*Frames+iW];
      else if (AcquisitionMode)
         Word32 = (int)AcquisitionData[iB*AScans*Frames+iA*Frames+iW];

      ///////////// Sample from LSBs /////////////
      if ( (Word32 & 0x00002000) != 0)// 14th LSB = 1 (Negative Sample)
         DataSignal[4*iW] = (float)(Word32 & 0x00001FFF);
      else                             // 14th LSB = 0 (Positive Sample)
         DataSignal[4*iW] = (float)((Word32 & 0x00001FFF)+0x00001FFF);

      ///////////// Sample from MSBs /////////////
      if ( (Word32 & 0x20000000) != 0)// 14th MSB = 1 (Negative Sample)
         DataSignal[4*iW + 2] = (float)((Word32 & 0x1FFF0000) >> 16);
      else                             // 14th MSB = 0 (Positive Sample)
         DataSignal[4*iW + 2] = (float)(((Word32 & 0x1FFF0000) >> 16)
                                                      + 0x00001FFF);
      DataSignal[4*iW + 1] = 0; // Add imaginary part
      DataSignal[4*iW + 3] = 0; // Add imaginary part
      }

      ///////////// Zero Padding /////////////
   else{
      DataSignal[4*iW] = 8191;      // Zero Padd from sample 1376 on
      DataSignal[4*iW + 2] = 8191;  // Zero Padd from sample 1376 on
      DataSignal[4*iW + 1] = 0;  // Add corresponding imaginary part
      DataSignal[4*iW + 3] = 0;  // Add corresponding imaginary part
      }
```

The presented code uses hexadecimal notification on the bitwise operations for simplicity. To expose this processing algorithm in a simpler way, lets consider its schematic illustration in Figure 3.9.

The samples generated will be stored in the array `DataSignal`. In its initialization it was set to contain a total of FrameSize $\times$ 2 = 1536 $\times$ 2 = 3072 values. The reason for this factor of 2 is related to the need of each sample having a real and imaginary part due to the requirements of the FFT algorithm, as we will see ahead. As we are not interested in the imaginary component, all odd indexes of the `DataSignal` which correspond to it are simply equaled to zero. However, because the range of values passed to the `DataSignal` array the will be shifted for convenience, as will be ahead detailed, the zero value will actually correspond to 8191.

As we can see, whenever a new A-Scan is being processed it is firstly verified if the current frame, i.e. sample of the A-Scan, being analyzed corresponds to one of the 1376 generated by the source on the laser sweeping phase. If not, this acquired frame will not contain reliable information and will be neglected. For this reason, every frame exceeding the mentioned index will not be red and the `DataSignal` will simply be filled with zeros, which corresponds to the zero padding procedure.

Otherwise, if the acquired frame contains useful information, the frame value is passed to the variable `Word32` as an integer, red either from the `LiveData` or the
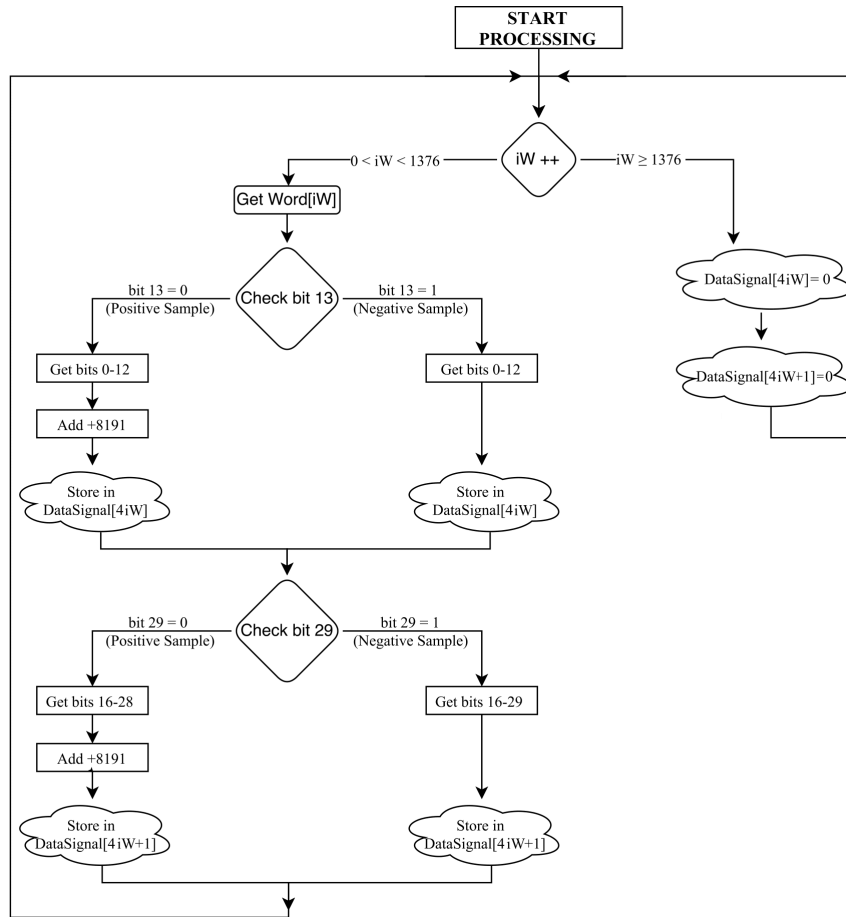
Figure 3.9: Flowchart of the sequence of instructions needed to process each sub-packet iW contained in packet.

`AcquisitionData`, according to the acquisition mode the system is operating in. The 2's complement decoding algorithm is then applied. The sample contained in the 16 LSB's (only on bits 0-13) is analyzed first.

Since the produced integers can be either negative or positive, their true range is $[-8191, 8191]$, which corresponds to a total of $16383 = 2^{14} - 1$ possible values, being in concordance with the 14 bits used for the conversion. However, all integers produced will have a value between $[0, 8191]$, since the sign information is in charge of another bit. It is convenient to shift the mentioned range so that all values are positive, i.e $[-8191, 8191] \rightarrow [0, 16383]$. This way, we can distinguish the negative integers, contained in $[0, 8191]$, from the positive ones which will be between $[8192, 16383]$. To do this, whenever a positive sample is processed, an extra instruction of adding 8191 is given to make this range shift, while the negative samples will already naturally emerge in the desired range. The obtained integer now corresponds to the proper digitized value and is passed to the correspondent index of the `DataSignal` array.

The same procedure is implemented in the sample contained in the 16 MSB's of `Word32`. In this case, to get the bits 16-28 we need to shift them 16 bits to the right, so that the integer is contained in the 14 LSB's to be properly stored in the correspondent index of the `DataSignal`.

The described algorithm is repeated until all the words are processed and the zero padding fills the rest of the `DataSignal` array. After this, the interferometric spectrum of 1 A-Scan becomes available. To process a B-Scan this code is iterated by

the `iA` variable according to the specified number of A-Scans meant to be visualized (the ignored ones due to the backward scanning are not processed). In acquisition mode, an entire volume must be processed and therefore the variable `iB` controls the iterations along the successive B-Scans.

3.3.2 Inverse Fourier Transform

As mentioned in the theoretical exposition of a Fourier domain OCT system, each A-Scan acquired will be in frequency domain and needs to be transposed to the time domain so that the reflectivity profile of the sample can be visualized. This transposition is made by applying the inverse Fourier transform. Since we are dealing with a digitized and therefore discrete signal, the transform that should be applied is the inverse discrete Fourier transform (IDFT). When computing either the IDFT or the direct discrete Fourier Transform (DFT), implementation algorithms are used to reduce the mathematical operations by exploiting the properties and symmetries of matrix multiplications. These algorithms allow a computationally efficient way of performing the DFT and the IDFT and are therefore designated as fast Fourier transform (FFT) and inverse fast Fourier transform (IFFT), respectively.

In practical terms, since we are dealing with real signals, the same results can be achieved by applying a FFT or an IFFT, as can be concluded by analyzing the equations that define their correspondent transforms. If we consider a sequence of N complex numbers x_n and the correspondent frequency domain sequence X_k, also by composed by N complex numbers, their DFT and IDFT are given by the equations:

$$x_n \xrightarrow{DFT} X_k = \sum_{n=0}^{N-1} x_n \ e^{-i\left(\frac{2\pi k n}{N}\right)} \ , \qquad k \ \in \ \mathbb{Z} \tag{3.1}$$

$$X_k \xrightarrow{IDFT} x_n = \frac{1}{N} \sum_{k=0}^{N-1} X_k \ e^{i\left(\frac{2\pi k n}{N}\right)} \ , \qquad n \ \in \ \mathbb{Z} \tag{3.2}$$

Attending to this, it is the FFT that is applied in our application, instead of the IFFT. This is for mere convenience, because the function used to perform the FFT already outputs the wished amplitude of each value, while if using the IFFT function the output would be the set of real and imaginary parts of each value, implying the need for an extra processing step to calculate the amplitude.

That being clarified, we will now present the code related to this operation. Firstly the FFT object of the `Fourier` namespace of the Malibu library is created and initialized as follows:

```
FFT = new Fourier;
FFT->Samples(FFTFrameSize*2);
FFT->SpectrumEnabled(true);
FFT->Window(Innovative::wtHanning);
FFT->IgnoreDC(true);
```

The number of samples contained in the FFT transform is first defined. This number would ideally be of 1376, the samples that are swept by the laser source. However, a limitation on this number of samples is imposed by the FFT transform function, which specifies that the size of the FFT, in samples, must be an even

power of $2^{[43]}$. This means that when passing 1376 samples to the function, it will truncate values after the inferior closest power of 2, which in this case will be of 1024. That being said, the number of samples in the FFT will be of `FFTFrameSize` $\times 2 = 512 \times 2 = 1024$.

In practice, since not all of the 1376 samples are used in the transform, but only the 1024 first ones, the potential imaging depth is decreased, since the highest frequencies of the laser bandwidth are not reached. However it is possible to overcome this limitation, although not necessarily recommended in every situation. That is to simply select in the ADC Configuration toolbox a frame size of 2048 instead. This way, 2048 samples are passed to the FFT function: the 1376 relevant samples + 672 zero padded samples. But by doing so the zero padding presence in the signal is quite significant, corresponding to about a third of it, adding a considerable amount of extra frequency components. As a consequence, a substantial spectral leakage effect is present after performing the FFT, which broadens the peaks of the FFT and consequently blurs the visualized reflective layers in a B-Scan. To give a proper notion of this effect, Figure 3.10 compares an acquisition of the same sample with a selected frame size of 1536 and of 2048. Note that due to the already explained symmetry of the FFT (refer back to Figure 1.5), although 1024 and 2048 samples are respectively outputted in each case, only half are visualized when rendering each A-Scan composing the B-Scan.

In some situations, the greater definition of the reflective layers visualized in Figure 3.10-A is preferable despite of the decrease in imaging depth. In others, priority should be given to the second one. Therefore, the selection of the frame size should be adjusted to the sample in question. It is important to refer that, in any case, the user can export the data values of the spectrum signal of each A-Scan obtained in acquisition mode, and afterwards use any signal processing software capable of performing the same processing tasks without the limitation on the number of samples to apply the FFT.

Still in the initialization of the `FFT` object, it is defined a Hanning window. That is because FFT algorithms assume a periodic input signal, which may result in a discontinuity in the edges of consecutive sets of data. That can be avoided by using a window function, assuring that the data at both edges is zero so that there is no discontinuity. Several window functions can be used. A Hanning window (Figure 3.11) is used in our case, which was experimentally verified to offer the best results among the available ones.

Finally, an instruction for ignoring the DC component of the signal is given. In practice, this is the equivalent of setting to zero the first element of the transformed data.

512 1024
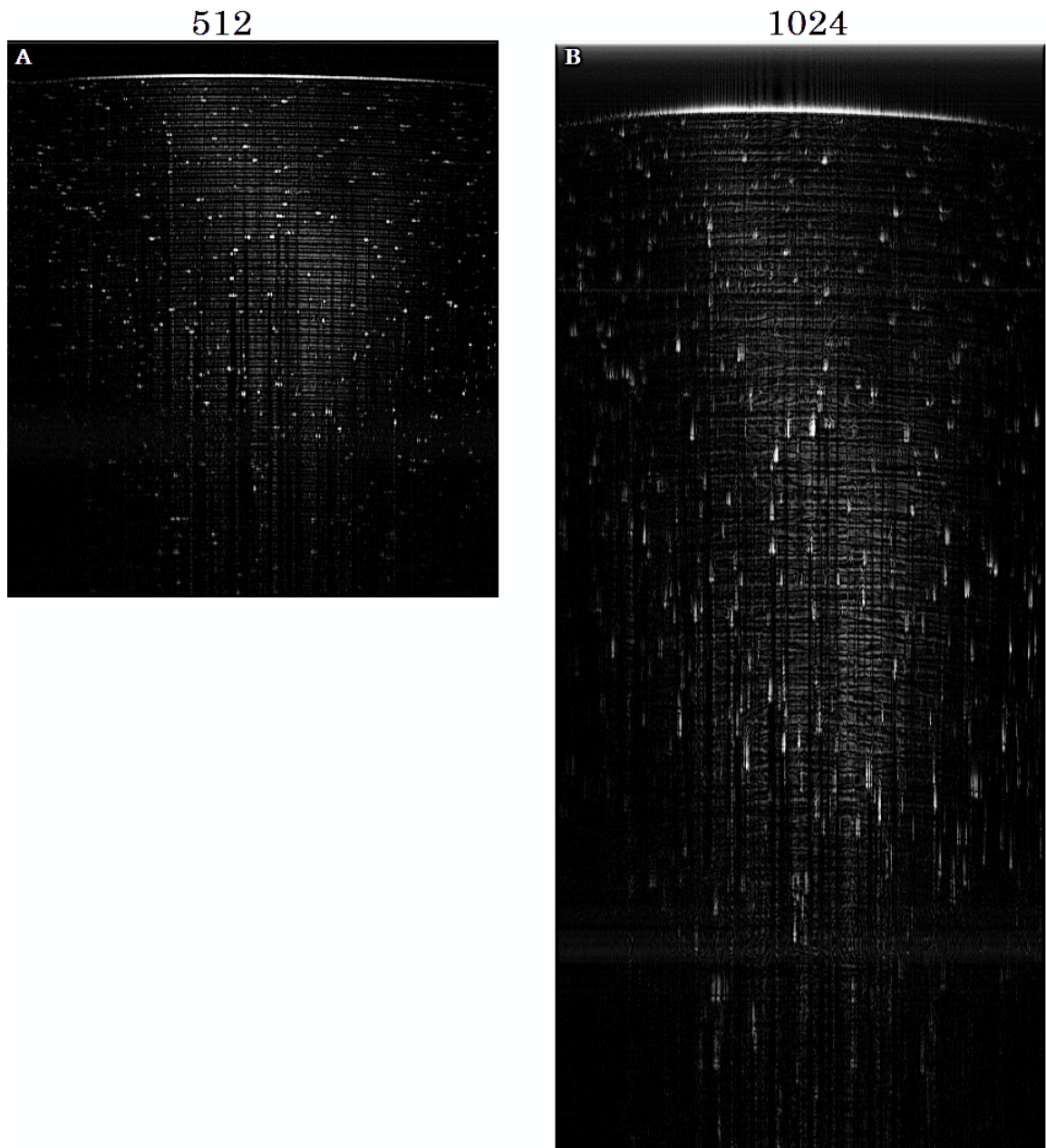
Figure 3.10: B-Scan of an adhesive tape acquired with our OCT system. (A) Acquisition with a selected frame size of 1536, resulting in a FFT with 1024 samples per A-Scan from which 512 are visualized due to its symmetry; (B) Acquisition with a selected frame size of 2048, resulting in a FFT with 2048 samples per A-Scan from which 1024 are visualized due to its symmetry.

The FFT itself consists on 3 instructions:

```
IppCopyInt32Buffer((int*)(&DataSignal[0]), (int*)(&FFT->Time()[0]),
                                            FFTFrameSize*4);
FFT->Transform();
IppCopyInt32Buffer((int*)(&FFT->Spectrum()[0]), (int*)(&FFTData[0]),
                                            FFTFrameSize);
```

Firstly, the raw domain A-Scan data obtained after the previously described 2's complement decoding and zero padding tasks stored in the `DataSignal` array is copied from the PC memory to the SRAM memory of the X5-400M, which as aforementioned is a memory reserved for computational tasks, to which the
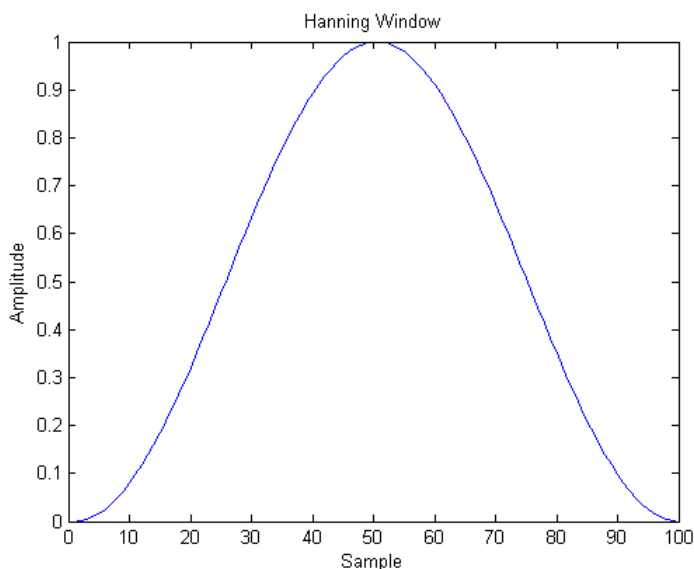
Figure 3.11: Hanning window.

`FFT->Time()` array is associated. The number of copied elements is the length of the `DataSignal`, which is the double of the previously determined number of samples (`FFTFrameSize` $\times$ 2 = 1024) because of the requirement of adding an imaginary part following each real number, corresponding therefore to a total of `FFTFrameSize` $\times$ 2 $\times$ 2 = 2048 samples.

Secondly, the function `FFT->Transform()` implements the FFT algorithm. When it is over, the FFT data output is available at the `FFT->Spectrum()` array, which will contain the `FFTFrameSize` $\times$ 2 = 1024 samples

After this, the data in the `FFT->Spectrum()` array is finally copied again to the PC memory and stored in whatever variable will be used for rendering the processed A-Scan. However, since this data is symmetric, only `FFTFrameSize` = 512 samples are copied.

Note that if a frame size of 2048 was selected, the `FFTFrameSize` would be of 1024 and therefore the sizes of the above mentioned arrays would be the double of the exposed.

3.3.3   Background Subtraction

The background subtraction is an entirely new feature of the current software version. As mentioned in the first chapter, acquiring an A-Scan with no sample present and then subtract it from each subsequent sample A-Scan is an effective way of attenuating the DC artifact and the component from the coherence noise which is not correlated with the sample. Besides these imaging artifacts, the integration of some elements in the DAQ system (such as the detector and the acquisition board) also contributes to the background noise in a way that is not completely random and therefore can be reduced by this subtraction.

Background subtraction can substantially benefit the quality of the visualized images, as well as improve the sensitivity of the system. When normalizing the data from the FFT transform to render an image, weak reflections that have a value in the order of the background noise will be overshadowed by it. By subtracting

the background noise, these weak reflection will now be perceptible. A comparison between two B-Scan corresponding to the same acquisition with the background subtracted in only one of them is shown in Figure 3.12.
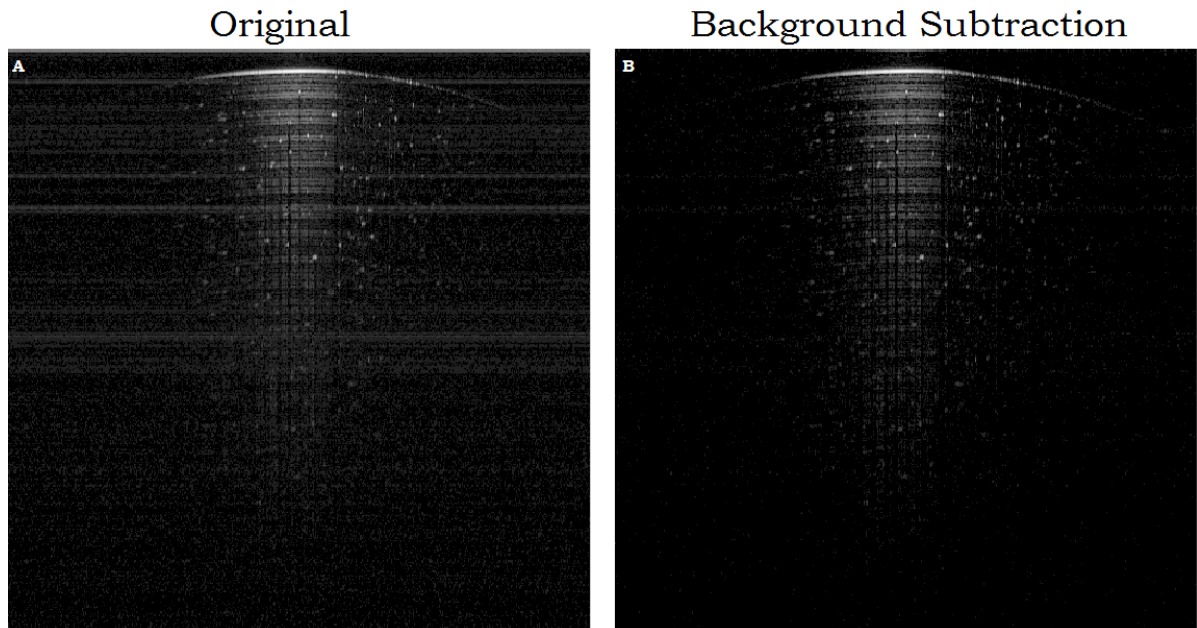
Figure 3.12: B-Scan of an adhesive tape acquired with our OCT system, visualized in logarithmic mode. (A) Original B-Scan; (B) B-Scan after background subtraction.

When analyzing this image, the benefit of this operation becomes clear. In our OCT system this is an optional feature the user can activate using the Background Configuration tool box in the application interface (in Figure 3.4), which becomes enabled when the user clicks the Start button. Two options are available: either recalibrate the background by making a new acquisition of it, by clicking the Acquire Background button, or interact with a check box to start subtracting the last acquired background to the new A-Scans.

If making a new background acquisition, the system automatically enters the acquisition mode and acquires a default number of 10 000 A-Scans. When finished, these are processed, including the FFT procedure. The background is subtracted on the FFT values because if it was subtracted to the spectrum signal, a single value alteration would have an impact on all the values after the FFT application, corrupting the visualized time domain A-Scans and B-Scans. After calculating the FFT of each of the background A-Scans, its average is calculated, originating 1 average background A-Scan which is exported and saved as a binary file, overwriting the previous one. This operation takes less than 1 second. It is obviously vital to remove the sample from the sample arm during this procedure.

When the user choses to subtract the background, the binary file which contains the last acquired background is red and passed to the array `BackgroundNoise`. A boolean variable signalizes this selection and the follwing code in the `doProcessing` method is reached:

```
if (*SubtractBackground){
    for (int iS = 0; iS < FFTFrameSize; iS++)
        FFT->Spectrum()[iS] = FFT->Spectrum()[iS] - BackgroundNoise[iS];
    }
```

As can be seen, every sample of each A-Scan is individually subtracted right after being applied the FFT. Because of this, the rate at which data is rendered in live mode is slightly decreased. This is the motive for leaving this operation as an optional feature, instead of always applying it regardless of the will of the user, who may prioritize a faster imaging over a higher quality one.

When the user clicks the Start Acquisition button to enter the acquisition mode, the data processing subsequent to the acquisition will or will not include the background subtraction depending on the check state of the correspondent check box in the moment the Start Acquisition button is pressed.

3.4 Data Display

As data is being processed in live mode, it becomes available for the user to visualize. Four data rendering options in live mode are available for the user, which are the visualization of the frequency domain spectrum signal, its FFT corresponding to the A-Scans in time domain, a B-Scan formed by successive A-Scans and finally the projection image. Additionally, a volume acquired in acquisition mode can also be rendered in a separate interface. The selection of the wished visualization option is made at the display bar of the interface window (Figure 3.13).
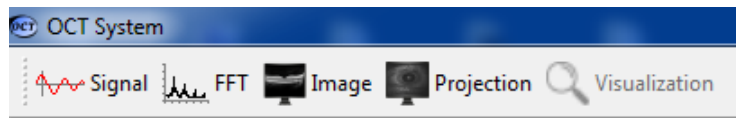
Figure 3.13: Display bar of the interface window of the OCT system.

By clicking any of the enabled display buttons a new window will be opened, separated from the main window represented in Figure 3.2. To each of these new windows a different class is associated: frmGraph, frmFFT, frmImage, frmProjection and frmVisualization, respectively.

To allow sever windows to be opened simultaneously, a multithreading approach is required. A thread is defined as the smallest sequence of programmed instructions that can be managed independently by a scheduler. The existence of multiple threads enables the computer to perform more than one task at a time, which is a requisite in this case. Since one thread may have to wait for a result or need to access a resource from another thread, they often must be synchronized. Synchronization problems are a common cause of errors and bugs in multithreading applications. To grant an adequate synchronization several booleans in each thread are used to control the work flow of the parallel tasks performed.

Thus, each of the mentioned visualization windows will be associated to a separate thread, which is initialized when the user clicks the correspondent button and destructed when the user closes the correspondent window, to prevent the creation of multiple threads performing the same task. The threads associated with each of the windows are respectively `ThreadGraph`, `ThreadFFT`, `ThreadImage`, `ThreadProjection` and `ThreadVisualization`.

3.4.1 Spectrum Signal

When clicking the Signal button, `ThreadGraph` is started and the method associated with it is the frmGraph::RefreshGraph() presented below:

```
public: void RefreshGraph(){
        while(*GraphAlive){
          if (*GraphReady){
            *GraphReady = false;
            for (int i = 0; i < Frames*2; i++)
               DataGraph[i] = DataAcquired[i*2]; //Ignore imaginary part
            panelGraph->Refresh();
            }
          }
        }
```

The `GraphAlive` boolean is made true when the Signal button is clicked and will remain so until the window is closed and the thread is destructed. Meanwhile, the code inside the `while` cycle will be in infinite loop, being always ready to render a new A-Scan spectrum. However, that only happens when the `GraphReady` boolean is made true, which happens after the data from the `DataSignal` array is copied to the `DataAcquired`, in the DataProcessing::doProcessing() method. The high rate at which A-Scans are processed makes it impractical to show every single one. For this reason a timer is associated with this copy, defining that a new A-Scan spectrum should only be copied to be rendered every 0.1 seconds, which is still a high enough refresh rate to grant that no delay in real time imaging is perceptible to the user.

It is also important to attend to the fact that when scanning the sample, the successive acquired A-Scans will be different. To allow the user to keep visualizing the spectrum correspondent to the same point of the sample, it is always copied the same sub-packet index within each acquired packet. This index was defined to be the correspondent to the central A-Scan of each B-Scan.

Once this copy is made,`GraphReady` is true and the subsequent instructions of the above code are reached. Firstly, `GraphReady` is reset to false to prevent receiving a new set of data while rendering a previous one. Because the `DataAcquired` is a straight copy of the `DataSignal`, all values contained in the odd indexes will refer to an irrelevant imaginary component as previously explained. Therefore, this data is copied value by value to a new array `DataGraph`, but this time leaving out the imaginary components. All the processing tasks needed to render the spectrum are now completed and the data in the last mention array can be displayed. To do this, the `panelGraph->Refresh()` instruction invokes another method of the same class which converts the data in the `DataGraph` array to a set of y coordinates normalized to correspond to the true acquired voltage by the board. The conversion from digital scale to voltage depends exclusively on the board's input range and ADC resolution, being given by:

$$\text{Volts} = \frac{2}{2^{14} - 1} \times \text{Digital} \; - \; 1 \qquad (3.3)$$

The A-Scan spectrum will then be displayed to the user as represented in Figure 3.14.

This window has the additional options of selecting a specific y or x axis visualization range and exporting the current spectrum data to a binary file.
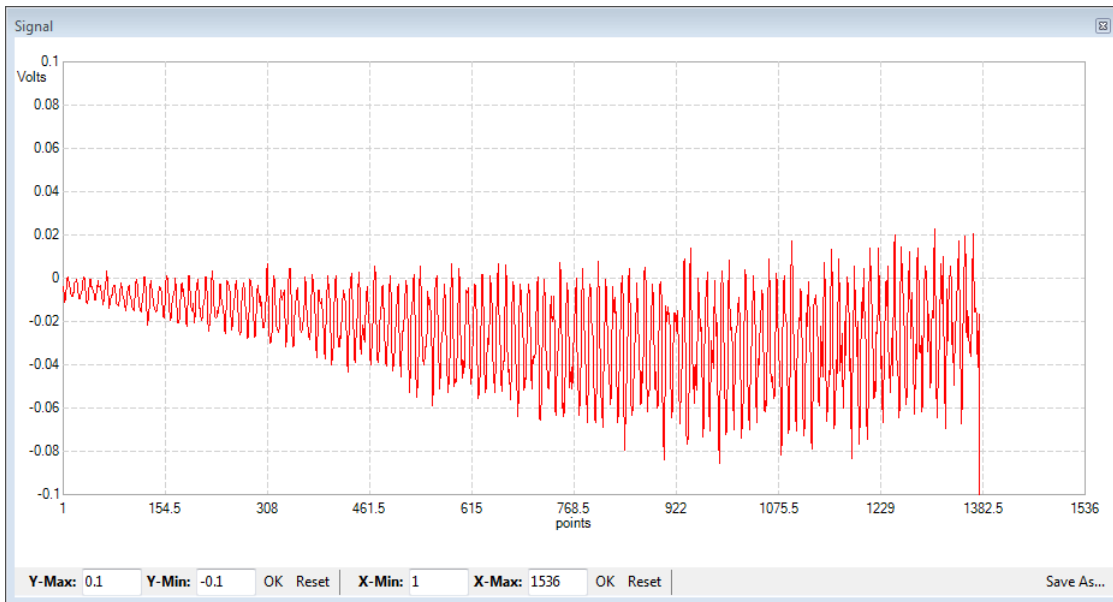
Figure 3.14: Signal window, displaying an acquired A-Scans spectrum (frequency domain) of an adhesive tape.

3.4.2   FFT

This window is very similar to the previous one, only differing in the data that is displayed. By clicking the FFT button, `ThreadFFT` is started and consequently the method frmGraph::RefreshFFT() is reached:

```
public: void RefreshFFT(){
        while(*FFTAlive){
          if (*FFTReady){
             *FFTReady = false;
             panelFFT->Refresh();
             }
          }
        }
```

The flow control booleans work analogously to the ones of `ThreadGraph`, already explained. The data to be rendered in this window origins from the `FFT->Spectrum()` array which stores the samples outputted by the FFT. Since these values need no extra processing, the `panelFFT->Refresh()` instruction is immediately given which paints the picture box in the window with the referred data set, producing the result shown in Figure 3.15.

Analogously to the Signal window, this A-Scan is refreshed every 0.1 seconds and corresponds to the same central A-Scan.

3.4.3   Image

When clicking the Image button, `ThreadImage` is started and the method frmGraph::RefreshImage() is called, which operates analogously to the previously exposed methods, only with different processing instructions.
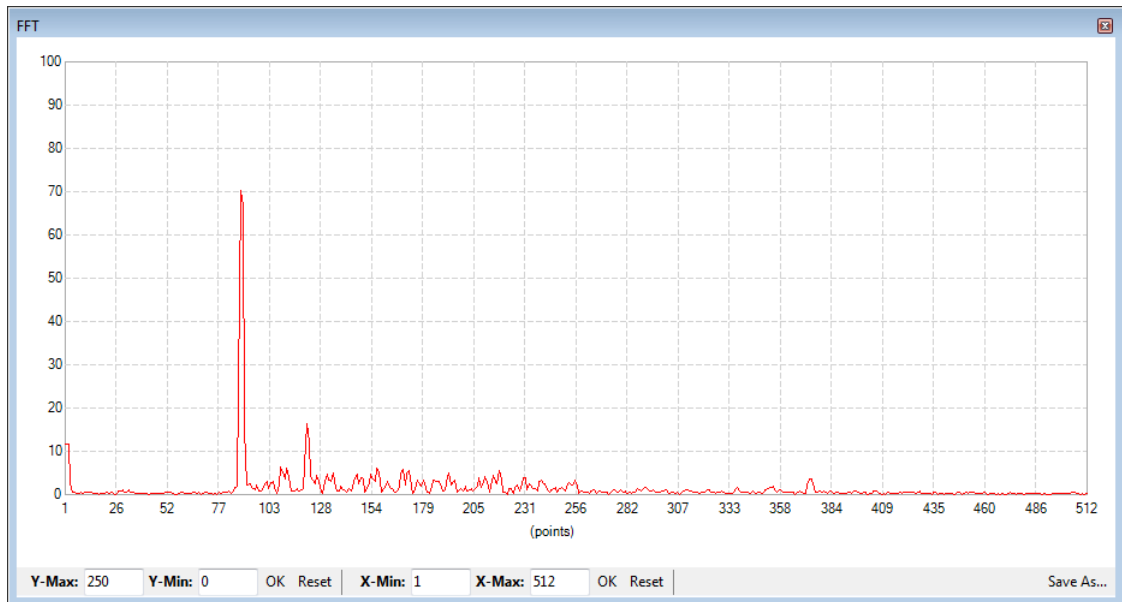
Figure 3.15: FFT window, displaying an acquired A-Scan of an adhesive tape now in time domain.

This time, it is an entire packet corresponding to 1 B-Scan that must be copied from the `FFT->Spectrum()` to the `DataAcquired` array which will contain the raw information of each B-Scan. As the required processing tasks are performed, data ready for rendering is stored in the `ImageData` array.

However, the processing tasks in this thread are a bit more complex, since they must be applied to every single A-Scan in the packet. Firstly, there is the need to normalize the image to allow its visualization in the typical 8-bit RGB color model. This means that each pixel of B-Scan image is obtained the by superposition of 3 different colors (red, green or blue), each one with a relative amplitude factor between $[0, 2^8 - 1] = [0, 255]$. To make full use of this dedicated range, the maximum and minimum value of each B-Scan must be determined and afterwards a linear normalization is performed according to the formula:

$$I_N = \frac{I - Min}{(Max - Min)} \times 255 \qquad (3.4)$$

Where I and I_N correspond to the image values before and after normalization, respectively. This normalization is made resorting to the follwing code:

```
for (int i = 0; i < AScans*Frames; i++){
    BScanMax = BScanMax > DataAcquired[i] ? BScanMax : DataAcquired[i];
    BScanMin = BScanMin < DataAcquired[i] ? BScanMin : DataAcquired[i];
    }
if (!ModeLogarithm){
    for (int i = 0; i < AScans*Frames; i++){
        ImageData[3*i] = (unsigned char) (DataAcquired[i]-BScanMin)
                                        /(BScanMax-BScanMin) *255.0;
        ImageData[3*i + 1] = ImageData[3*i];
        ImageData[3*i + 2] = ImageData[3*i];
        }
    }
```

99

As can be seen, images will be rendered in gray scale, since every 3 consecutive elements in `ImageData` will be equal, i.e. R=G=B. After this data is ready to be displayed to the user as a B-Scan. However, this is only if the user selects a linear scale visualization, recorded by the `ModeLogarithm` boolean which in this case would be false.

Visualizing the B-Scan on a logarithmic scale allows obtaining a greater image contrast. This option was already tested in previous work[26] but not properly implemented in the software, being a new feature of this version. If the user selects this option, extra processing steps are needed:

```
else if (ModeLogarithm){
  for (int i = 0; i < AScans*Frames; i++){
     PositiveData = DataAcquired[i] > 0 ? DataAcquired[i] : 0;
     ImageLog[i] = (float) Math::Log10( (PositiveData - BScanMin)
                                         /(BScanMax-BScanMin)*255 +1);

     }
  for (int i = 0; i < AScans*Frames; i++){
     BScanMax = BScanMax > ImageLog[i] ? BScanMax : ImageLog[i];
     BScanMin = BScanMin < ImageLog[i] ? BScanMin : ImageLog[i];
     }
  for (int i = 0; i < AScans*Frames; i++){
     ImageData[3*i] = (unsigned char) (ImageLog[i] - BScanMin)
                                        /(BScanMax-BScanMin) *255;
     ImageData[3*i + 1] = ImageData[3*i];
     ImageData[3*i + 2] = ImageData[3*i];
     }
   }
```

Firstly, we have to account for the fact that if background is being subtracted, negative values with small amplitude can be originated due to the noise statistical variation. Although having negative values in an image data array makes no sense, they are not a problem when visualizing in linear mode, because they will be equally normalized. Forcing the negative values to zero before normalization would be more correct approach, however when rendering B-Scans in live mode that would have no perceptible impact in the obtained images, but would decrease their refresh rate since extra computation time would be required. For this reason, this detail is overlooked in linear mode in benefit of the system performance. But when applying a logarithmic scale, every sample must have a positive value so that no mathematical exception is raised. For this reason a new array `PositiveData` copies only the positive data to it and sets to zero the negative values.

After this, the logarithm of the normalized positive data is calculated and saved into the `ImageLog` array. Note that this time the normalization must be in the range $[1, 256]$, since the presence of zero values would raise a mathematical exception when calculating the logarithmic. Thus the value $+1$ is added after the regular normalization.

Before rendering, it is still necessary to normalize the logarithmic data so that it can be properly displayed. Therefore the minimum and the maximum values of `ImageLog` are determined and the normalization is made, again basing on Equation 3.4.

A representation of this window visualizing a B-Scan in linear scale is shown in Figure 3.16.

As can be seen, in the bottom of the window the Display Mode buttons allow
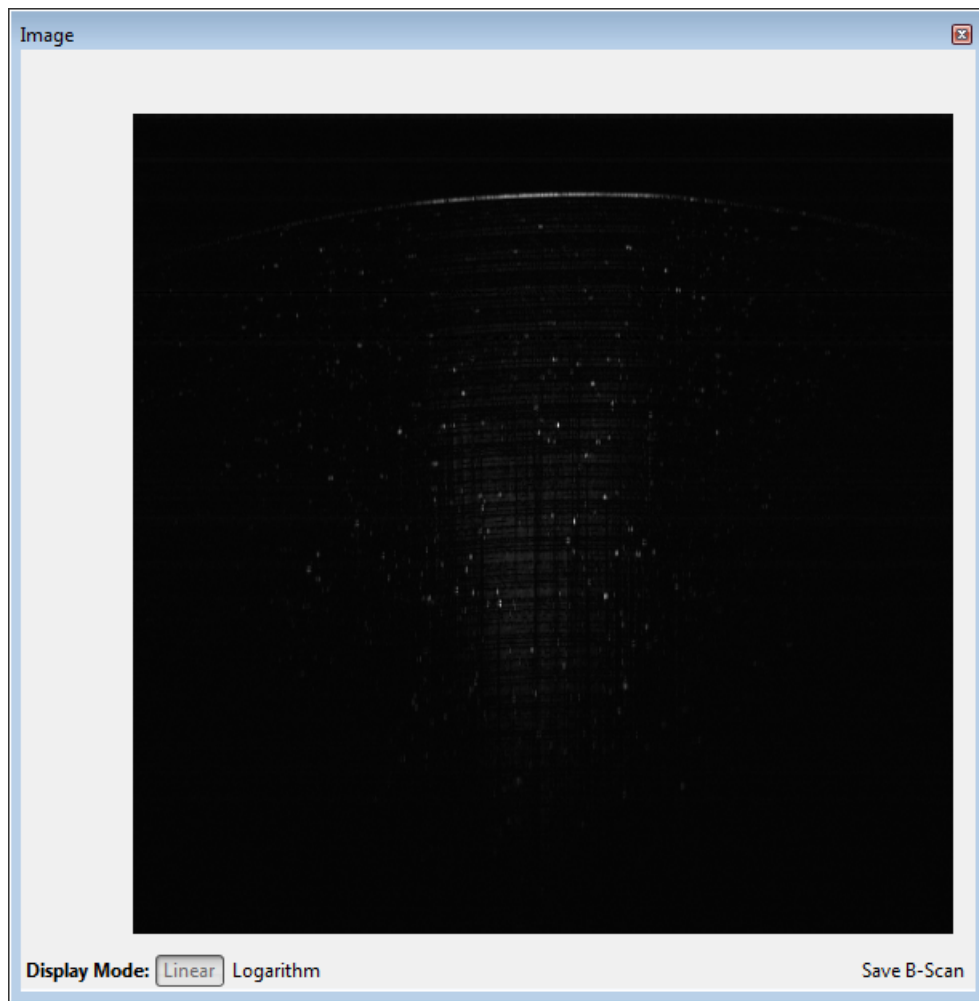
Figure 3.16: Image window, displaying a B-Scan. The sample visualized is an adhesive tape in a 512 A-Scans acquisition.

alternating between the linear and logarithmic scale. An option of saving the B-Scan is also present, which exports the image currently being visualized to a .png file.

3.4.4   Projection

The concept of a projection image was already explained, being summed up in Figure 1.38. The information of each B-Scan will now correspond to a 1 dimensional horizontal line, in which each pixel contains the sum of the samples in each A-Scan.

It was decided that is was more favorable to refresh the projection image line by line in live mode, i.e. render each B-Scan as it is acquired instead of waiting for an entire volume acquisition and only after display the complete projection image. This option allows the user to see the already available data more quickly, reducing the time delay between the acquisition and the correspondent image display which is a priority in real time imaging.

Thereby, data copies to the rendering method frmGraph::RefreshImage() associated with `ThreadProjection` are made after each B-Scan is processed. However, before this it is necessary to calculate the sum of the samples along each A-Scan. That is done still in the ProcessingData::doProcessing() method:

```
for (int iS=0; iS < FFTFrameSize; iS++){
   if (*PreviewAlive){
      if (iS == 0) //Reset the sum value before a new A-Scan
         PreviewData[iA+(AScans-IgnoredAScans)*BScan] = FFT->Spectrum()[iS];
      else
         PreviewData[iA+(AScans-IgnoredAScans)*BScan] += FFT->Spectrum()[iS];
   }
}
```

This code transcribes the implementation of Equation 1.50.

Having now the data from 1 B-Scan ready to be displayed, the above presented array `PreviewData` is copied to the `DataAcquired` to be linearly normalized and rendered.

```
for(int iA = 0; iA < AScans; iA++){
   BScanMax = BScanMax > DataAcquired[iA+AScans*iB] ?
                           BScanMax : DataAcquired[iA+AScans*iB];
   BScanMin = BScanMin < DataAcquired[iA+AScans*iB] ?
                           BScanMin : DataAcquired[iA+AScans*iB];
}
for (int iA = 0; iA < AScans; iA++){
   ProjectionData[3*(iA+AScans*iB)] = (unsigned char)
         (DataAcquired[iA+AScans*iB] - BScanMin)/(BScanMax-BScanMin) *255;
   ProjectionData[3*(iA+AScans*iB)+ 1] = ProjectionData[3*(iA+AScans*iB)];
   ProjectionData[3*(iA+AScans*iB)+ 2] = ProjectionData[3*(iA+AScans*iB)];
}
```

Every time a new B-Scan is finished being processed, the explained cycle is repeated. The `iB` counter keeps track of the B-Scan number in the volume so that the proper horizontal line in the projection image is refreshed.

The Projection window is presented in Figure 3.17. While the dimension in pixels of the B-Scans displayed in the Image window depends on the acquisition parameters (i.e. the x×y dimensions are proportional to A-Scans×Frame Size), the projection image displayed in this window has a set size of 512×512 pixels, so it is either shrieked or stretched by a Visual Studio library method by means of interpolation (except in the case of a 512×512 volume, obviously). This makes the projection image more legible when smaller volumes are acquired.

As in the Image window, an option for saving the visualized projection is offered, exporting it to a .png file.

3.4.5   Visualization

This window was developed to be accessed in acquisition mode, after the acquisition and data processing is finished. When this happens the Visualization button of the display bar becomes enabled, while all the other ones will be disabled. When opened, as shown in Figure 3.18, it contains the projection image of the acquired volume as well a B-Scan among the acquired ones.

The processing tasks required to render the B-Scan and the projection images are the same as the ones in live mode, with the only difference that this time the entire volume is copied and processed at once.
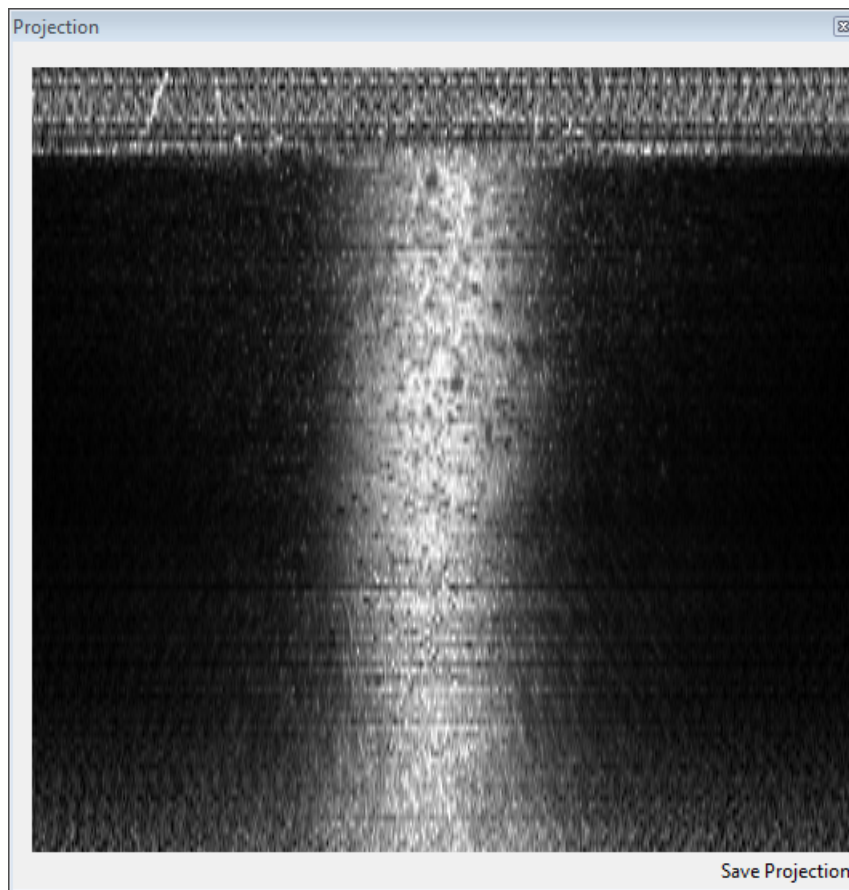
Figure 3.17: Projection window, displaying the projection of an acquired volume. The sample visualized is an adhesive tape in a 512×128 volume acquisition. Since every B-Scan in this volume is very similar the projection image will show no significant alterations along each vertical line.

A scroll bar at the right allows the user to navigate along the acquired B-Scans, and a white horizontal line added to the projection image informs on the correspondent position in the volume of the visualized B-Scan.

At the bottom, the Linear and Logarithmic buttons adjust the scale of the B-Scan. An Average button is also present, a new feature that was suggested in previous a work[26]. This can be useful when acquiring a volume of B-Scans with a static y-axis mirror since a B-Scan averaging contributes significantly to remove the random noise component present in the image. This averaging is done by the follwing instructions:

```
for (int i = 0; i< Frames*AScans; i++)
   AverageData[i] = 0;
for (int iS = 0; iS < Frames; iS++){
   for (int iA = 0; iA < AScans; iA++){
      for (int iB = 0; iB < BScans; iB++)
         AverageData[iS + iA*Frames] +=
                       ImageVolume[iS+iA*Frames+iB*AScans*Frames]/BScans;
   }
}
```

Each pixel in the average B-Scan is given by the sum of every pixels in that same position in every B-Scan, divided by the number of acquired B-Scans, thus yielding an average value.

Saving the visualized images to a .png file is also possible. The exported B-Scan
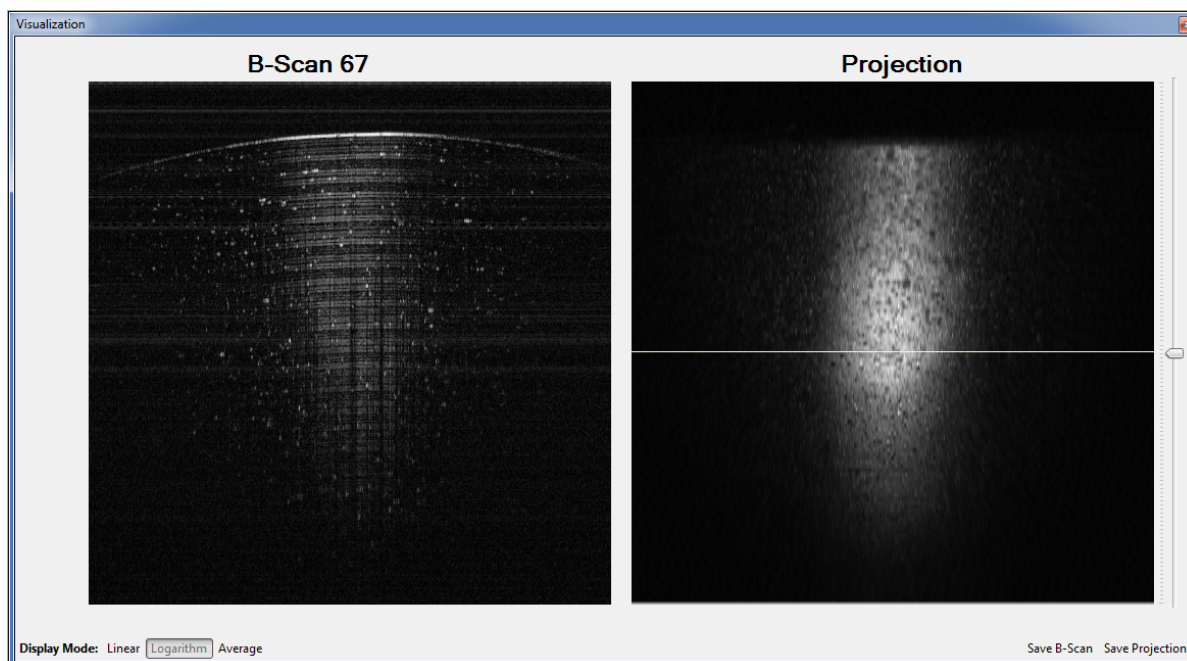
Figure 3.18: Visualization window, displaying the B-Scan selected by the user and projection of the volume. The sample visualized is a transparent adhesive tape in a 512×128 volume acquisition.

corresponds to the one being visualized at the moment.

3.5 Saving Data

The final step of an OCT acquisition is to save the acquired volume. Saving options in live mode were already mentioned, consisting on the A-Scan spectrum and FFT exportation as a binary file and the B-Scan and projection image outputted as a .png image. But it is als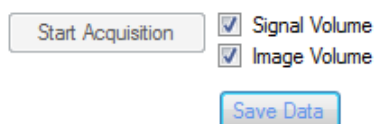o possible to export a volume acquired, not only the images in the Visualization window, but also the spectrum and FFT of every single A-Scan in the volume as a binary file. To do so, after the data processing in acquisition mode is finished, the Save Data controls become available as seen in Figure 3.19.

Figure 3.19: Save Data controls used to export the spectrum signal and/or the FFT of every A-Scan in the acquired volume.

The user can tick or untick each presented box to determine if the A-Scans spectrum signal (Signal Volume box) and/or the correspondent FFT (Image Volume box)will be exported. After this selection, the Save Data button should be clicked, which opens a dialog box as represented in Figure 3.20.

Each selected tick box will open a different dialog box and consequently will create a separate binary file. The user can then select the folder in which this file will be saved, as well as change the filename. By default, the filename selected is the type
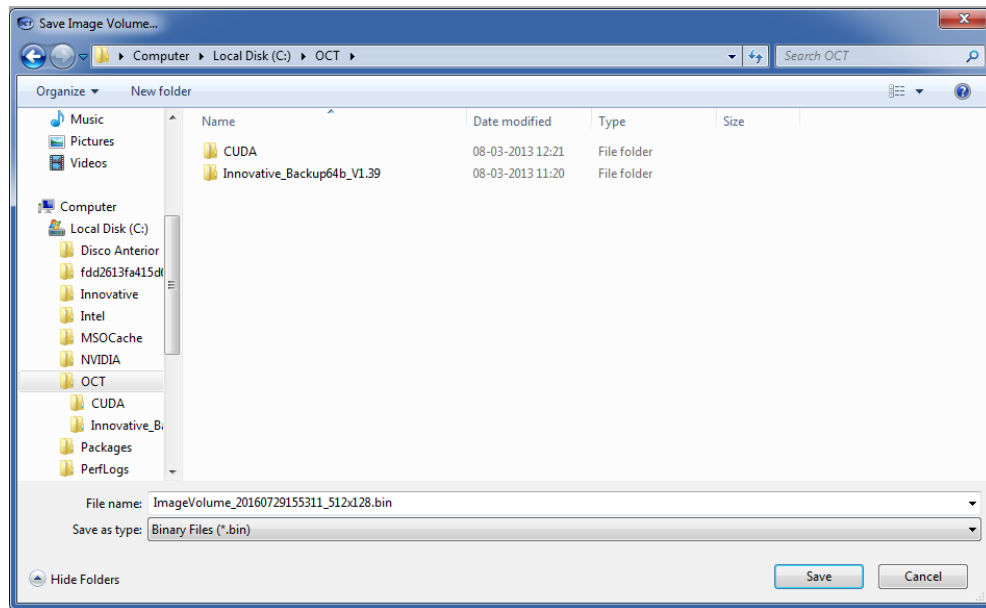
Figure 3.20: Dialog box that pops up when the Save Data button is clicked. This specific one corresponds to the Image Volume tick box.

of data being exported (SignalVolume or ImageVolume for the spectrum and FFT, respectively), followed by the date and time of the acquisition (the computer time at the moment the Save Data button was pressed, in format year-month-day-hour-minute -second) and finally by the size of the volume acquired (in format A-Scans × B-Scans). An example of this default filename is also illustrated in Figure 3.20.

The Signal Volume file will have a number of samples given by the defined values FrameSize × A-Scans × B-Scans selected. The Image Volume file will contain FFTFrameSize × A-Scans × B-Scans samples. As aforementioned, if the FrameSize selected is of 1536, the FFTFrameSize will be 512, while if it were to be 2048 the FrameSize would be of 1024.

Binary files are written as single-precision floats, which use 32 bits to represent the value. When using a distinct software to read the data contained in the generated binary files, this same format must be specified. Since different programs may define a float with a different number of bits (e.g. 64 bits instead of 32 bits), it is recommended not to read the binary file as floats, but rather as int32, thus specifying the correct precision. Since typically the number of values that will be red must also be specified, it is a good idea to specify it in the filename as is made by default.

The way the A-Scans spectra and FFTs are exported in live mode when using the proper buttons in the correspondent window is equal to the explained in this section.

4 | *Imaging Tests Results*

This work would not be complete without presenting some images acquired in OCT tests. While developing the acquisition software, it would be impossible to use an actual living being as sample during the hundreds of hours dedicated to software development. Therefore, mostly static samples were used along this work. Since the focus of this work is the improvement of the acquisition system, an effort was made to alienate negative influences related to the optical apparatus. One example of this is the sensitivity of the system, which is why highly reflective samples were first used, to ensure that, if the system was not acquiring the expected signal, it was not because of the its optical component but rather due to the acquisition system. The development process was to guarantee that the system was reliable when acquiring in a perfect set of conditions, and gradually approximate those to the ones existing when imaging small animals.

That being said, from the multitude of static samples analyzed, only some of them will be present, strategically selected for having certain interesting features. These samples will be a gold coated mirror, a coin, an opaque and a transparent adhesive tape.

Finally, one of the great achievements of this project was the fact of the system being finally ready to perform real time imaging in living samples. There was the opportunity of testing this system in a rat with the aim of imaging its eye. This experiment will also be discussed in this chapter and results will be shown.

In every acquisition the selected frame size was of 1536 frames, thereby outputting a vertical resolution of 512 frames in each A-Scan. Every B-Scan presented in this chapter was acquired with a set number of 512 A-Scans. The projection images shown correspond to a volume of 512×512.

4.1   Gold coated Mirror

A picture of this sample is shown in Figure 4.1. This was the first one of the most common samples used in during the software development, since it had the highest reflectivity.
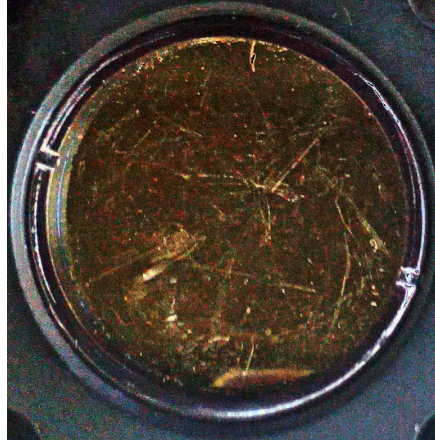
Figure 4.1: Gold coated mirror.

The correspondent projection image is presented in Figure 4.2. The resolution of it is high enough to easily distinguish the several scratches in the surface of the mirror.
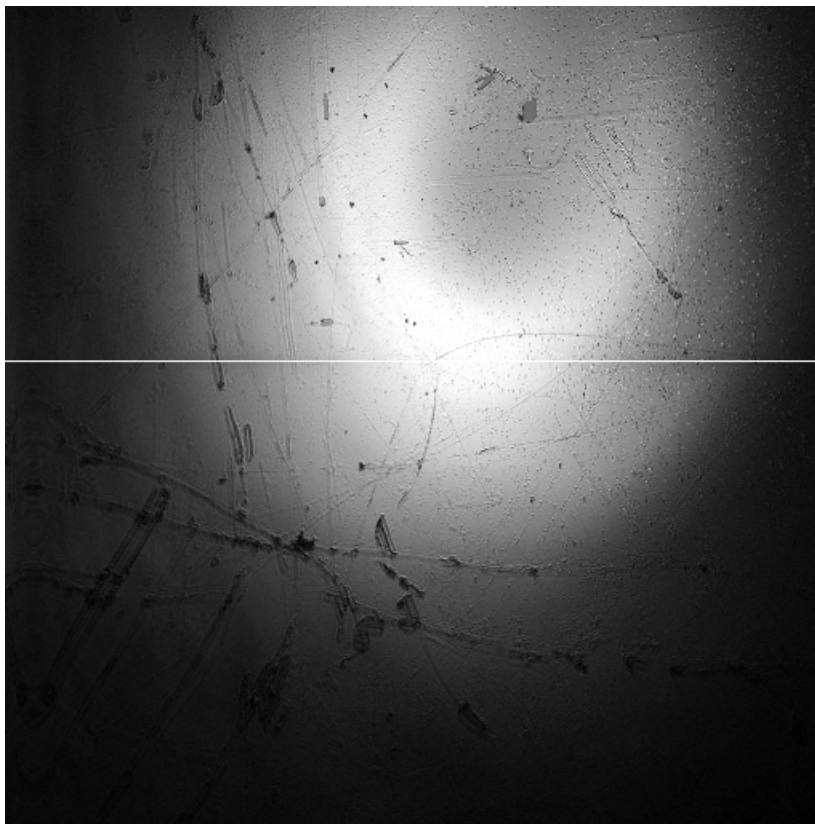
Figure 4.2: Projection image with a 512×512 resolution of the gold coated mirror. The white horizontal line makes the correspondence to the visualized B-Scan in Figure 4.3.

The B-Scan scanned along the sample in the position suggested by the white in the projection image is shown in Figure 4.3, both in linear and logarithmic scale.
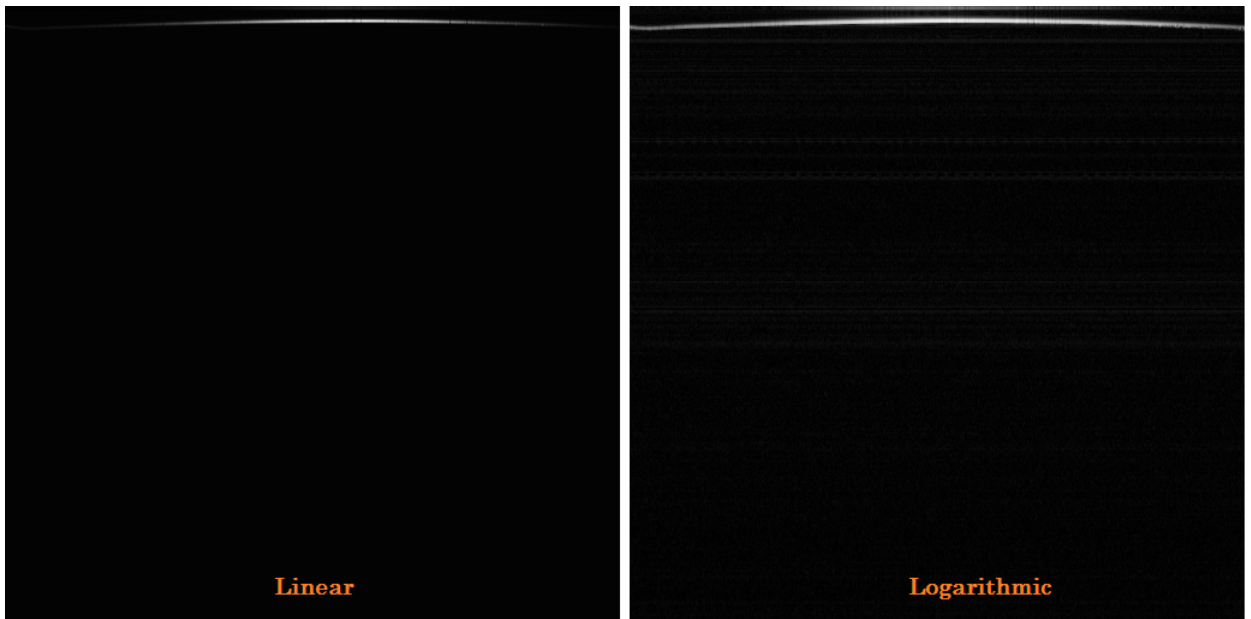
Figure 4.3: B-Scans with a 512×512 resolution of the gold coated mirror in linear scale (left) and logarithmic scale (right).

Some considerations can be made by analyzing this B-Scan, that are common to every other one along this chapter. For instance, although the surface of the sample is plane, we can see a slight curvature on the B-Scan. That is due to the scanning, that forces the laser path length in the sample arm to be greater when an edge of the sample is focused than when focusing the center. Ultimately it is the difference in the path length traveled by the laser in the reference and sample arm that dictates the position of the reflective layers in the sample, an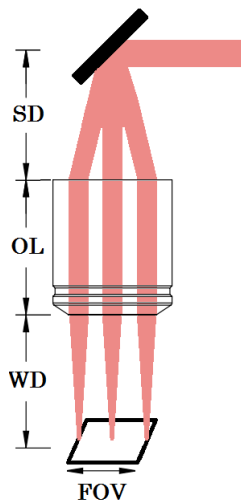d the reference arm length does not account for this variable scanning effect. Therefore, the extra length traveled to reach the edges of the sample is interpreted as a further reflective layer, which creates this curved sample illusion in the B-Scan. For a more concrete insight on this issue, let us consider the scheme of the sample arm in Figure 4.4.

$$\text{Laser Path} = \left(\sqrt{SD^2 + \frac{FOV^2}{4}} + OL + WD \right) \times 2 \quad (4.1)$$

Figure 4.4: SD - Scanning Distance (18.9 mm); OL - Objective Lens (25.5 mm); WD - Working Distance (25.1 mm); FOV - Field of View (9.4 mm)

The path length traveled by the laser beam when it leaves the optical scanning mechanism depends on a set of specifications of the objective lens used, namely the

scanning distance, objective length, working distance and field of view. The value of each mentioned parameter for the Thorlabs SMS03-BB lens used in this OCT system is presented in the label of the respective figure. Using basic trigonometry, we can easily deduce the equation that describes the extension of this path as a function of the selected field of view, i.e. the extension of the sample being sampled. This relation is given by Equation 4.1. The factor of two accounts for the identical length traveled after being reflected by the sample. To interpret the practical effects of this equation let us analyze the following plot:
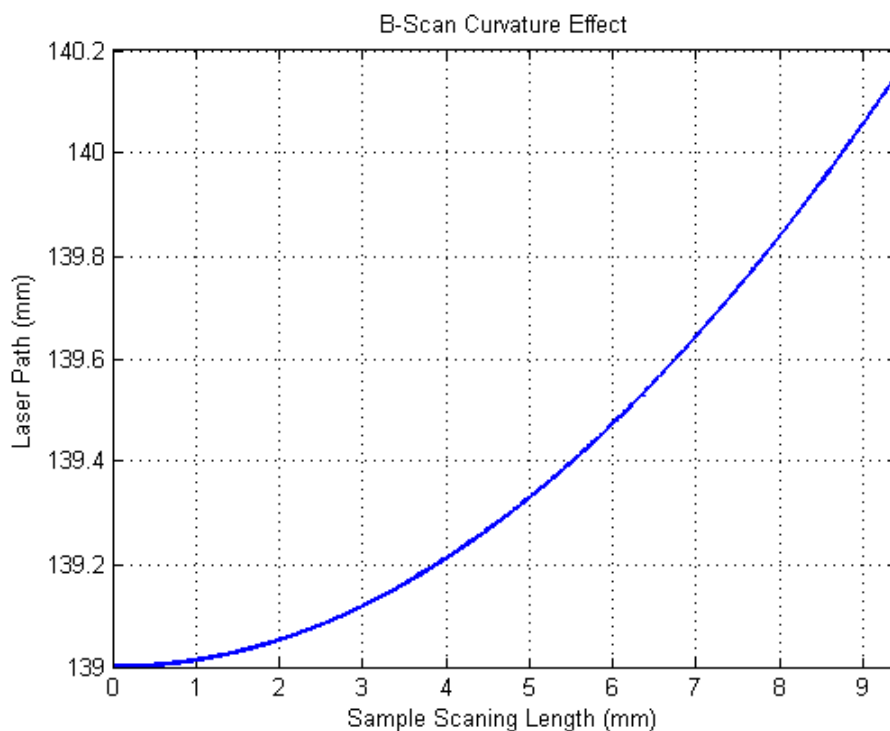
Figure 4.5: Plot of the laser path as a function of the length scanned in the sample by the beam.

As can be seen, if the maximum allowed field of view is scanned, the result interpreted by the system is equivalent of having the edges of the sample more than 1 mm further away than the center of the sample. The axial resolution of the system is perfectly capable of detecting this path length difference, which leads to the described curvature effect. Note that in Figure 4.1 the scanning extension was inferior to the maximum field of view, therefore this effect is not as dramatic as it could be. However, this is usually not a significant hold back in eye imaging since the eye is already curved by nature, so this effect only slightly exaggerates this characteristic.

One can also compare the differences between the linear and logarithmic scale in this specific case. As previously mentioned, when rendering B-Scans in logarithmic scale an increase in contrast is expected to be obtained. However, Figure 4.3 shows no dramatic differences between both scales. This is only because the sample in question is highly reflective, having a reflectance many times superior to the one of a biological sample. Therefore, when normalizing the image, a restrict set of frames along each A-Scan will yield values equal and very close to the maximum normalization factor, corresponding to the reflective surface of the mirror, while all the other values will be very close to 0. This contrast is already so great that the

effect of scaling these values to logarithmic has almost no practical effect. Still, we can verify that the scanned edges of the sample, which contain inferior values due to the curvature effect described, are more visible in logarithmic scale.

4.2   Coin

A coin was also tested by this OCT system, mainly because it also has a good reflectivity and it contains raised shapes above a flat surface, which makes it ideal to test the resolution of the projection images obtained. It was used a Portuguese 1 € coin, portrayed in Figure 4.6.

Figure 4.6: Portuguese 1 € coin used in the OCT imaging test. The yellow circle corresponds to the estimated scanned zone according to the obtained projection.

The obtained projection is presented in Figure 4.7.
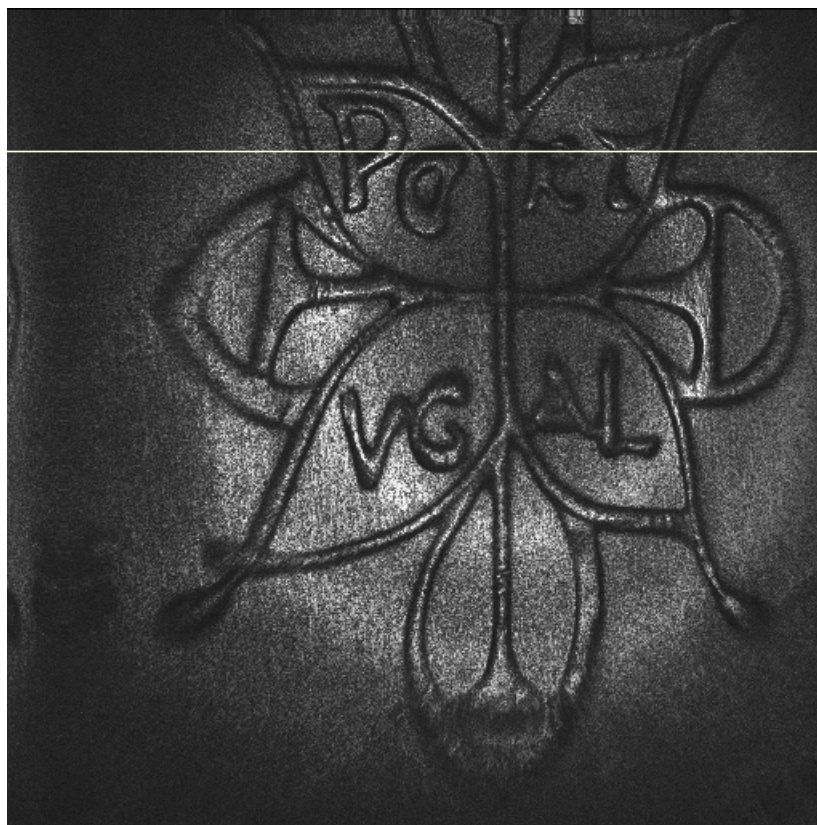
Figure 4.7: Projection image with a 512×512 resolution of the coin. The white horizontal line makes the correspondence to the visualized B-Scan in Figure 4.8.

The obtained result is very satisfactory, since the shapes in relief are completely perceptible and well defined. The scanning of the sample was adjusted to contain the relief of the royal stamp, which has a diameter of approximately 10 mm, being superior to the diameter of the eye of a mouse or rat (3.32 mm and 6.41 mm, respectively[44]). When imaging smaller samples, decreasing the voltage range sent to the galvanometer mirror system allows scanning a smaller area keeping the same image resolution.
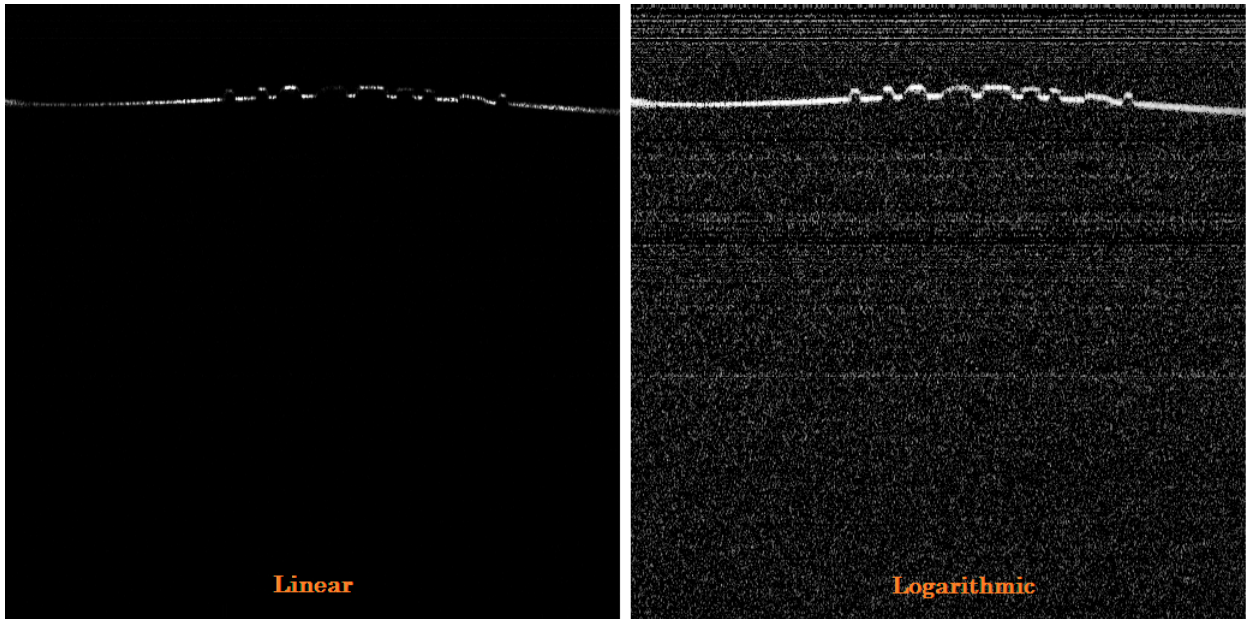
The B-Scan highlighted in the projection image is represented in Figure 4.8:

Figure 4.8: B-Scans with a 512×512 resolution of the coin in linear scale (left) and logarithmic scale (right).

Comparing the presented B-Scans, the benefits of using a logarithmic scale are more evident than in the last case. Because this sample is not as flat and smooth, and composed by a different metal (nickel brass), it is not as reflective as the gold mirror. Therefore the contrast between the A-Scans FFT values corresponding to the reflective layer and to the background is not as accentuated. Another visible aspect is the fact that by using the logarithmic scale, the background is also enhanced. That is expected to happen since, due to the nature of the logarithm function, after this operation and a new normalization, the difference between the higher and the lower values in a normalized B-Scan is not as significant as before this operation. To get a better understanding of this matter, let us regard a practical example by considering a normalized B-Scan in range $[1, 256]$ (and not $[0, 255]$ to be able to calculate the logarithmic values without throwing a mathematical exception). If we select a very high value (corresponding to a reflective layer) and a very low value (corresponding to background noise fluctuations) among the B-Scan, for instance $I_{high} = 250$ and $I_{low} = 5$, we have an intensity difference of $\Delta I = 245$. Because we know the range of values to which the logarithmic transformation is applied, we know that the minimum and maximum values will be of $Min = \log(1) = 0$ and $Max = \log(256)$. Thus, we can use Equation 3.4 to determine the intensity values of the two selected points in the new logarithmic scale normalized image, being given by:

$$I_{N_{high}} = \frac{\log(250)}{\log(256)} \times 255 \;=\; 254$$

$$I_{N_{low}} = \frac{\log(5)}{\log(256)} \times 255 \;=\; 74$$

Thus, an intensity difference of $\Delta I = 245$ was reduced to only $\Delta I_{\log} = 180$ when visualizing the B-Scan in logarithmic scale. For this reason, small values are enhanced comparatively to greater values, and the background noise is more visible in this scale.

4.3 Transparent Adhesive Tape

We will now view the results of the imaging tests performed using a transparent adhesive tape (Figure 4.9). We label this one transparent in comparison to another adhesive tested that was more opaque, which we will leave for the next section.
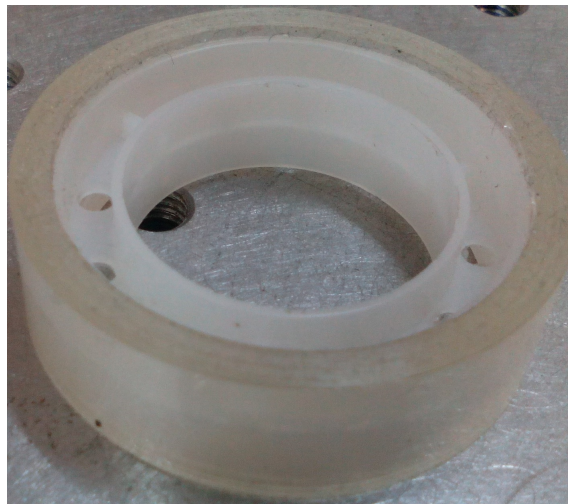
Figure 4.9: Transparent adhesive tape.

Unlike the preceding samples, this one shows no major irregularities along neither the vertical or horizontal axis, and therefore originates a very regular projection image, as can be seen in Figure 4.10.

113
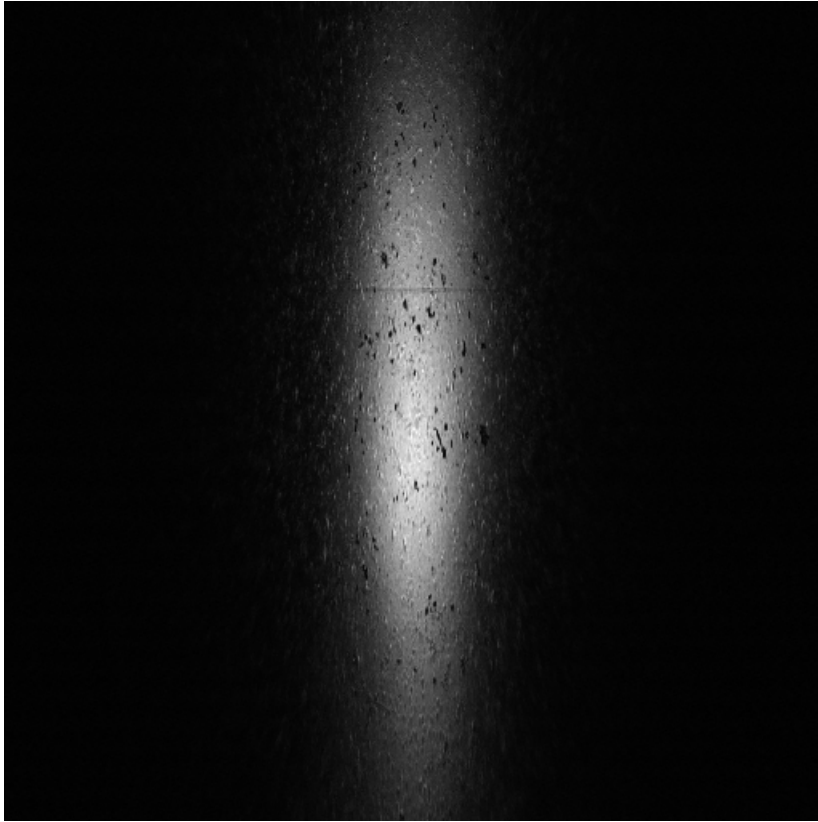
Figure 4.10: Projection image with a 512×512 resolution of the transparent adhesive tape.

An interesting characteristic of this projection is the big intensity difference verified in the center and edges of each horizontal line. That indicates that the B-Scans that compose it are also much more intense in the center than in the edge, which is proven in Figure 4.11.
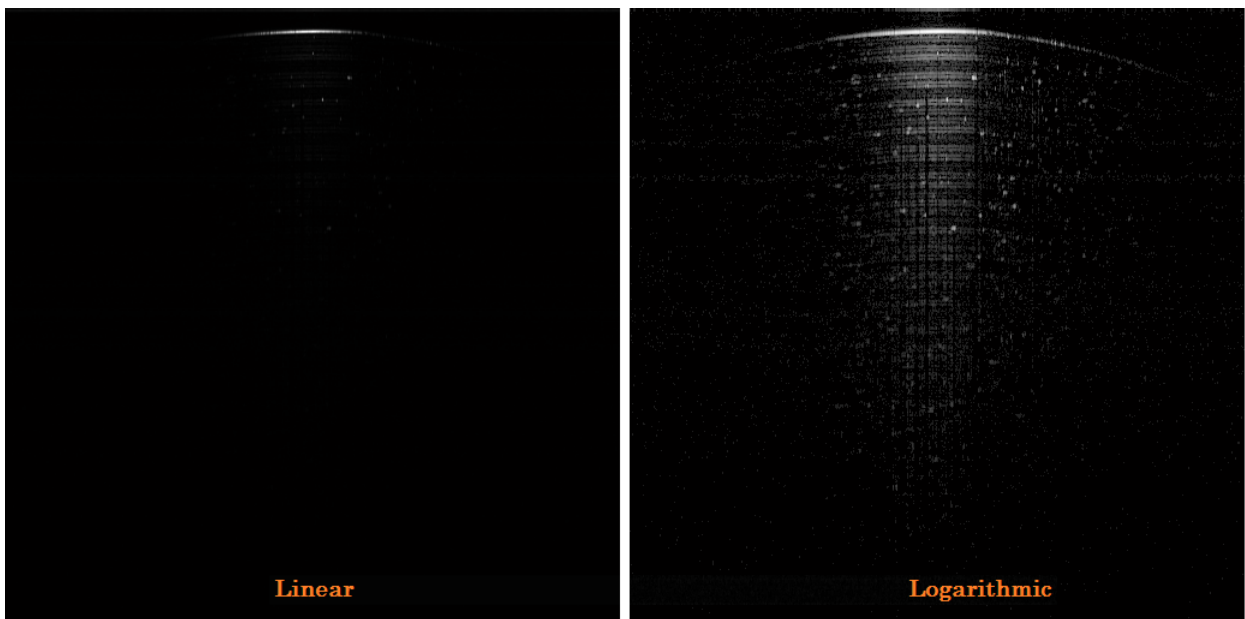
Figure 4.11: B-Scans with a 512×512 resolution of the transparent adhesive tape in linear scale (left) and logarithmic scale (right).

This sample is significantly less reflective than the previous ones. For this reason, it can only be properly viewed in logarithmic scale. The reason why the center of the

sample shows significantly more intense values than the edges is a result of several contributions. Namely, the curvature effect described above added to the fact that the sample is already naturally curved. Since the sample center of the sample is adjusted to coincide with the focus of the objective lens, the scanned edges of it fall slightly behind this point which causes reflections to be weaker. Another reason is the fact that the scanned area was superior to the specified field of view, and therefore the lens could no longer perform satisfactorily on the edges.

Note that the white dots visible in the B-Scan is not speckle noise, although resembling it, but characteristics of the sample, since it is verified that they are always in the same positions. These are then due to the existence of some residues which are more reflective than the layers of the tape. In some cases we can even verify that light is blocked by it, and no more layers of the adhesive tape are visible below it.

4.4   Opaque Adhesive Tape

Another adhesive tape was used as sample, this time a less transparent one (Figure 4.12), which is useful to discuss the impact of this characteristic in the maximum imaging depth z_{max}. It is important to clarify that when we compare the transparency of each sample, the associated physical variable is the average refractive index n_{avg}, being greater in the opaque one.
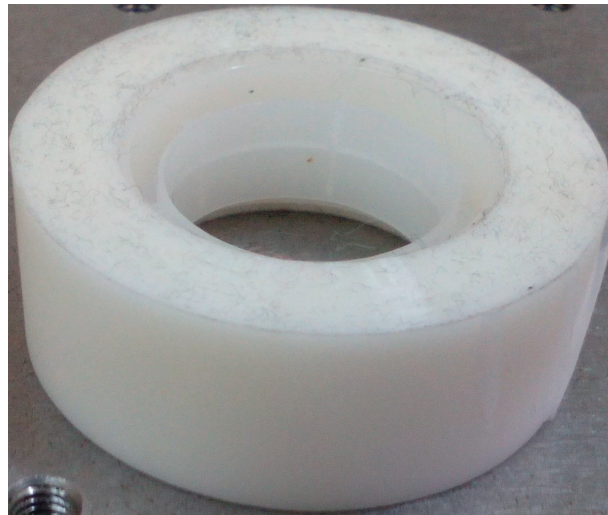
Figure 4.12: Opaque adhesive tape.

The projection image of the acquired volume using this sample represented in Figure 4.13. As in the previous one, no major irregularities are expected to be present in the sample and therefore its projection shows no particularly relevant information.
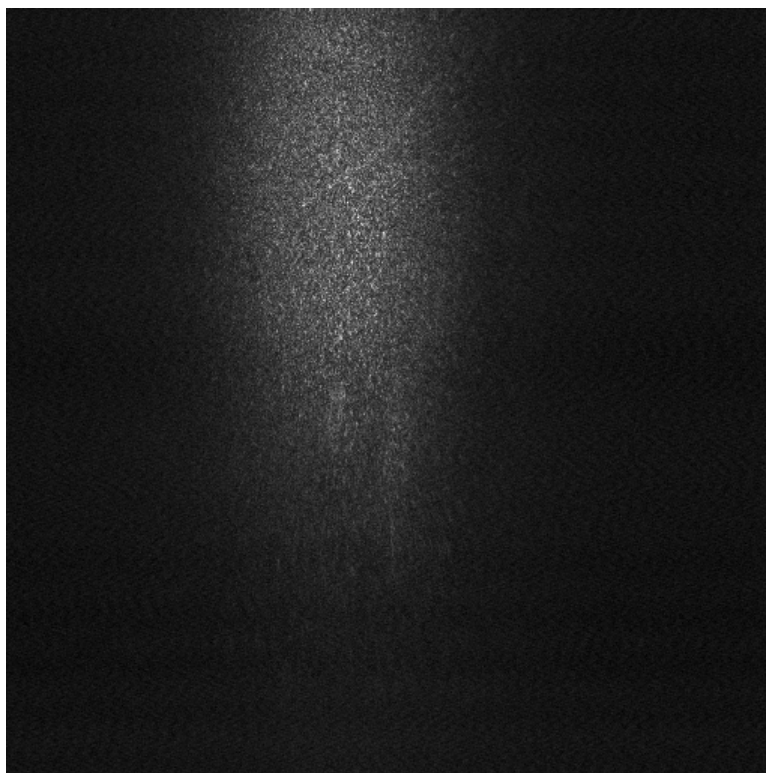
Figure 4.13: Projection image with a 512×512 resolution of the opaque adhesive tape.

Seeing that every B-Scan in the volume is very similar, a randomly chosen one is displayed in Figure 4.14. The clear benefits of using a logarithmic scale were already proven, so only the B-Scan rendered in this scale is displayed.
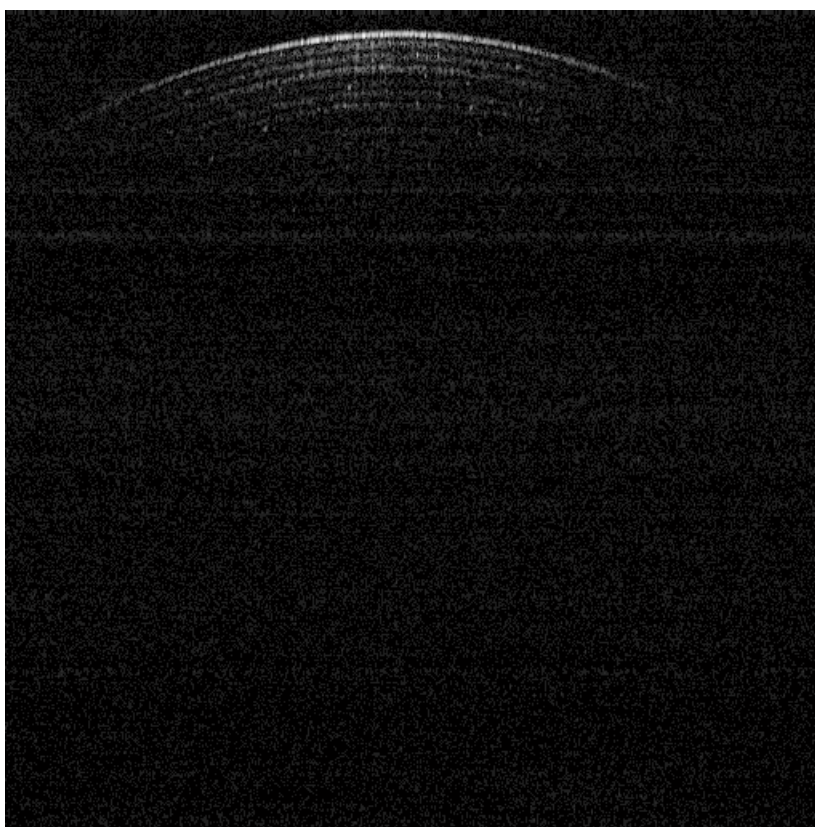
Figure 4.14: B-Scan with a 512×512 resolution of the opaque adhesive tape in logarithmic scale.

As expected, we verify that the imaged depth has significantly decreased for this adhesive tape, and consequently much less layers of tape are visible. This is due to the fact that the laser beam cannot penetrate as further in this case as it did in the last one, due to the mentioned different characteristics of the sample. Based on this considerations, we can assume an inverse proportionality between z_{max} and n_{avg}.

4.5   Rat

Finally, the OCT system was set to be used in an *in vivo* imaging exam, using a rat as sample. The rat was evidently anesthetized to ensure it remained as static as possible, and the corneas was kept hydrated and dilated using an opthalmologic hydration solution, for both the animal's comfort and the benefit of the imaging test.

This imaging exam proved to be more complicated than expected, not for any trouble with the acquisition system, but for the technical difficulty of aligning the laser beam with the rat's eye. To assist in this task, the animal stand that comes with the commercial Phoenix OCT system was used, and the angle of the incident beam was adjusted by a series of post holders, resulting in the setup shown in Figure 4.15.
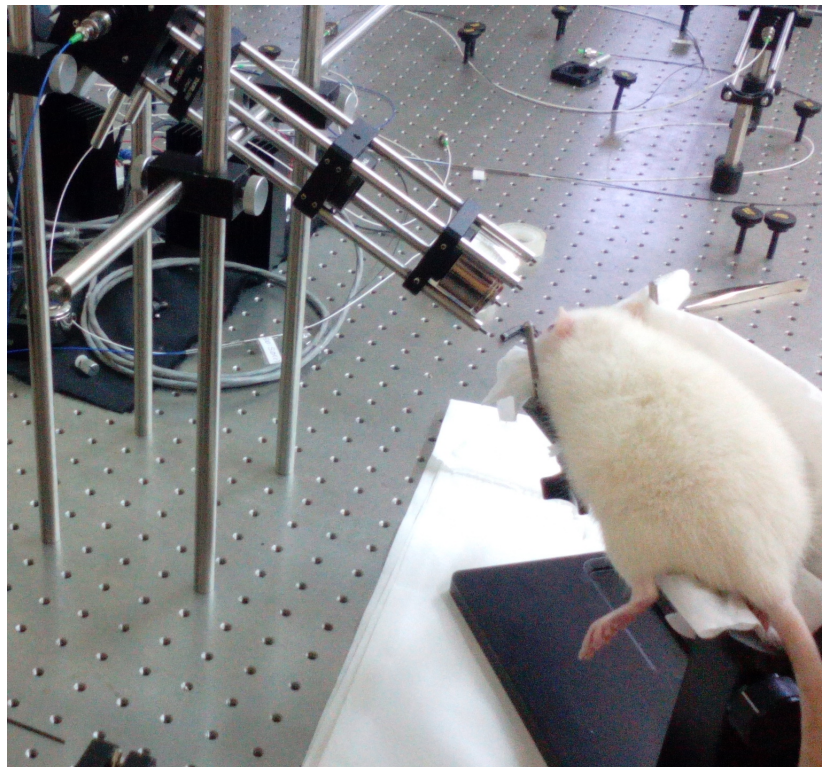
**Figure 4.15:** Apparatus used to properly position the rat to perform the OCT imaging test.

This animal stand allows adjusting the height and tilt of the rat, to properly focus the beam on its eye and make it enter perpendicularly. However, since the wavelengths swept by the laser are in the NIR region, the beam is invisible to the human eye. Therefore, ensuring that it was incident on the rat's eye was a complex

task. The only tool to assist in this, besides the B-Scan and projection image displayed in live mode, was a fluorescent target that responded to the absorption of the laser beam emitting a visible red light. By repetitively placing this target in front of the rat's snout and readjusting its position afterwards, we managed to focus the beam in the proper place. However, after aligning the beam with the eye, it was still necessary to position it in the specified working distance of the objective lens. The ideal way of doing this would be to move the sample arm of the OCT, bringing it closer or away from the rat's eye, without changing the angle of incidence while viewing the impact of this adjustment in the B-Scan in live mode. However, as shown in Figure 4.15, that was not an option because the sample arm is not movable in that way. Thus, there was no other way of doing this besides successively bringing the animal stand closer or further away and again readjusting the animal position so that its eye would be aligned with the beam. The mentioned difficulties caused this imaging test to last more than one hour before obtaining any acceptable results.

An acquired B-Scan is presented in Figure 4.16. For greater contrast it is displayed in logarithmic scale.
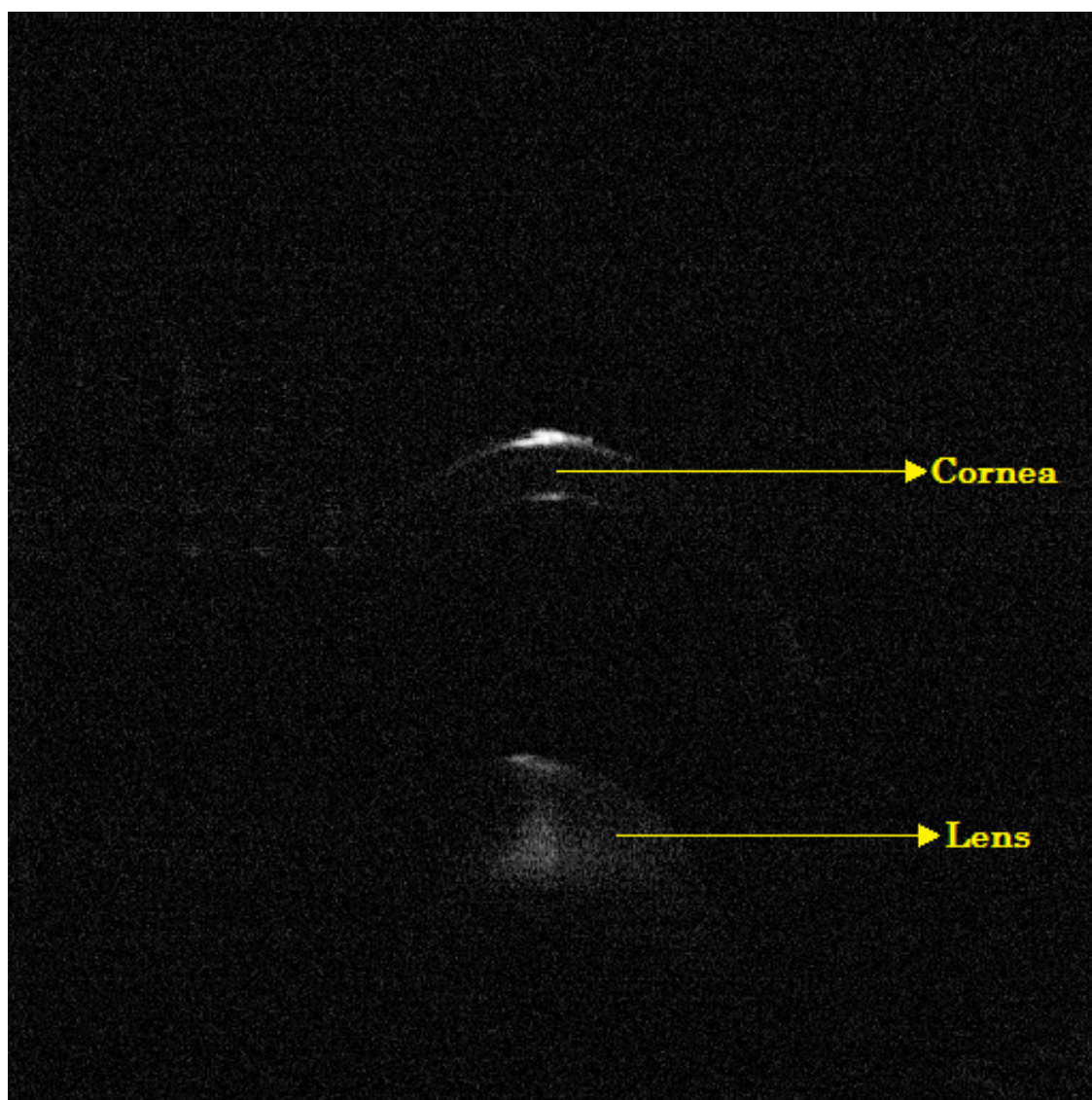
Figure 4.16: B-Scan with a 512×512 resolution of the rat's eye in logarithmic scale. The two visible structures are identified as the cornea and the lens.

Two structures are visible in this image. By knowing the structure of a rat's eye

(Figure 4.17), we can conclude that these are the cornea and a part of the lens.
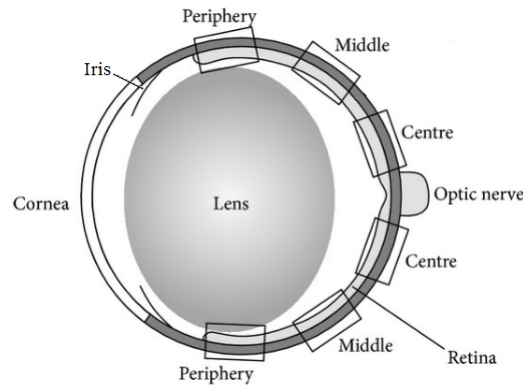
Figure 4.17: Scheme of the rat eye [45] (Adapted).

In Figure 4.16, the lens appears to be roughly at twice the expected distance from the inner layer of the cornea. Assuming this was not caused by any malformation or deficiency in the rat's eye, that indicates that the angle of incidence of the laser beam was far from being perpendicular as it should.

We can also conclude that the x-axis scanning covered a greater area than it should, since the visible layers of the eye only occupy about half of the B-Scan in this axis. Reducing the scanning angle would grant a greater resolution since more A-Scans would be acquired in the desired region.

This wide scanning angle also contributes to the exaggerated curvature of the visualized structures of the eye, which are already accentuated by nature when compared to the human eye.

Some suggestions on how to overcome the mentioned technical and mechanical difficulties will be presented in the next chapter.

5 | *Conclusions and Future Work*

To finish this work, and my specific contribution to the OCT project, it is pertinent to summarize the developed work and make some considerations that will come in handy for the next collaborators of this project.

To begin with, I believe it is fair to consider that the main goal of this work was reached. The OCT acquisition system, particularly its software, has proven to be fully working and capable of performing real time *in vivo* imaging. That alone is a great achievement from which several collaborators that worked on this project over the last 4 years deserve credit.

The modifications on the data acquisition system were many, with emphasis on the software upgrade. In fact, besides features such as background subtraction, logarithmic representation, live mode subsampling, the acquisition mode itself, among others, the whole logic acquisition principles were redefined, since it was the only way of being able to acquire, process and display data in the expected timing. Previous work suggested that the next step in the software development should be to integrate certain processing algorithms in a GPU (Graphics Processing Units) environment, with the aim of increasing the parallelism among processing tasks and therefore increase the performance of the system and reduce the processing and rendering times[26]. However, this work has proven that there was room for a lot of improvements and new implementations before even thinking about taking that step. In fact, acquisition times similar to the ones of commercial OCT systems were achieved without implementing any GPU processing algorithms.

Hopefully, this work will also allow a clearer interpretation of the OCT software principles and operation, which has so far been seen as a black box for those who were not directly involved with its development. Its documentation and description was susceptible to improvements in distinct ways, for instance by presenting the state diagram in Figure 3.1, which gives an immediate perception of the software tasks and working principles. It is my conviction that this work will allow for a next intervener in this development process to have an easier introduction to the software.

However, this declarations do not mean that no further work on the OCT acquisition system is required. On the contrary, as the system evolves, modifications or implementations of certain features that would benefit its performance become clearer. A review of some possible contributions to it will now be addressed. For the sake of clarity, they will be presented in distinct topics.

FFT

One mentioned reversal in this work was the fact that the FFT function that allows the visualization of the sample in time domain only accepts a power of 2 number of samples. Therefore we are faced with a dilemma: either use only 1024 of the 1376 possible samples per A-Scan and accept a decrease in the potential imaging depth, or zero pad the signal to get 2048 samples and accept the spectral leakage effect which blurs the depth profile of the sample. The software would benefit from an alternative way of performing the FFT, capable of providing similar computation times but without this sampling drawback, calculating the FFT of the exact 1376 samples.
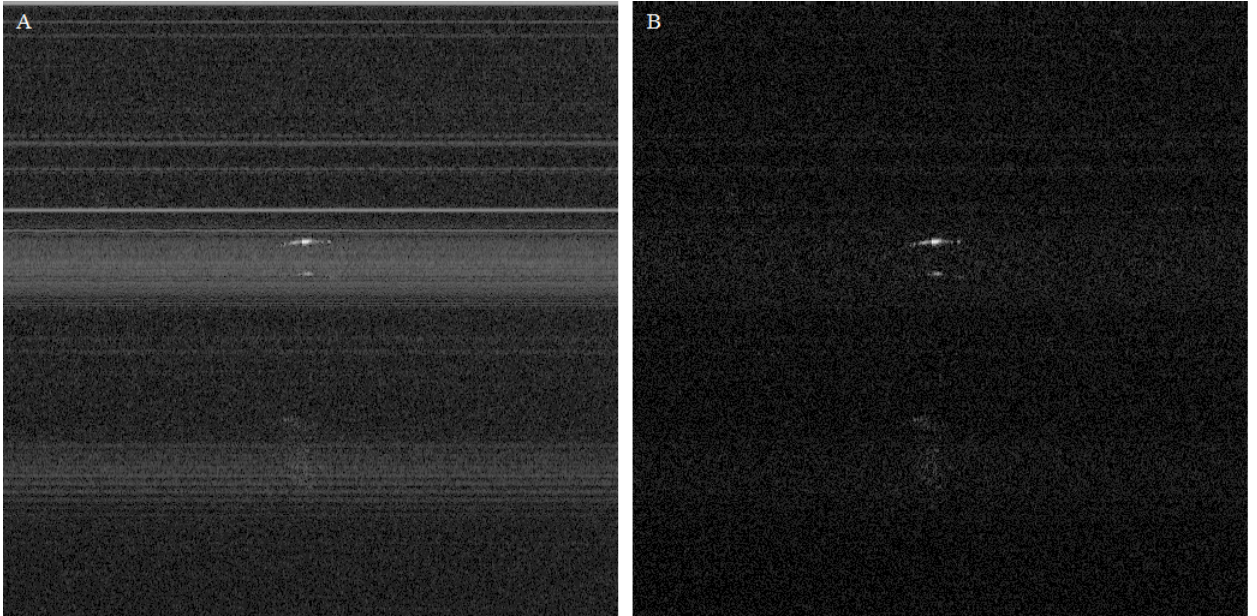
Background Subtraction

A new feature implemented was the ability of subtracting a previously acquired background signal to each incoming A-Scan, which proved to provide satisfying results. However, a distinct approach on this subtraction can be made. That is to make this subtraction using an A-Scan that contains no information on the sample (i.e. a Background A-Scan) selected among a B-Scan, instead of one acquired before the acquisition start.

This brings the advantage of accounting for certain noise sources that would otherwise be neglected, such as the different positions of the y-axis mirror which contribute differently to the component of the coherence noise not related with the sample. Also, since the background noise varies over time, we can generally assume that reducing the time span between its characterization and the A-Scans to which it is subtracted would provide a more accurate background profile.

On the other side, this alternative method can only be used in the case the horizontal scanned length is greater than the field of view of the lens or than the sample width, since otherwise all the acquired A-Scans would contain sample information and could not be used as background A-Scans.

Let us then analyze the practical results of this by considering Figure 5.1, which shows a B-Scan of the rat's eye (similar but distinct from the one previously presented in Figure 4.16) before any background subtraction and after it using the described method.

As we can see, this alternative background subtraction method also provides satisfactory results. All things considered, we cannot say that this method is better or worse than the one implemented in the OCT system, due to the mentioned limitations. All the more, these methods can complement each other, by saving an acquisition with background subtraction in the OCT system, and afterwards use signal a signal processing program to improve the noise removal according to the second method. In fact, that was the case in Figure 4.16, because a considerable noise component was still present in the image although the background subtraction was enabled. The reason for that was latter diagnosed as a loose connection in an optical fiber junction.

Figure 5.1: The same B-Scan image of the rat's eye before (A) and after (B) the background subtraction according to the described method.

Image Labeling

It would also be a relevant upgrade to make a correspondence between the sample number in each A-Scan to the correspondent relative distance. That would allow scaling the image to decipher the real distances between the visible layers of the sample. The best way of doing it would be to use a sample with a simple structure composed by two reflective layers at a known distance (e.g. a cover slip), determine the number of samples existing between the reflective layers (which would be the two maximums of the A-Scan FFT) and calculate the relation between these value and the distance of the corresponding layers in the sample in metric units. This relation would then give rise to the wished conversion factor. Note that when B-Scans are visualized with 512 or 1024 samples in the vertical axis this scaling factor is different, thus this procedure should be done for both cases.

The above mentioned procedure would allow labeling B-Scans in the y-axis which represents the depth of the sample. Labeling it in the x-axis is a more complex task, since it would depend on the angle swept determined by the function generator, which is not controlled by the software nor is it aware of its behavior.

X-axis Scanning Controlled by Software

Being able to control and adjust the x-axis scanning parameters by means of software instead of using an external unit would allow scaling the B-Scans and projection images in metric units in the horizontal direction, besides facilitating the user's interaction with the OCT system, which is currently controlled by both the software interface window and the function generator. This implantation in software would exclusively contribute as a more convenient and practical way of adjusting the x-axis scanning, since it already offers a perfectly stable, constant and overall reliable scanning, being hard to imagine how it could be improved in terms of performance. The mentioned integration in the software would also remove

the inconvenient of having to manually adjust the phase of the generated waveform every time the acquisition system is started, to make the first A-Scan coincide with the first column of the corresponding B-Scan.

This could be done by using a DAC that could be integrated in the software, capable of continuously generating the x-axis waveform signal after one single instruction that would pass the scanning parameters. This last characteristic is lacking in the NI PCI-6010 used to control the y-axis scanning. This DAC should also have a high frequency precision to grant a perfect synchronization between the scanning and the acquisition.

### Optical and Mechanical Apparatus

Notwithstanding the above considerations, it is evident that the main performance restrictions of the OCT are now related to the mechanical difficulties of properly positioning the animal used as sample and eventually the optical component of the system.

When imaging a static material sample a set of post holders allows to easily adjust the distance between the sample and the objective lens so that it is placed in the recommended working distance. However, this task is much more complex when using a living animal as sample since it naturally cannot be held by post holders. The used animal stand only allows adjusting the height and tilt of the animal, and not its distance to the objective lens. Doing so involves repetitively placing the animal stand closer or further away from the OCT sample arm which implies readjusting the height and tilt of the animal and verifying if the distance correction is sufficient or not, giving rise to an exhaustive iterative process. A way of improving this would be to attach the sample arm to a rail providing it with the mobility required to adjust the described distance. That would make the sample positioning process much simpler. Besides this distance adjustment, simply focusing and adjusting the scanning waveform of the laser beam in the eye proved to be a very difficult task since it is not visible to humans. That could be improved by using an objective lens with a smaller working distance as is the commercial Phoenix OCT, in which the rodent's cornea is completely covered with a coupling gel, and the objective lens couples with the eye as portrayed in Figure 5.2. A similar implementation in our OCT system would drastically reduce the mechanical difficulties of sample positioning.
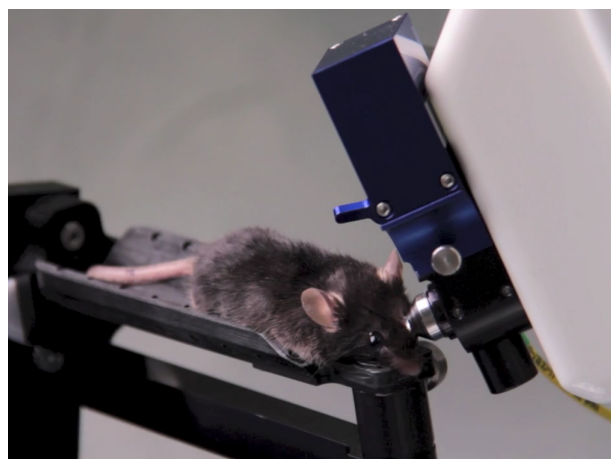
Figure 5.2: Sample positioning in the commercial Phoenix OCT system.

Another aspect that contributes to the difficulty in the sample positioning is the fact that the user can only rely on the B-Scan and projection image in live mode to get a sense of where the beam is focusing. Due to the computation effort needed to generate the projection image, it takes several seconds to completely refresh it, depending on the volume size (although it is progressively displayed line by line). Also, if the laser beam is not focused on the eye, it most likely will be focused on the animal's fur, which is very little reflective and therefore mostly noise will be displayed in the B-Scan and in the projection, which does not help defining what region is being visualized to make a proper correction of the animal's position and beam scanning. Certain commercial OCT's, such as the Phoenix OCT once more, are incorporated with a camera that shows to the user the region being scanned by the laser as represented in Figure 5.3.
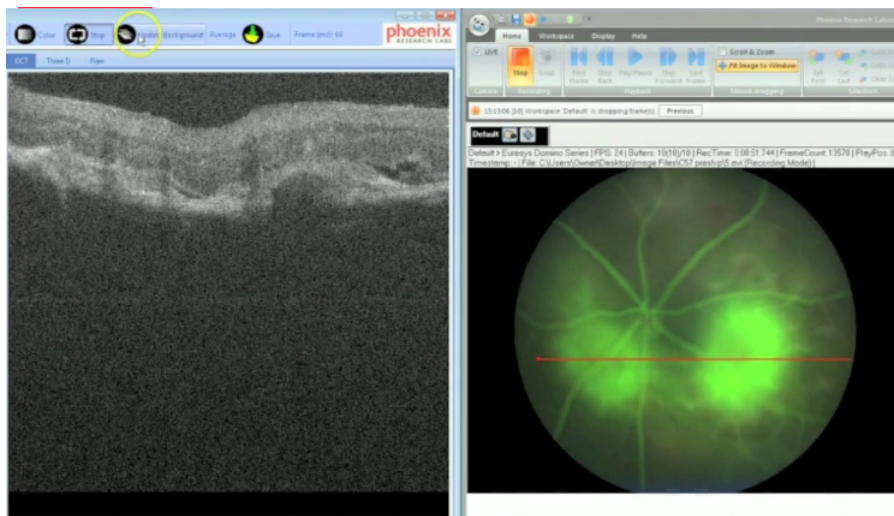
Figure 5.3: Software interface of the commercial Phoenix OCT system, providing a camera image on the right and a B-Scan on the left. The mouse used as sample has had an injection of fluorescein to enhance the blood vessels in the camera image. The red horizontal line indicates the region being scanned by the laser and displayed on the B-Scan.

This implementation in our OCT system would also be a significant contribution to overcome the exposed issue.

References

[1] Rushton, R. H. "The clinical measurement of the axial length of the living eye." Trans Ophthalmol Soc UK 58.1 (1938): 36-142.

[2] Franken, S. "Measuring the length of the eye with the help of ultrasonic echo." Ophthalmologica 143.2 (1962): 82-85.

[3] Duguay, M. A., and A. T. Mattick. "Ultrahigh speed photography of picosecond light pulses and echoes." Applied optics 10.9 (1971): 2162-2170.

[4] Fujimoto, James G., et al. "Femtosecond optical ranging in biological systems." Optics letters 11.3 (1986): 150-152.

[5] Fercher, A. F., K. Mengedoht, and W. Werner. "Eye-length measurement by interferometry with partially coherent light." Optics letters 13.3 (1988): 186-188.

[6] Clivaz, X., et al. "High-resolution reflectometry in biological tissues." Optics Letters 17.1 (1992): 4-6.

[7] Huang, David, et al.""Optical coherence tomography." Science 254.5035 (1991): 1178-1181.

[8] Pedrotti, Frank L., Leno S. Pedrotti, and Leno Matthew Pedrotti. "Introduction to optics". Vol. 2. Englewood Cliffs, NJ: Prentice-Hall, 1993.

[9] Tomlins, Peter H., and R. K. Wang. "Theory, developments and applications of optical coherence tomography." Journal of Physics D: Applied Physics 38.15 (2005): 2519.

[10] Hecht, Eugene. "Optics." 4th Edition, Addison Wesley Longman Inc, 1998.

[11] Brezinski, Mark E. "Optical coherence tomography: principles and applications". Academic press, 2006.

[12] Bashkatov, A. N., et al. "Optical properties of human skin, subcutaneous and mucous tissues in the wavelength range from 400 to 2000 nm." Journal of Physics D: Applied Physics 38.15 (2005): 2543.

[13] Jacques, Steven L. "Optical properties of biological tissues: a review." Physics in medicine and biology 58.11 (2013): R37.

[14] Weber, Marvin J. "Handbook of optical materials". CRC press, 2002.

[15] Wojtkowski, Maciej. "High-speed optical coherence tomography: basics and applications." Applied Optics 49.16 (2010): D30-D61.

[16] Massof, Robert W., and Fred W. Chang. "A revision of the rat schematic eye." Vision research 12.5 (1972): 793-796.

[17] Schmitt, J. M., A. Knüttel, and R. F. Bonner. "Measurement of optical properties of biological tissues by low-coherence reflectometry." Applied Optics 32.30 (1993): 6032-6042.

[18] Levitz, David, et al. "Determination of optical scattering properties of highly-scattering media in optical coherence tomography images." Optics express 12.2 (2004): 249-259.

[19] Knu, A., S. Bonev, and W. Knaak. "New method for evaluation of in vivo scattering and refractive index properties obtained with optical coherence tomography." Journal of biomedical optics 9.2 (2004): 265-273.

[20] Tuchin, Valerii Viktorovich. "Tissue optics: light scattering methods and instruments for medical diagnosis". 3 Edition, Bellingham: SPIE press, 2014.

[21] Dhalla, Al-Hafeez Zahir. "Development of Extended-Depth Swept Source Optical Coherence Tomography for Applications in Ophthalmic Imaging of the Anterior and Posterior Eye." (2012).

[22] Izatt, J. A., and M. A. Choma. "Theory of optical coherence tomography." Optical coherence tomography. Springer Berlin Heidelberg, 2008. 47-72.

[23] J. Cardoso. "Instrumentação e Sistemas de Aquisição de Dados - Interfaces e Sistemas de Aquisição de Dados". Department of Physics, University of Coimbra (2013)

[24] Bouma, Brett, ed. Handbook of optical coherence tomography. Informa Health Care, 2001.

[25] Yaqoob, Zahid, Jigang Wu, and Changhuei Yang. "Spectral domain optical coherence tomography: a better OCT imaging strategy." Biotechniques 39 (2005).

[26] Rodrigues, João. "Optical Coherence Tomography High Rate Acquisition Setup, Image Processing and Parallelism." University of Coimbra, IBILI, 2015).

[27] Agnelo, José. "Swept Source Optical Coherence Tomography for Small Animals: System Control and Data Acquisition." University of Coimbra, IBILI (2013).

[28] Podoleanu, A, Gh. "Optical coherence tomography." Journal of Microscopy (2012).

[29] Pedrosa, André. "Swept Source Optical Coherence Tomography for Small Animals - Performance Parameters and Optic Modelling ." University of Coimbra, IBILI (2015).

[30] Carvalho, Patrícia. "Optical Coherence Tomography Layout Simulation Using MATLAB®." University of Coimbra, IBILI (2016).

[31] Axsun Oct Swept Source Engine, "Operator Manual", no. 978. Massachussets, USA, 2010.

[32] Thorlabs Inc. Instrumentation, "PDB100 Series Balanced Amplified Photodetectors Operation Manual", Germany, Version 1.1 (2014).

[33] Innovative Integration, "X5-400M User's Manual", California, USA, Rev 1.01 (2011).

[34] Innovative Integration, "Data storage in memory". Available at: http://www.innovative-dsp.com/forum/viewtopic.php?f=43&t=13113&sid=83 dfb3f902481efb5a8881a95bd06f73/.

[35] Innovative Integration, "X5-400M FrameWork Logic User Guide", California, USA, Rev 2.1 (2009).

[36] Innovative Integration, "Malibu Library User's Manual", California, USA, Rev 1.4 (2013).

[37] Standford Research Systems, "Digital Delay / Pulse Generator DG535 Specifications".

[38] Thorlabs Inc. Instrumentation, "GVS001 and GVS002 Scanning Galvo Systems User Guide", Germany, Rev 19 (2015).

[39] Tektronix Inc., "AFG3000 Series Quick Start User Manual", Beaverton, Oregon, EUA.

[40] National Instruments Corporation, "NI 6010 Specifications", Redmond, USA (2005).

[41] National Instruments Corporation, "NI Dynamic Signal Acquisition", Redmond, USA (2010).

[42] Innovative Integration, "Data format on X3&X5 packet streaming boards". Available at: http://www.innovative-dsp.com/forum/viewtopic.php?f=18&t=411&hilit=data+format

[43] Malibu, "Samples Method", Redmond, USA (2010). Available at: http://www.innovative-dsp.com/support/onlinehelp/Malibu/!!OVERLOADED _Samples_Innovative_Fourier.html

[44] The MarcLab (University of Utah), "Mouse Schematic Eye". Available at: http://prometheus.med.utah.edu/ marclab/eyes.pdf

[45] Heiduschka, Peter, et al. "Lens injury has a protective effect on photoreceptors in the RCS rat." ISRN ophthalmology 2013 (2013).